Microstructural investigation of mixed rare earth iron boron processed via melt-spinning and high-pressure gas-atomization for isotropic bonded permanent magnets

by

Nicholas Lee Buelow

A thesis submitted to the graduate faculty

in partial fulfillment of the requirements for the degree of

MASTER OF SCIENCE

Major: Materials Science and Engineering

Program of Study Committee:
Iver Anderson, Major Professor
Matt Kramer
Frank Peters

Iowa State University

Ames, Iowa

2005

Graduate College
Iowa State University

This is to certify that the master's thesis of

Nicholas Lee Buelow

has met the thesis requirements of Iowa State University

Clive E. Anderson
Major Professor

Lawrence J. Genalo
For the Major Program

Dedicated to my family
and friends who encouraged
and believed in me every
step to the completion of
my degree

TABLE OF CONTENTS

IS-T2562

ABSTRACT

A solid solution of three rare earths (RE) in the $RE_2Fe_{14}B$ structure have been combined to create the novel mixed rare earth iron boron ($MRE_2Fe_{14}B$) alloy family. $MRE_2Fe_{14}B$ exhibits reduced temperature dependent magnetic properties; remanence and coercivity. The desired form of $MRE_2Fe_{14}B$ is a powder that can be blended with a polymer binder and compression or injection molded to form an isotropic polymer bonded permanent magnet (PBM). Commercially, $Nd_2Fe_{14}B$ is the alloy of choice for PBMs. Powders of $Nd_2Fe_{14}B$ are made via melt-spinning as can be $MRE_2Fe_{14}B$ which allows for direct comparisons. $MRE_2Fe_{14}B$ made using melt-spinning at high wheel speeds is overquenched and must be annealed to an optimal hard magnetic state. Due to the rare earth content in the $MRE_2Fe_{14}B$ powders, they must be protected from the environment in which they operate. This protection is accomplished by using a modified fluidized bed process to grow a protective fluoride coating nominally 15nm thick, to reduce air oxidation. $MRE_2Fe_{14}B$ has demonstrated reduced temperature dependent magnetic properties in ribbon and PBM form.

The real challenge has been modifying alloy designs that were successfully melt-spun to be compatible with high-pressure gas-atomization (HPGA). The cooling rates in HPGA are lower than melt-spinning, as the powders are quenched via convective cooling, compared to melt-spinning, which quenches initially by conductive cooling. Early alloy designs, in gas atomized and melt-spun form, did not have similar phase compositions or microstructures. Alloy additions, such as the addition of zirconium as a nucleation catalyst, were successful in creating similar phases and microstructures in the HPGA powders and melt-spun ribbon of the same $MRE_2Fe_{14}B$ composition.

CHAPTER 1: GENERAL INTRODUCTION

INTRODUCTION

Materials with permanent magnetic moments have been studied for years. One of the first materials to be classified as a permanent magnet was an iron bearing ore called lodestone [1]. As technology advanced, the iron bearing ores were refined to make steel, concentrating the amount of iron per unit volume, thereby increasing the magnetic properties. The properties of specific interest for this study are remanence and coercivity. Remanence and coercivity are defined as the internal field strength, after saturation, at zero applied field, and the reluctance of the internal magnetic moment to change direction in the presence of a reverse field, respectively [1]. Early experiments found that heat treated hardened steels had higher coercivity than mild steels of the same composition [1]. This observation created the distinction between hard magnets, high coercivity, and soft magnets, low coercivity. The results originated the terminology and the discovery that extrinsic effects (i.e. microstructure) will affect the magnetic properties. Figure 1 shows the difference in hystresis loops for hard and soft magnets and how the properties of remanence (M_r) and coercivity (H_{ci}) are measured from these loops.

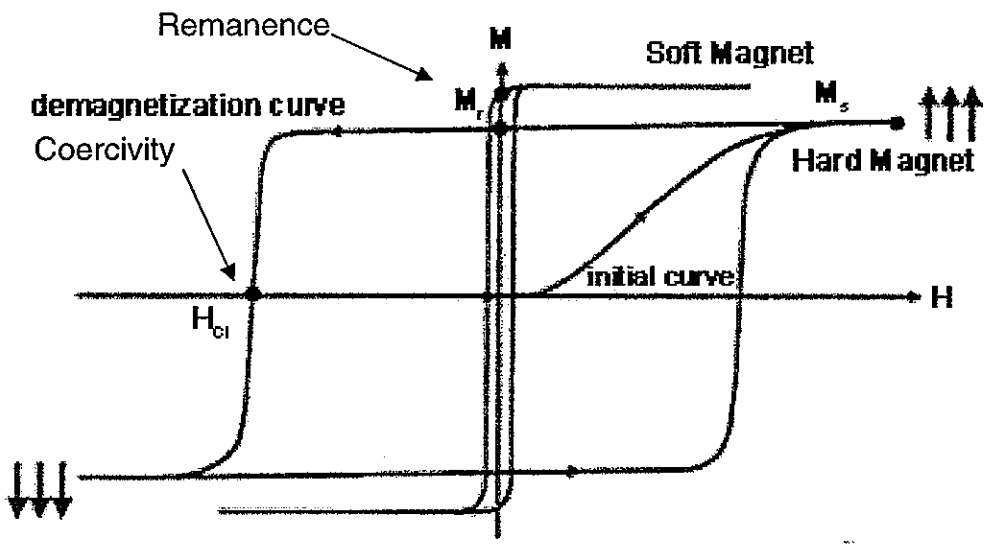

Figure 1: Hystresis loops showing difference between loops for hard and soft magnets and how remanence and coercivity are determined from the loop [2].

A product that resulted from the years of research on improvement of the intrinsic and extrinsic properties of magnetic materials is the high performance permanent magnet (PM). These PM alloys have high remanence and extremely high coercivity. Currently, neodymium iron boron ($Nd_2Fe_{14}B$) PMs are the best available [3] for high performance applications. The magnetic properties of $Nd_2Fe_{14}B$ arise from quantum interactions between the neodymium and iron and unit cell structure (intrinsic properties), and the microstructure (extrinsic properties) of the PM. The structure of the unit cell and microstructure are partially influenced by both alloy design and processing method. The combined usage of alloy design and process control has been used readily in the production of these technologically useful PM alloys.

The auto industry is pursuing PM technology for use in gas/electric hybrid automobiles. envisioning that traditional internal combustion engines will eventually be replaced by electric automobiles powered by fuel cells [4]. Commercial PMs have the magnetic strength to work in electric motor applications, but have an intrinsic limitation that affects their magnetic properties. The problem is related to a tendency for the maximum energy product (BH_{max}) to be inversely proportional to temperature, Figure 2. BH_{max} is the amount of energy stored per unit volume of PM [1]. This value affects the amount of work that the magnetic field is able to do outside the volume of the PM [1] and is measured by fitting the largest rectangular area that is possible in the second quadrant of the hystresis loop. BH_{max} is the combined effect of remanence and coercivity (see Figure 3).

To alleviate the temperature dependence of $Nd_2Fe_{14}B$, a new PM alloy is being developed to address this issue, along with some other important manufacturing issues. The alloy design theory behind $RE_2Fe_{14}B$ PM systems was adapted for use in the development of novel mixed rare earth iron boron ($MRE_2Fe_{14}B$) alloy family. Two versions of this new PM alloy family combine neodymium, yttrium, and dysprosium with iron, cobalt, and boron to reduce the loss of BH_{max} as temperature increases [5] (see Figure 2).

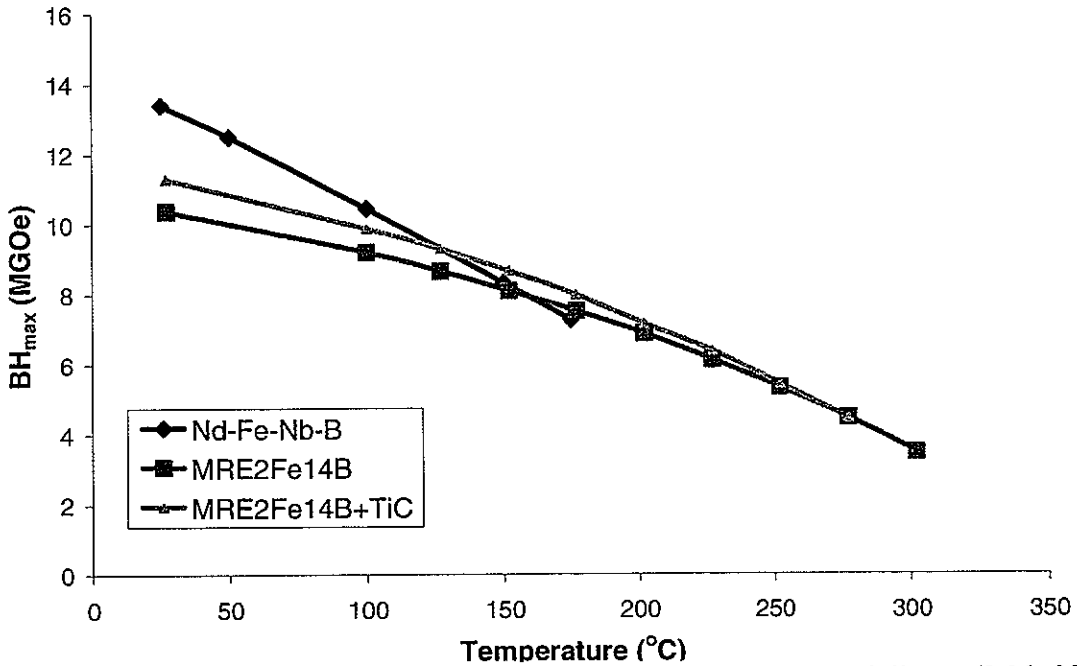

Figure 2: Temperature stability of BH_{max} of $MRE_2Fe_{14}B$ vs. a commercially available Nd-Fe-Nb-B. $MRE_2Fe_{14}B$ is shown with and without a TiC addition.

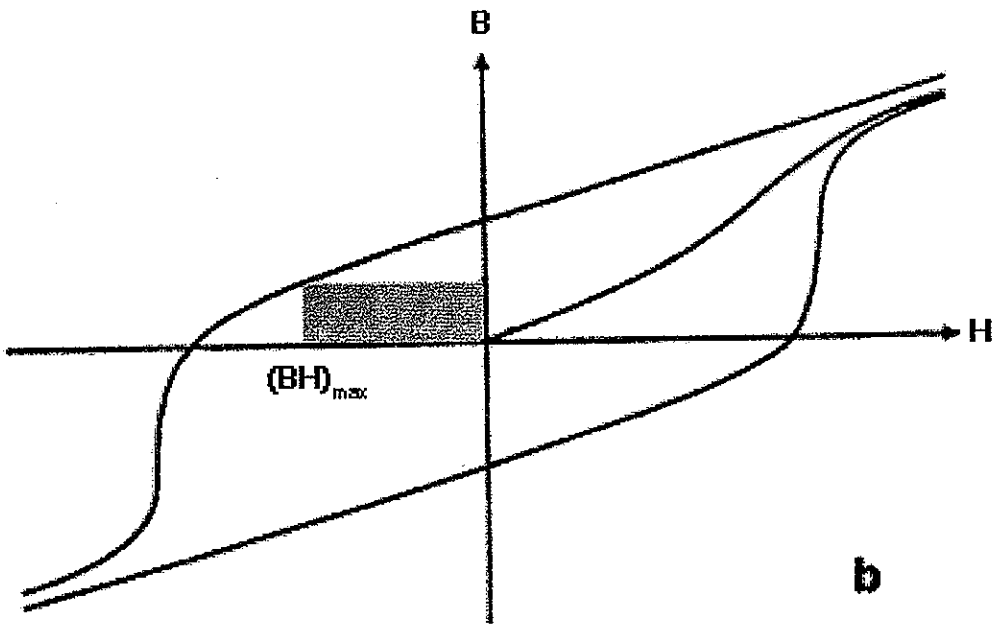

Figure 3: Measuring BH_{max} from a hysteresis loop [2].

$MRE_2Fe_{14}B$ magnet alloys have reduced temperature dependent magnetic properties beyond 200°C. The magnetic properties of $Nd_2Fe_{14}B$ based PMs deteriorate rapidly due to an increase in temperature [5], as shown in Figure 2. Over the temperature range of 25°C to 200°C commercial Nb-modified $Nd_2Fe_{14}B$ experienced a ~50% loss in BH_{max}, whereas, $MRE_2Fe_{14}B$ experienced a ~27% loss of BH_{max}. $MRE_2Fe_{14}B$ has a smaller (reduced) temperature dependent remanence ($\Delta M_r/\Delta T$) and coercivity ($\Delta H_{C_i}/\Delta T$) parameter compared to $Nd_2Fe_{14}B$. To maximize the magnetic output of the alloy design a method of synthesizing an optimum fine uniform microstructure for the $MRE_2Fe_{14}B$ alloys is being attempted through the use of melt-spinning and high-pressure gas-atomization (HPGA). Both rapid solidification processes can reach cooling rates of 10^6K/s (only in the finest particles for gas atomization) [6]. Depending on the alloy, both processing methods can form amorphous and nanoscaled structures with differences found in the nucleated phases and growth orientations. The challenge has been to adjust alloy designs and annealing treatments to convert the alloy design developments made with melt-spun ribbons into HPGA powders with fine spherical particulate form, preferred for polymer bonding.

THESIS ORGANIZATION

This thesis represents work related to the development of $MRE_2Fe_{14}B$ by melt-spinning for commercial testing and powder production by HPGA. The constituent papers in Chapters 2, 3, and 4 were written as a requirement of presentation at technical conferences which published the papers in the associated conference proceedings. The final paper chapter 5 was written for submission to *Materials Science and Engineering A*. Chapter 1 is a general presentation to introduce the subject matter that will be covered in later chapters. The first paper, Chapter 2, is the first attempt at using metallographic and magnetic investigation to understand the differences and similarities between HPGA powder and melt-spun ribbon of the same composition. In Chapter 3 the focus is on the use of a nucleation catalyst to influence the microstructure and magnetic properties of HPGA powder. Results concentrate on the commercial testing of $MRE_2Fe_{14}B$ in polymer bonded magnet form. Results presented in Chapter 4 concentrate on the use of a modified fluidized bed process to grow a protective fluoride layer around the particles. Effects of the fluoride coating on the

reduced loss of magnetic properties in a polymer bonded magnet are discussed. The final paper (presented in Chapter 5) is a combination of Chapter 2-4 with discussion on the use of cooling rate models to predict what particle size and wheel speed (which controls the ribbon thickness) will have on similar average cooling rates. General conclusions that can be drawn from this work are presented in Chapter 6, along with recommendation for future work. Following that is the acknowledgments of the people who help in the data collection for this document.

LITERATURE REVIEW

Previous Research and Motivation

Permanent magnet (PM) technology has been continually evolving for the past 20 years, since the discovery of rare earth transition metal (RE-TM) PMs, especially $RE_2Fe_{14}B$ alloys that possess improved magnetic strength at relatively low cost [7]. In the automotive industry, the gas/electric hybrid automobiles are making use of PMs in electric drive motors. These automobiles require magnets that have a large BH_{max} for performance that is comparable to the traditional internal combustion engine [4]. Performance levels must also be maintained over a wide range of operating temperatures, especially at high temperatures, a current weakness of PM electric motors. Applications in the fields of medicine and computer technology are also finding uses for $RE_2Fe_{14}B$ PMs [2].

Traditional $RE_2Fe_{14}B$ alloys are a staple in PM technology and therefore have been the subject of much research. The majority of work on the $RE_2Fe_{14}B$ magnet alloy system has been dedicated to the reduction of α-Fe formation, increasing BH_{max}, and increasing the Curie temperature [8]. The outcome of the research showed that a variety of alloying and processing modifications were able to reduce α-Fe formation and increase BH_{max}. Increasing the Curie temperature of $RE_2Fe_{14}B$ magnet alloys was accomplished typically by the substitution of cobalt for part of the iron content [3]. This substitution has helped the high temperature performance of $RE_2Fe_{14}B$; however, this was at a cost to the coercivity because cobalt's magnetocrystalline anisotropy is not as high as iron's [2]. Striking a balance between the relevant magnetic properties allowed this type of PM to be tailored to many different applications.

Mixed Rare Earth Iron Boron

The driving force behind the on-going development of $MRE_2Fe_{14}B$ magnet alloys has been retention of magnetic properties at significantly increased operating temperature [5]. This is being accomplished by combining three REs in a solid solution based on the $RE_2Fe_{14}B$ unit cell in what is assumed to be an "ideal" alloying behavior. $MRE_2Fe_{14}B$ alloys are intended to exhibit beneficial magnetic properties that correspond to the "symbiosis" of the three REs present in the unit cell, e.g. improvement in thermal stability of magnetocrystalline anisotropy (influencing coercivity) of $MRE_2Fe_{14}B$ by the incorporation of $Y_2Fe_{14}B$, as seen in Figure 4b. Increased thermal stability of the magnetic moment (influencing remanence), found in $Dy_2Fe_{14}B$, and has also been coupled into the $MRE_2Fe_{14}B$ formulation. Finally, the increased saturation from $Nd_2Fe_{14}B$, as indicated in Figure 4a, was added as well [9]. Another boost to the $MRE_2Fe_{14}B$ alloys is accomplished by the addition of cobalt, which is well known to increase the Curie temperature of $RE_2Fe_{14}B$ magnets [10]. This increase in Curie temperature should also extend the range of stable operating temperatures for $MRE_2Fe_{14}B$.

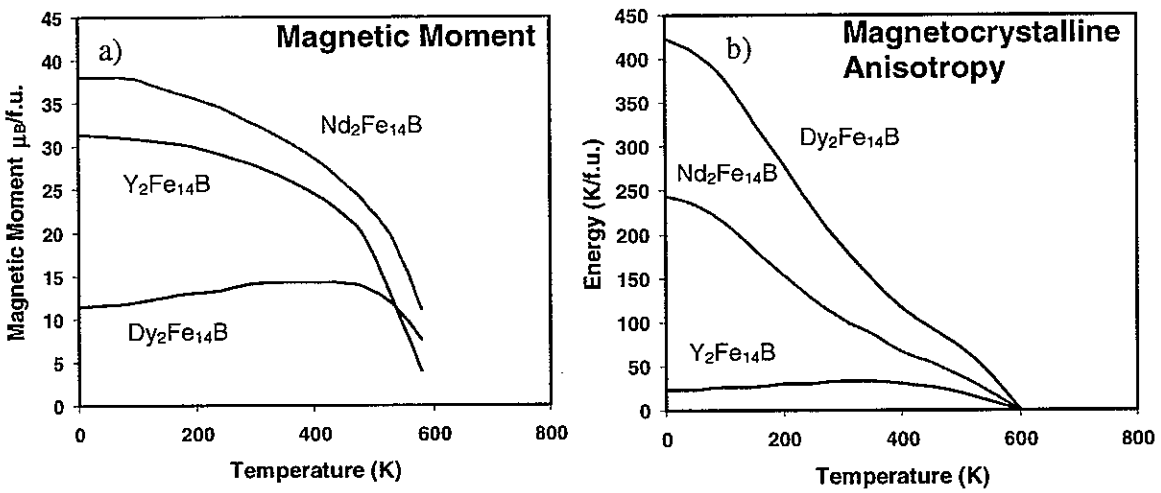

Figure 4: Comparison of magnetic properties of $Nd_2Fe_{14}B$ to two other 2-14-1 phases. a) Temperature dependence of the magnetic moment (remanence) and b) temperature dependence of the magnetocrystalline anisotropy (coercivity).

Enhancing the intrinsic magnetic capabilities of $MRE_2Fe_{14}B$ was accomplished (as described above) though selective addition of elements known to enhance magnetic

properties, namely, remanence and Curie temperature. However, attention must be paid to extrinsic effects that affect the magnetic properties. Microstructure is dictated by processing, mostly, but can be influenced by alloy design, as well. The use of zirconium is known to increase the number of nucleation sites in PM alloys as a nucleation catalyst, effectively refining the microstructure and increasing the coercivity [11]. Coercivity is very dependent on the size of the features in the microstructure that will affect the formation of domain walls. Any element that will refine the microstructure has the possibility to enhance coercivity, using the correct processing techniques. Another option is the use of a compound that will pin the grain boundaries, restricting growth of the microstructure. An example of a compound that will accomplish this is titanium carbide [12].

The solidification path for $MRE_2Fe_{14}B$ is expected to closely resemble the path shown as a dashed line in Figure 5a, on this vertical section of the Dy-Fe-B ternary phase diagram. This assumption is based on examination of the possible phase diagrams and alloy design considerations. The Y-Fe-B and Dy-Fe-B systems are the two highest melting systems, 1300°C and 1280°C respectively, for the $RE_2Fe_{14}B$ compound [13]. The Dy-Fe-B phase diagram is preferred for analysis of the solidification path because more is known about Dy-Fe-B system, compared to the Y-Fe-B system. Yttrium and dysprosium also have ionic radii that are within 0.2% of each other, 1.773Å and 1.775Å respectively [14]. Neodymium is about 2.7% larger than dysprosium and yttrium with an atomic radius of 1.822Å [14]. The similarity of the yttrium and dysprosium atomic radii means there is a good possibility that the two elements are soluble in the each other's $RE_2Fe_{14}B$ lattice, without causing excessive internal stress due to a difference in atomic radii [15]. Also, there is some probability that neodymium will be at least partially (>5at%) soluble in the dysprosium's or yttrium's $RE_2Fe_{14}B$ lattice due to its 2.7% size mismatch. The 2.7% size difference is less than the size difference suggested by Hume-Rothery of 13-14%. Above 13-14% size mismatch there is not predicted to be extensive solid solubility [15].

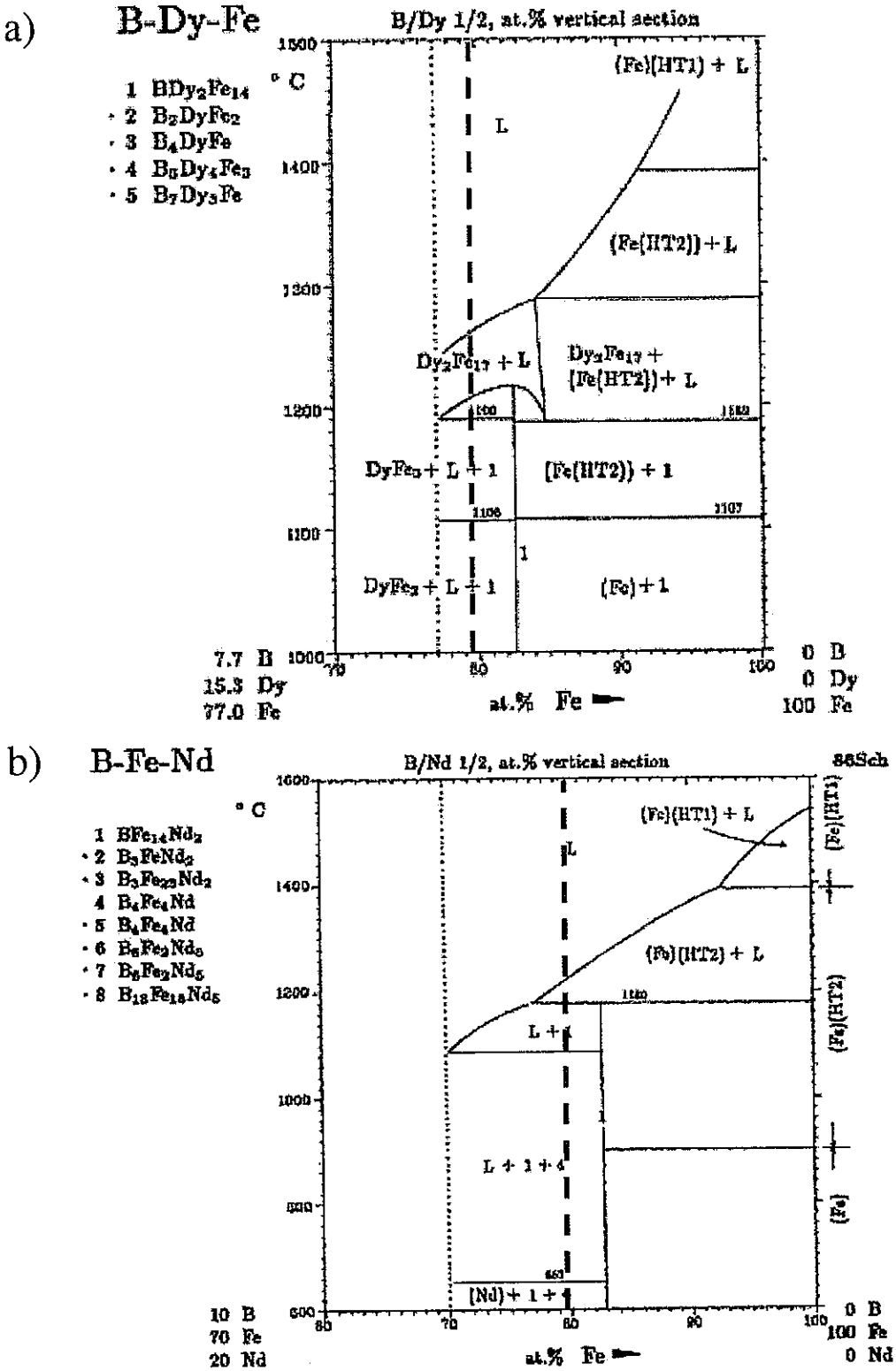

Figure 5: a) Dy-Fe-B vertical section b) Nd-Fe-B vertical section. Red lines indication composition on both diagrams [13].

Understanding what phases are forming and where they are forming is critical to the on-going development of $MRE_2Fe_{14}B$. Examination of the phase diagram points to boron as the deciding factor in how $MRE_2Fe_{14}B$ solidifies. In other words, the only phase in the Dy-Fe-B phase diagram that would consume boron from the melt is $MRE_2Fe_{14}B$. The boron could be consumed in that phase or possibly in the $MRE_1Fe_4B_4$ phase, as predicted on the Nd-Fe-B phase diagram. Figure 6 demonstrates how $MRE_2Fe_{14}B$ might solidify, if cooling rates are not sufficient to form an amorphous microstructure.

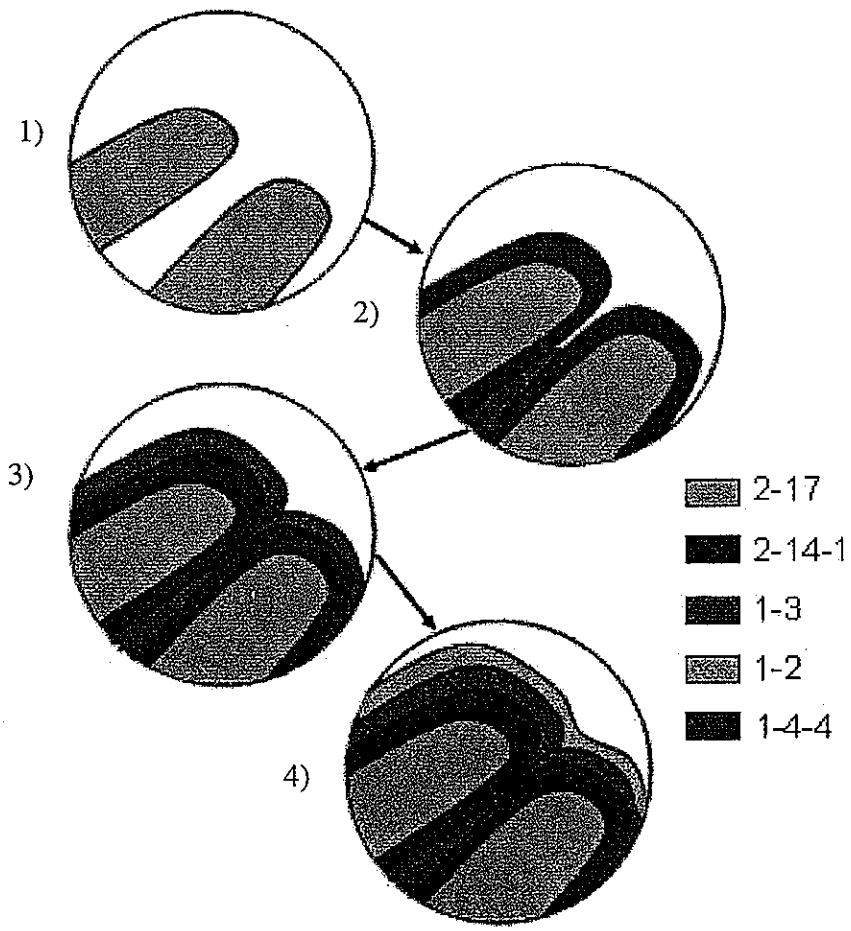

Figure 6: Schematic of possible solidification pattern seen in $MRE_2Fe_{14}B$ for atomized powders.

Since the MRE_2Fe_{17} phase field covers the peritectic $MRE_2Fe_{14}B$ line compound, MRE_2Fe_{17} will be the primary solidification product for $MRE_2Fe_{14}B$ in the as-solidified state, without high undercooling. The next phase to nucleate will be the $MRE_2Fe_{14}B$ phase and

will likely form a layer around the MRE_2Fe_{17} primary phase. Due to possible boron enrichment in the intercellular or interdendritic region, it is likely that $MRE_2Fe_{14}B$ jumps to the behavior of the Nd-Fe-B phase diagram and creates the $MRE_1Fe_4B_4$ phase. As the material continues to cool, the formation of other phases is possible (e.g. MRE_1Fe_3 and MRE_1Fe_2), as dictated by the phase diagram, creating a layered morphology.

Influence of Microstructure on Magnetic Properties

The formation of α-Fe causes difficulty in the processing of $Nd_2Fe_{14}B$, because a two-phase field that prefers α-Fe as the primary solidification product covers the peritectic $Nd_2Fe_{14}B$ line compound. The $Nd_2Fe_{14}B$ system also has a low melting eutectic reaction that is a concern for near-stoichiometric nanocrystalline $RE_2Fe_{14}B$ magnetic materials generated by rapid solidification processing. To lessen the temperature range where α-Fe is the preferred solidification product, the nominal composition of the magnet alloy can be made rare earth-rich, effectively decreasing the amount of undercooling needed to bypass the formation of α-iron. However, lowering the iron content moves the composition of the magnet alloy further away from the peritectic $Nd_2Fe_{14}B$ line compound (see Figure 5b).

Besides the composition and temperature limitations of the phase diagram there are many properties that make $Nd_2Fe_{14}B$ desirable as a hard magnetic material. $Nd_2Fe_{14}B$ is known for its consistently large BH_{max} values, ~50MGOe [16]. The BH_{max} value for this magnet is still lower than the intrinsic capability of the material due (~60MGOe) presumably to microstructure effects [2, 7]. The relationship of microstructure to coercivity is partially explained by Brown's paradox. Brown's paradox explains how the coercive field, $\mu_0 H_c(T)$, of a real microstructure is much less than the theoretically predicted coercive field [17]. BH_{max} is partially determined by the coercivity of a PM, therefore maximizing coercivity is necessary to maximize BH_{max}.

$$\mu_0 H_C(T) = \alpha_{ex}\alpha_K \mu_0 H_N^{\min}(T) - N_{eff} J_S(T) \qquad (1)$$

Equation 1 relates the coercivity attainable to the type of microstructure present in the material and is known as Brown's expression. The permeability of free space is represented by μ_o and coercivity as a function of temperature is $H_c(T)$. The parameter α_K takes in to account that the surface of the grain is nonideal. The α_{ex} describes the reduction of the coercive field caused by the exchange coupling of the grains. Also N_{eff} is the effective demagnetization factor that accounts for local demagnetization fields in the grain structure and J_s is the spontaneous polarization of the magnetic moments as a function of temperature. All of these values are microstructural parameters related to the microstructure of real magnets. The H_N^{min} (T) term denotes the minimum of the angular dependence of the ideal nucleation field [17].

When comparing the microstructure of nanocrystalline stoichiometric $Nd_2Fe_{14}B$ with melt-spun $MRE_2Fe_{14}B$, the microstructure of $MRE_2Fe_{14}B$ can be a close match. When looking at the TEM images in Figure 7, it hints that $MRE_2Fe_{14}B$ must also be a stoichiometric PM alloy, as the other image shows the microstructure of a stoichiometric PM [3]. Stoichiometric nanocrystalline PM alloys are known for being exchange coupled. Greater exchange interaction between neighboring grains will decrease the coercivity, and increase remanence. The opposite is also true for less exchange coupling [18].

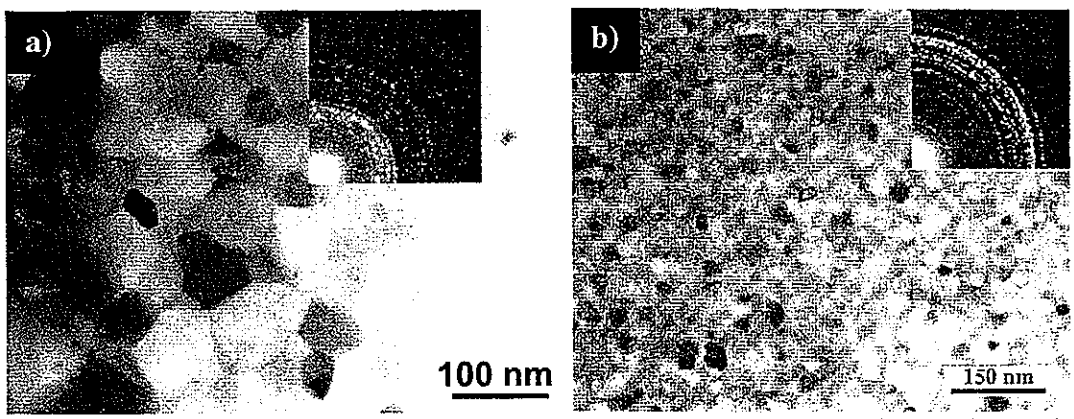

Figure 7: a) TEM image of melt-spun $MRE_2Fe_{14}B$ b) TEM image of stoichiometric $Nd_2Fe_{14}B$ [3].

The best PM alloy designs will always be limited by the microstructure of the material. Microstructure has a direct effect on the magnetic properties through the linkage of

solidification processing and annealing treatments [4]. Rapid solidification techniques have the ability to promote as-solidified formation of the desired phases with the highly refined microstructures needed for optimal isotropic magnetic properties. This has been proven in the production of other $RE_2Fe_{14}B$ magnet alloys of the nanostructured type [3]

Powder Production

There are many methods to make PM powders. Some involve several steps to achieve a quality PM powder; other techniques can produce the powder directly. Traditional chill casting techniques can be employed for the production of $RE_2Fe_{14}B$ powders though the use of a hydrogen-decomposition-desorption-recombination (HDDR) process. In HDDR processing thin, ~10mm, ingot is cast and then homogenized at high temperature (~1000°C) for a long time (~20hrs) in a flowing argon atmosphere [19]. Due to slower solidification rates, the magnetic phases in the thin casting will segregate. The thin casting will see slightly elevated solidification rates, as compared to normal castings, due to the reduced distance the heat has to travel to get to the chill [20]. There is a possibility that $RE_2Fe_{14}B$ will nucleate near the chill. The homogenization process causes preferred growth of the $RE_2Fe_{14}B$ phase. The material is then heated at ~800°C in a flowing atmosphere of hydrogen to weaken the material for the milling process. High energy mechanical milling and jet milling is used to obtain a final mean (HDDR) powder size of ~3μm [21].

To reduce or eliminate the homogenization step used for cast ingots of $RE_2Fe_{14}B$, a method called strip casting can be employed. Strip casting involves quenching the molten PM material on a rotating copper wheel. Wheel speeds are usually low at 1m/s [22] to 10m/s [21], depending on the desired solidification rate. Instead of a casting 10mm thick, strip casting produces a ribbon strip, 250μm to 350μm thick. This reduction in thickness reduces the distance the heat has to travel though the material to the chill increasing the solidification rate and reducing phase segregation. This structure allows the strips to go right to HDDR and milling, skipping the homogenization step [21]. Both of the afore mentioned methods use master alloys that are rare earth rich to decrease the temperature range when α-Fe is the preferred solidification product [19, 22], increasing the probability of getting $RE_2Fe_{14}B$ in the as-quenched state

Thin cake and strip casting accompanied by the HDDR process can make fine powders using off-stoichiometry master alloys. These processes are labor intensive. Rapid solidification is the preferred technique for production of nanocrystalline PM powders, as the number of steps needed to get to the final powder form is reduced. The extreme solidification rates available in these techniques form microstructures optimal for hard magnetic properties and can be produced on stoichiometry. The formation of the structures and phase selection during rapid solidification is kinetically controlled. At the melting temperature the free energy of the solid and liquid phases are equal and therefore, the energy barrier to nucleation, ΔG^*, is infinite and solidification at T_m is not possible [23]. As the temperature, of the system drops below T_m the barrier, ΔG^*, is inversely proportional to $(T_m - T)^2$ [23]. The barrier to nucleation is still large even when T is less than T_m, meaning that the melt can be taken below T_m and still be a liquid for a certain amount of time. This is called undercooling, where the amount of undercooling dictates the phases present and the velocity of the solidification front dictates the microstructure. During rapid solidification a relatively slow solidification front will result in a dendritic structure. As the front velocity is increased, a cellular structure is created. Velocities beyond that can result in solute trapping and a resulting nanocrystalline structure or, perhaps, an amorphous structure. An amorphous structure is accomplished when the liquid is transformed to solid so quickly the atoms get locked in a "solid liquid" state before they can move to a crystal orientation

Free-jet chill-block melt spinning and high-pressure gas-atomization (HPGA) are being investigated as possible rapid solidification processing routes for production of $MRE_2Fe_{14}B$ powder. Both techniques have the ability to solidify the melt at a rate sufficient to create amorphous and/or nanocrystalline structures [23]. Both structures are desirable for development of optimal isotropic PM powders. The creation of a fully amorphous structure in the as-spun/atomized state allows for excellent control over the microstructure during the annealing process, crystallizing the $MRE_2Fe_{14}B$ phase from the amorphous solidification product at a specified temperature. The grain size is then controlled by duration of exposure to the specified annealing temperature. The most desirable as-spun/atomized microstructure would be nanocrystalline. With the proper size and shape of the crystals, an optimized hard magnetic state can be produced without the need for further heat treatment, reducing cost. If

either the amorphous or nanocrystalline microstructure forms, a second phase that limits the growth of the nanocrystalline structures may be desirable. Large grains present after annealing are detrimental to the magnetic state, due to enhanced nucleation of reverse domains. Reverse domains in large grains will neutralize the overall magnetic moment of the grain.

The melt-spinning technique gives direct control over the melt homogeneity, solidification rate and undercooling, and, therefore, microstructure, based on wheel speed and melt superheat [24]. Melt-spinning solidifies the melt through direct contact with a rotating water cooled copper wheel. The thermal conductivity of copper is responsible for pulling the heat out of the melt, i.e., conduction heat transfer. Therefore, the material closest to the wheel surface will see the highest quench rate. At reduced wheel speed, the ribbon can depart from contact with the wheel before complete solidification and must finish solidification and cooling by convection to the stagnant chamber atmosphere. The faster the wheel is moving, the thinner the resulting ribbon will be, increasing the quench rate throughout the thickness of the ribbon [25].

Undercooling in melt-spinning is seen when the liquid is cooled below its melting point and maintained as a liquid on the surface of the wheel for some distance before nucleation occurs, Figure 8b [26]. Nucleation of the solid phase will occur on the wheel surface, downstream of the puddle, and proceeds as a gradient moving up through the ribbon from the wheel surface to the free surface. The further away from the melt jet puddle, the more solidified the ribbon has become. The ribbon produced can be crushed, in an inert atmosphere, into a relatively fine powder, depending on the degree of as-spun crystallinity, with minimal loss of magnetic properties.

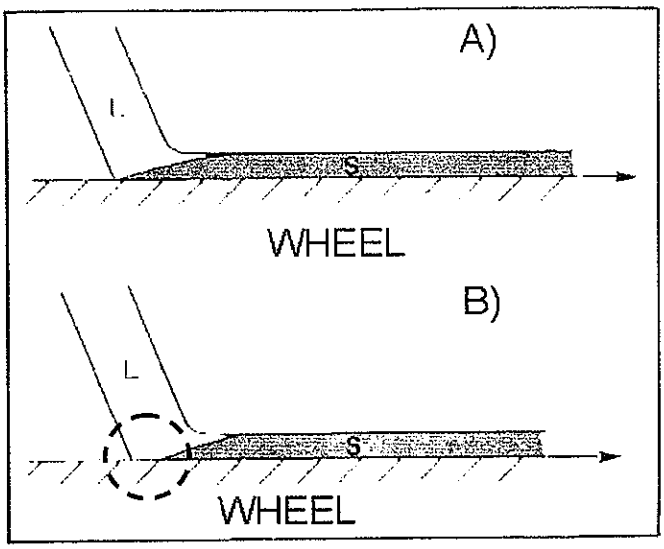

Figure 8: Representation of idealized solid/liquid interface if nucleation occurs near the wheel surface. a) Nucleation occurs near liquidus temperature b) Large undercooling is experienced before nucleation, liquid is present for a distance on the surface of the wheel before solidification [26].

HPGA can directly create spherical powders with a very fine particle size from the $MRE_2Fe_{14}B$ alloy. Particle size is dependent, for example, on the atomizing gas. Using helium as the atomizing gas creates more fine particles (dia. <10μm) per batch, as compared to argon. Higher velocities are attainable for helium as compared to argon allowing for more break-up of the melt because helium is a lighter gas with a reduced viscosity [27]. For $MRE_2Fe_{14}B$, helium atomization gas is used to create high yields of particles that are >20μm. The >20μm particles are where the greatest undercooling is expected to be achieved for $MRE_2Fe_{14}B$. This is because the catalysts for nucleation, known as motes, are more dispersed in the smaller particles. The dispersion of the motes leads to increased undercooling and is known as the mote isolation effect [27]. Figure 9 illustrates how breaking up the melt into smaller and smaller droplets disperses the motes, creating many droplets with no motes that can reach higher undercoolings [28]. The mote isolation effect can allow particles finer than about 10μm diameter to experience completely adiabatic solidification at high undercoolings [29].

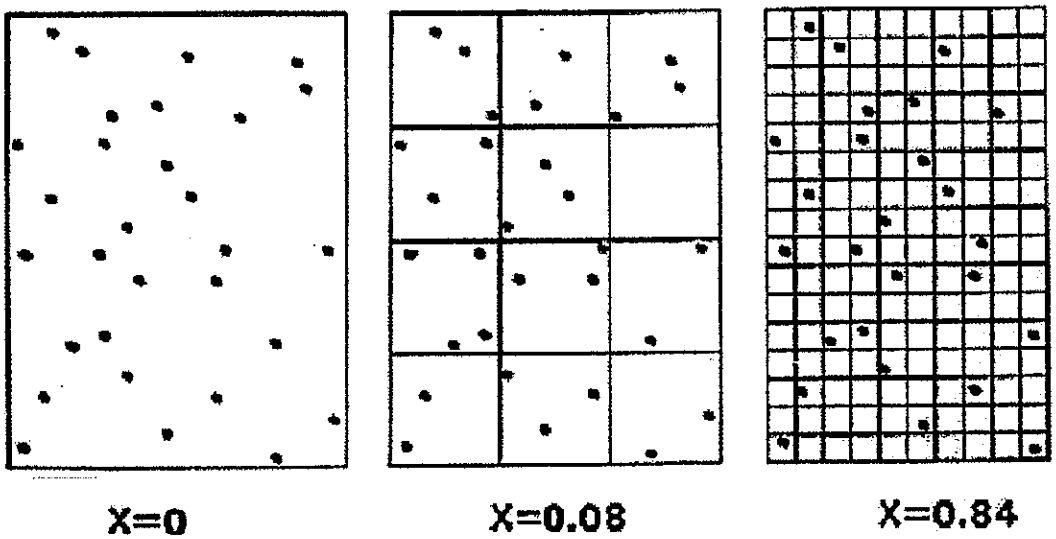

Figure 9: Diagram illustrating mote isolation effect [28].

The reason adiabatic cooling is possible in the smaller particles is due the heat of fusion as compared to the amount of solid. During gas atomization, the heat of fusion created as a result of the solidification process at the solid/liquid interface is adsorbed by the previously solidified material, which acts as a heat sink. Heat transfer is no longer limited by the rate at which it can be adsorbed by the atomization chamber environment, but, instead, it is controlled by the rate at which heat can be adsorbed by the solid present in the particle. The solid in the particle will be able to adsorb heat at a higher rate than transfer to the surrounding atmosphere. Figure 10 gives examples of how solidification takes place in the largest and the smallest particles. For the largest particles solidification is slower than the heat transfer and, therefore, follows isothermal path "A". In the smallest particles, where completely adiabatic cooling is possible, heat of fusion is not great enough to influence the velocity of the solidification front, so no change in microstructure or segregation will be present; path "B". Generally, atomized droplets will see a mixture of adiabatic and isothermal solidification. The particles will solidify adiabatically until recalescence raises the temperature of the particle enough to slow the solid/liquid interface velocity. This is the general case, as seen in path "C" [30].

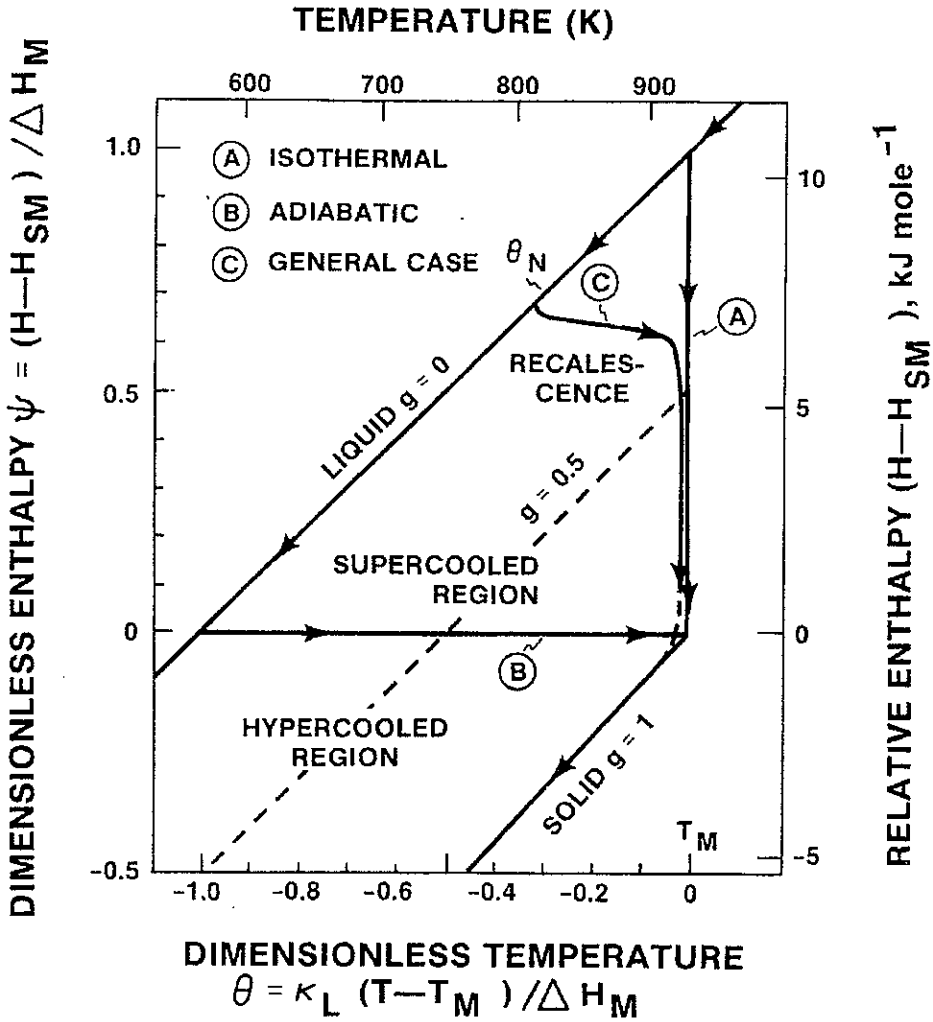

Figure 10: Possible adiabatic and isothermal cooling paths for atomized droplets with the effect of recalescence considered [30].

HPGA and melt-spinning are both able to produce PM powder. Melt-spinning has an advantage over HPGA in the fact that samples can be done on a laboratory scale, ~8g per run. The smallest batch for HPGA on the other hand is about 5kg and the atomization run itself is more labor intensive than melt-spinning. Due to sample size and staff time, alloy design iterations were completed using melt spinning. It was suggested by Branagan et al that it was possible to create atomized powders with an optimal to overquenched microstructure similar to those seen in melt-spinning [31]. $Nd_2Fe_{14}B$ was able to be atomized with an optimally quenched microstructure in particles that ranged from 5-10μm [31].

Cooling rate is a major determining factor in the structures that form in the atomized powders and in the melt-spun particulate. The cooling rate for melt-spun ribbon was determined using Equation 2 [32]. The output of this model is an average cooling rate given as a function of ribbon thickness. Determining local cooling rates uses microstructure parameters, such as secondary dendrite arm spacing (SDAS), as a measure of cooling rate. In Equation 2, R is the cooling rate, n is the form factor (n = 1 for ribbon), h is the heat-transfer coefficient, T is the temperature of the melt, T_A is the ambient temperature (room temperature in most cases), C_p is the latent heat per unit mass, ρ is the density of the melt, and d is the thickness of the ribbon. These variables give a good estimation of the average cooling rate based on ribbon thickness. Heat transfer coefficients ranged from 10^5 W/m^{2}K to 10^6 W/m^{2}K, which is considered the maximum possible for melt spinning were determined by Shunpei et al and Liebermann, respectively [32, 33]. Cooling rates as determined by Kramer experimentally for $Nd_2Fe_{14}B$ at wheel speeds of 5 and 20m/s, were $4.6x10^5$ and $4.2x10^6$K/s, respectively. These will be used to provide reference between theoretical and actual cooling rates [34].

$$R = \frac{nh(T - T_A)}{C_p \rho d} \tag{2}$$

For atomized powders where the cooling rate is dependent on particle size, the following equations can be used to find the average cooling rate for a range of particle diameters. The determination of local cooling rates and the effect of recalescence due to the motion of the solid/liquid interface will use microstructural features, SDAS for example, for determination of exact relative cooling rates inside the particle.

Equation 3 determines the Reynold's number (Re) where v is the velocity of the atomizing gas, D is the particle diameter, ρ_f is the density of the atomizing gas, and μ_f is the viscosity of the atomizing gas.

$$\mathrm{Re} = vD\frac{\rho_f}{\mu_f} \tag{3}$$

The Prandtl number, shown in Equation 4, is related to C_f, the specific heat, μ_f is the viscosity of the atomizing gas, and k_f is the conductivity of the atomizing gas.

$$\mathrm{Pr} = C_f \frac{\mu_f}{k_f} \tag{4}$$

These values are then used in Equation 5 to find heat transfer coefficient h, which is the measure of how effectively heat can be moved from the solidifying material to the associated heat sink.

$$h = k_f D^{-1}\left[2.0 + 0.60\,\mathrm{Re}^{1/2}\,\mathrm{Pr}^{1/3}\right] \tag{5}$$

The heat transfer coefficient is then used in Equation 6 along with T, the temperature of the droplet, T_o, the ambient temperature, ρ, the alloy density, C_p, the average heat capacity, and R, the radius of the droplet, to find the average cooling rate, ε_{Avg} [35].

$$\varepsilon_{Avg} = \frac{dT}{dt} = \frac{3h(T - T_o)}{\rho C_p R} \tag{6}$$

The calculated values for atomized powders may not correlate exactly to what is expected when comparing the two models due to unforeseen conditions that affect the cooling rate. Measuring cooling rates of atomized particles is very difficult due to the chaotic nature of the process, so Equations 3-6 are actually a best estimate of the average cooling rate.

PM Powder Consolidation Methods

There are two industrially useful forms of a $RE_2Fe_{14}B$ PMs. One type is the sintered fully dense PM. Sintered fully dense magnets come in two forms; isotropic and anisotropic. Sintered fully dense PMs have excellent magnetic strength, but they are extremely difficult to machine due to their brittle nature [36] and are prone to corrosion, which leads to irreversible loss of magnetic properties [37]. The other technologically useful type is the isotropic polymer bonded PM. Anisotropic polymer bonded PMs, made with anisotropic powders, have been made with BH_{max} values ~27MGOe under laboratory conditions, but are difficult to make in mass quantities [38]. The second form of bonded PM made with $RE_2Fe_{14}B$ is the

isotropic polymer bonded PM. Isotropic polymer bonded PMs use metal powders, resulting from rapid solidification processing, and are mixed with an epoxy or thermoplastic polymer, depending on temperature requirements. Bonded isotropic PMs will not be as strong magnetically as sintered PMs, but they offer the advantages of mass production and net shape formability.

Sintered fully dense PMs can be made from powders produced via HDDR or rapid solidification. $Nd_2Fe_{14}B$ has a low melting liquid which makes it ideal for liquid phase sintering. The low melting liquid is neodymium-rich and it is found on the grain boundaries [39] of sintered magnets. The neodymium on the grain boundaries suppresses the nucleation of reverse domains in large grains (1-5μm) [39]. The powders are consolidated in a green compact. During this phase the magnets can made either isotropic or anisotropic depending on the specifications of the application they are intended for. In isotropic PMs, the magnetic moments are randomly oriented based on the physical positioning of each powder particle. The magnet is then liquid phase sintered with the random orientation of the magnetic moments. In anisotropic PMs, the magnetic moments of each particle are aligned by applying a magnetic field to the mold during the compaction phase [40]. The magnetic moments in each particle physically rotate and reposition the particles so that the moment lies in line with the magnetic field. Aligning the magnetic moments of each particle increases the magnetic strength of the PM. In contrast, $MRE_2Fe_{14}B$ does not have a low melting liquid phase. Thus, if sintered fully dense PMs were made, higher temperatures would be required to sinter the material. Higher temperatures could induce more grain growth, eliminating the preferred nanoscaled microstructure and allowing for enhanced nucleation of reverse domains in the grains, leading to reduced coercivity.

As stated earlier $MRE_2Fe_{14}B$ is being processed via melt-spinning and HPGA to achieve a nanoscaled grain structure. Melt-spinning would seem like the optimal processing method because of the process control and the higher quench rates. However, the next step in the evolution of $MRE_2Fe_{14}B$ is to put it into the form of a polymer bonded magnet. Now considerations must be made that relate to optimizing the polymer processing of these polymer bonded magnets (PBMs). The ribbon that comes from the melt spinning process must be crushed into a powder. The powder has a flake, or plate, geometry. This geometry

lowers the packing factor of the powder in the PBM and increases the injection pressure needed for injection molding. The amount of powder in the PBM directly relates to the BH_{max}. Equation 7 shows how the amount of powder in a PBM relates to BH_{max} [2].

$$(BH_{max})^{bond} = f^2(BH_{max}) \tag{7}$$

Example
$f = .60$, $(BH_{max})^{bond} = 36\%\ (BH_{max})$
$f = .71$, $(BH_{max})^{bond} = 50\%\ (BH_{max})$

The BH_{max} of a polymer bonded magnet is equal to the square of the fill factor (fill factor being the vol% magnet powder in the PBM). Following this equation, a PBM with a fill factor of 70% will have 50% of the BH_{max} possible for the PBM, compared to an isotropic sintered fully dense PM of the same material. Spherical powders are created directly with the HPGA process. This is where processing the $MRE_2Fe_{14}B$ magnet alloys via HPGA has a distinct advantage. Spherical powder keeps the relative viscosity of the polymer blend low at high solids loading percentages. This gives spheres a distinct advantage over disks, equivalent to flake powders, created by crushing melt spun ribbon (see Figure 10) [41].

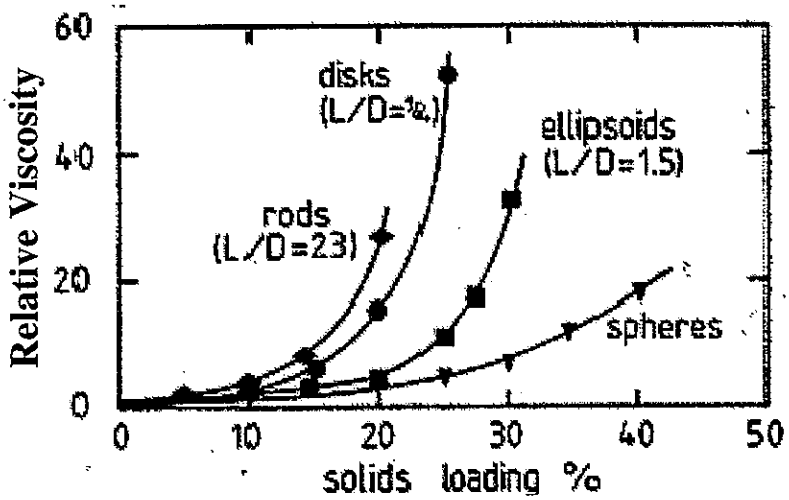

Figure 10: Viscosity of polymer blended with different shape powders. Disks would be the equivalent to the flake geometry of the melt spun powders [41].

$MRE_2Fe_{14}B$ is being designed for high temperature applications, so a high temperature polymer is needed to bind the particles. Nylon and epoxy currently used as binders commercially will soften in the temperature range in which $MRE_2Fe_{14}B$ is intended to operate, 150-200°C. Thus, polyphenyl sulfide (PPS) is the binder of choice. Since PPS has a melting temperature of 300°C, is non-reactive with the PM powders, is solvent resistant, is hydrophobic [42], and comes in a powder form that can be blended with the $MRE_2Fe_{14}B$ powders, PPS is preferred to make a feed stock for injection or compression molding.

Protective Fluoride Coating

The rare earth elements in $MRE_2Fe_{14}B$ make it prone to corrosion, which, as stated earlier, is detrimental to the magnetic properties. Sintered fully dense PMs can be plated with nickel after sintering to act as a barrier to corrosion. Polymer bonded magnets use the polymer matrix as a corrosion barrier by encapsulating the PM powders but the polymer matrix is not a true hermetic seal. While polymer binders provide a reasonable form of protection, additives in the polymer matrix could also attack the PM powders. Therefore, there is a need to develop a passive coating for the powders. A modified fluidized bed process could be used to grow a passive layer around each individual particle [43]. A fluoride coating is an option, since it could readily react with the rare earth elements on the surface of the particle to create a protective fluoride layer [43]. This would sacrifice the material on the surface layer of each particle, but will protect the rest of the particle, allowing $MRE_2Fe_{14}B$ to operate in increasingly hostile environments.

References

1. D.C. Jiles. *Introduction to Magnetism and Magnetic Materials.* Chapman and Hall. London ; New York. 1991.

2. D. Goll, H. Kronmüller. "High performance permanent magnets". *Naturwissenschaften.* 87 (2000) 423-438.

3. G.C. Hadjipanayis, "Nanophase hard magnets". *Journal of Magnetism and Magnetic Materials.* 200 (1999) 373-391.

4. I.E. Anderson, W. Tang, R.W. McCallum. "Particulate processing and high-performance permanent magnets". *International Journal of Powder Metallurgy.* Vol

5. ISURF 02935, McCallum, R.W., Xu, Youwen, Kramer, M.J., Anderson, I.E., and Dennis, K.W. "Permanent Magnet Alloy with Improved High Temperature Performance"

6. T.R. Anantharaman, C. Suryanarayana. *Rapidly Solidified Metals.* Trhans Tech Publications. Switzerland. 1987.

7. A. Hütten. "Processing, Structure, and Property Relationships in Nd-Fe-B Magnets". *JOM* March (1992), 11-15.

8. R. Hermann, O. Filip. "Influence of melt convection on the microstructure of levitated and undercooled Nd-Fe-B alloys". *Journal of Magnetism and Magnetic Materials.* 263 (2003) 15-20.

9. W. Tang, K.W. Dennis, Y. Q. Wu, M.J. Kramer, I.E. Anderson, and R.W. McCallum. "Studies of new YDy-based $R_2Fe_{14}B$ magnets for high temperature performance (R=Y+Dy+Nd)". *IEEE Transactions on Magnetics.* 40 (4), July 2004.

10. W. Tang, K.W. Dennis, Y.Q. Wu, M. J. Kramer, I. E. Anderson and R. W. McCallum "New YDy-based $R_2(Fe,Co)_{14}B$ Melt-spun Magnets (R=Y+Dy+Nd)", Presented in The 5th Pacific Rim International Conference on Advanced Materials and Processing, November 2-5, 2004. Beijing, China.

11. W. Tang, K.W. Dennis, Y. Q. Wu, M. J. Kramer, I. E. Anderson and R. W. McCallum, "Effect of Zr substitution on microstructure and magnetic properties of new YDy-based $R_2Fe_{14}B$ magnets (R=Y+Dy+Nd)", Presented in the 49th Annual Conference on Magnetism and Magnetic Materials, Jacksonville, Florida, November, 7-11, 2004.

12. G. Ya. Merkulova, L. Margulies, K.W. Dennis, and R.W. McCallum. "The temperature dependence of coercivity in nanocrystalline Nd-Fe-B-(TiC) magnets", *Journal of Applied Physics.* Volume 87, Number 9 (2000).

13. ASM International, Handbook of Ternary Phase Diagrams, 1995.

14. E.T. Teatum, K.A. Gschneidner, Jr. and J.T. Waber. "Compilation of calculated data useful in predicting metallurgical behavior of the elements in binary alloy systems", Los Alamos Scientific Laboratory of the University of California. (1968).

15. W. Hume-Rothery, R.E. Smallman, C.W. Haworth. *The Structure of Metals and Alloys.* 5th Ed. The Metals and Metallurgy Trust of the Institue of Metals and the Institution of Metallurgists. London. 1969.

16. M. Takahashi, K. Uchida, F. Tniguchi, and T. Mikamoto. "High performance Nd-Fe-B sintered magnets mad by the wet process", *Journal of Applied Physics*. Volume 83, Number 11 (1998).

17. A. Zern, M. Seeger, J. Bauer, H. Kronmüller. "Microstructural investigations of exchange coupled and decoupled nanocrystalline NdFeB permanent magnets". *Journal of Magnetism and Magnetic Materials.* 184 (1998) 89-94.

18. R. Fischer and H. Kronmüller. "The role of grain boundaries in nanoscaled high-performance permanent magnets". *Journal of Magnetism and Magnetic Materials.* 184 (1998) 166-172.

19. Y. Kawashita, N. Waki, T. Tayu, T. Sugiyama, H. Ono, H. Koyama, H. Kanno, and T. Uchida. "Magnetic properties of Nd-Fe-B system anisotropic HDDR powder made from segregated master ingots." *Journal of Magnetism and Magnetic Materials.*

20. M.C. Flemings. *Solidification Processing*. McGraw-Hill, New York, 1974.

21. W. Pei, C. He, F. Lian, G. Zhou, and H. Yang. "Structures and magnetic properties of sintered Nd-Fe-B magnets produced by strip casting technique". *Journal of Magnetism and Magnetic Materials.* 239 (2002) 475-478.

22. J. Bernardi, J. Fiddler, M. Sagawa, Y. Hirose. "Microstructural analysis of strip cast Nd-Fe-B alloys for high $(BH)_{max}$ magnets". *Journal of Applied Physics.* Volume 83, Number 11, 1 June 1998. 6396-6398.

23. M.A. Otooni. *Elements of Rapid Solidification*. Springer-Verlag. Berlin. 1998.

24. Y.L. Tang, M.J. Kramer, K.W. Dennis, R.W. McCallum, and L.H. Lewis. "On the control of microstructure in rapidly solidified Nd-Fe-B alloys through melt treatment". *Journal of Magnetism and Magnetic Materials.* 267 (2003) 307-315.

25. D.J. Branagan, R.W. McCallum. "Altering the cooling rate dependence of phase formation during rapid solidification in the $Nd_2Fe_{14}B$ system". *Journal of Magnetism and Magnetic Materials.* 146 (1995) 89-102.

26. W.J. Boettinger, J.H. Perepezko. "Fundamentals of Rapid Solidification". *Rapidly Solidified Crystalline Alloys.* Edited by, S.K. Das, B.H. Kear, C.M. Adam. The Metallurgical Society, Pennsylvania. 1985.

27. I.E. Anderson and B.B. Bath. "Rapid Solidification of Copper-Based Alloys". *Rapidly Solidified Crystalline Alloys.* Compiled by S.K. Das, B.H. Kear, and C.M. Adam, TMS-AIME, Morristown, NJ, May 1-3, 1985, 219-244.

28. I.E. Anderson and M.P. Kemppainen. "Undercooling Effects in Gas Atomized Powders". *Undercooled Alloy Phases*, E.W. Collings and C.C. Koch Eds., 1986, TMS-AIME, New Orleans, p 269.

29. A.L. Genau, R. Trivedi, I.E. Anderson. "Microstructure selection during raid solidification of Al-Si powders". 2004 International Conference on Powder Metallurgy and Particulate Materials. Chicago, IL. June 13-17, 2004.

30. M. Cohen and R. Mehrabian. "Some fundamental aspects of rapid solidification", *Rapid Solidification Processing Principles and Technologies, III.* Editor—R. Mehrabian. (1982).

31. D.J. Branagan, T.A. Hyde, C.H. Sellers, and R.W. McCallum. "Developing rare earth permanent magnet alloys for gas atomization". *Journal of Physics D: Applied Physics.* 29 (1996) 2376-2385.

32. O. Shunpei, Tetsuji Saito, Tetsuichi Motegi. "Effects of cooling rate on microstructures and magnetic properties of Nd-Fe-B alloys". *Journal of Alloys and Compounds.* 363 (2004) 263-270.

33. H.H. Liebermann and R.L. Bye, Jr. "Rapid solidification processing and its effects on microstructure of metallic alloy strip," *Rapidly Solidified Crystalline Alloys.* Edited by S.K. Das, B.H. Kear, and C.M. Adam. The Metallurgical Society, Inc. (1985) 61-76.

34. M. J. Kramer H. Mecco, K.W. Dennis, E. Vargonova, R.W. McCallum and R E. Napolitano. "Rapid Solidification and Metallic Glass Formation – Experimental and Theoretical Limits. Presented in The 12th International Conference on Liquid and Amorphous Metals, 11 - 16 July, 2004, Metz, France.

35. R. Mehrabian. "Relationship of heat flow to structure in rapid solidification processing". *Rapid Solidification Processing.* Claitor's Publishing Division, Baton Rouge. (1978) 9-27.

36. A. Li, W. Li, S. Dong, X. Li. "Sintered Nd-Fe-B magnets with high strength". *Journal of Magnetism and Magnetic Materials.* 265 (2003) 331-336.

37. J. Xiao and J. Otaigbe. "Polymer bonded magnets III. Effect of surface modification and particle size on the improved oxidation and corrosion resistance of magnetic rare earth fillers". *Journal of Alloys and Compounds.* 309 (2000) 100-106.

38. N. Hamada, C. Mishima, H. Mitarai, and Y. Honkura. "Development of Nd-Fe-B Anisotropic Bonded Magnet with 27 MGOe".

39. J. Fidler, K.G. Knoch, H. Kronmüller, and G. Schneider. "Analytical TEM study of Al-doped, "two-phase" Nd-Fe-B sintered magnets," *Journal of Materials Research.* Vol. 4 No. 4 (1989) 806-814

40. F. Vial, F. Joly, E. Nevalainen, M. Sagawa, K. Hiraga, and K.T. Park. "Improvement of coercivity of sintered NdFeB permanent magnets by heat treatment," *Journal of Magetism and Magnetic Materials.* 242-245 (2002) 1329-1334.

41. R. M. German, *Powder Injection Molding*, First Edition ed: Metal Powder Industries Federation, Princeton, New Jersey, 1990.

42. Ticona. "Designing with Fortran Polypenylene Sulfide" http://www.ticona.com/tools/search/lit_details.cfm?docid=27. [Accessed 18 June 2005]

43. M.L. Anderson. Surface Passivation and Electrochemical Behavior of Gas Atomized $LaNi_{4.75}Sn_{0.25}$ for Battery Applications. Masters Thesis. Iowa State University. (2000)

CHAPTER 2: COMPARISON OF MIXED RARE EARTH IRON BORIDE GAS ATOMIZED POWDERS TO MELT SPUN RIBBON FOR BONDED ISOTROPIC PERMANENT MAGNETS

A paper published in *Advances in Powder Metallurgy & Particulate Materials - 2004*[1]

N.L. Buelow[2], I.E. Anderson[3*], R.W. McCallum[4], M.J. Kramer[5], W. Tang[6], and K.W. Dennis[7]

ABSTRACT

Bonded isotropic permanent magnets (BPMs) formed by injection or compression molding offer good corrosion resistance and the capability for net shape manufacturing. Substituting Y and Dy for Nd in $Nd_2Fe_{14}B$ results in a mixed rare earth iron boride ($MRE_2Fe_{14}B$) for use in BPMs. Microstructures of MRE-Fe-B powders directly affect the magnetic properties of the BPMs. Melt spinning has been used to process $Nd_2Fe_{14}B$ alloys to achieve the necessary grain structure to maximize the magnetic properties. Due to the plate-like particulate that results from melt spinning the maximum energy product may not exceed that achieved by spherical powders in an injection molded bonded magnet due to polymer compound viscosity and fill factor considerations. Producing spherical powders allows for a higher fill factor, increasing the maximum energy product. Gas atomization offers rapid solidification effects that promote glass formation or uniform fine microsegregation to the particulate and produces spherical particles. Comparisons of melt spun and gas atomized $MRE_2Fe_{14}B$ powder will be reviewed

---

[1] Reprinted with permission from ADVANCES IN POWDER METALLURGY & PARTICULATE MATERIALS 2004, Metal Powder Industries Federation, 105 College Road East, Princeton, New Jersey 08540

[2] Graduate student Materials Science and Engineering and primary author
[3] Adjunct Professor of Materials Science and Engineering and Ames Lab-USDOE Senior Metallurgist
[*] Author for correspondence
[4] Adjunct Professor of Materials Science and Engineering and Ames Lab-USDOE Senior Materials Scientist
[5] Adjunct Professor of Materials Science and Engineering and Ames Lab-USDOE Scientist II
[6] Ames Lab-USDOE Post Doctoral Fellow
[7] Ames Lab-USDOE Assistant Metallurgist

INTRODUCTION

The role of permanent magnets (PMs) has been continually evolving for the past 20 years, since the discovery of Rare Earth $(RE)_2Fe_{14}B$ PMs that posses improved magnetic strength at relatively low cost [1]. Applications in the field of medicine, computer technology, and automotive technology are growing and need new and refined magnetic materials with increasingly better properties [2]. The next generations of hybrid automobiles require magnets that can be easily molded, have high BH_{max}, and improved temperature characteristics [3].

Traditional $RE_2Fe_{14}B$ alloys have been a staple in PM technology. Large amounts of research have been dedicated to reducing precipitation of α-Fe, to increasing BH_{max} through alloying and processing techniques, and to increasing the Curie temperature [4-6]. Increasing the Curie temperature of $RE_2Fe_{14}B$ magnet alloys has helped their high temperature performance; however, it did little to stabilize magnetic properties over a temperature range. As operating temperature increases from room temperature, the BH_{max} of $RE_2Fe_{14}B$ magnet degrades [7]. This is an issue facing automakers and a problem that is being addressed at Ames Laboratory though the development of a novel PM alloy, mixed rare earth iron boride ($MRE_2Fe_{14}B$) [3].

The driving force behind $MRE_2Fe_{14}B$ is the retention of magnetic properties at increased operating temperature [3]. This is accomplished by combining three 2-14-1 phases, in what is assumed to be an "ideal" alloying behavior. $MRE_2Fe_{14}B$ alloys exhibit magnetic properties that correspond to the "symbiosis" of the three 2-14-1 phases present, e.g. thermal stability of magnetocrystalline anisotropy seen in $Y_2Fe_{14}B$, thermal stability of the magnetic moment found in $Dy_2Fe_{14}B$, and increased BH_{max} from $Nd_2Fe_{14}B$ [8,6]. Another boost to the $MRE_2Fe_{14}B$ alloys can be derived by the addition of Co, which is well known to increase the Curie temperature of RE-Fe-B magnets [4]. This increase in Curie temperature should also extend the range of stable operating temperatures for $MRE_2Fe_{14}B$.

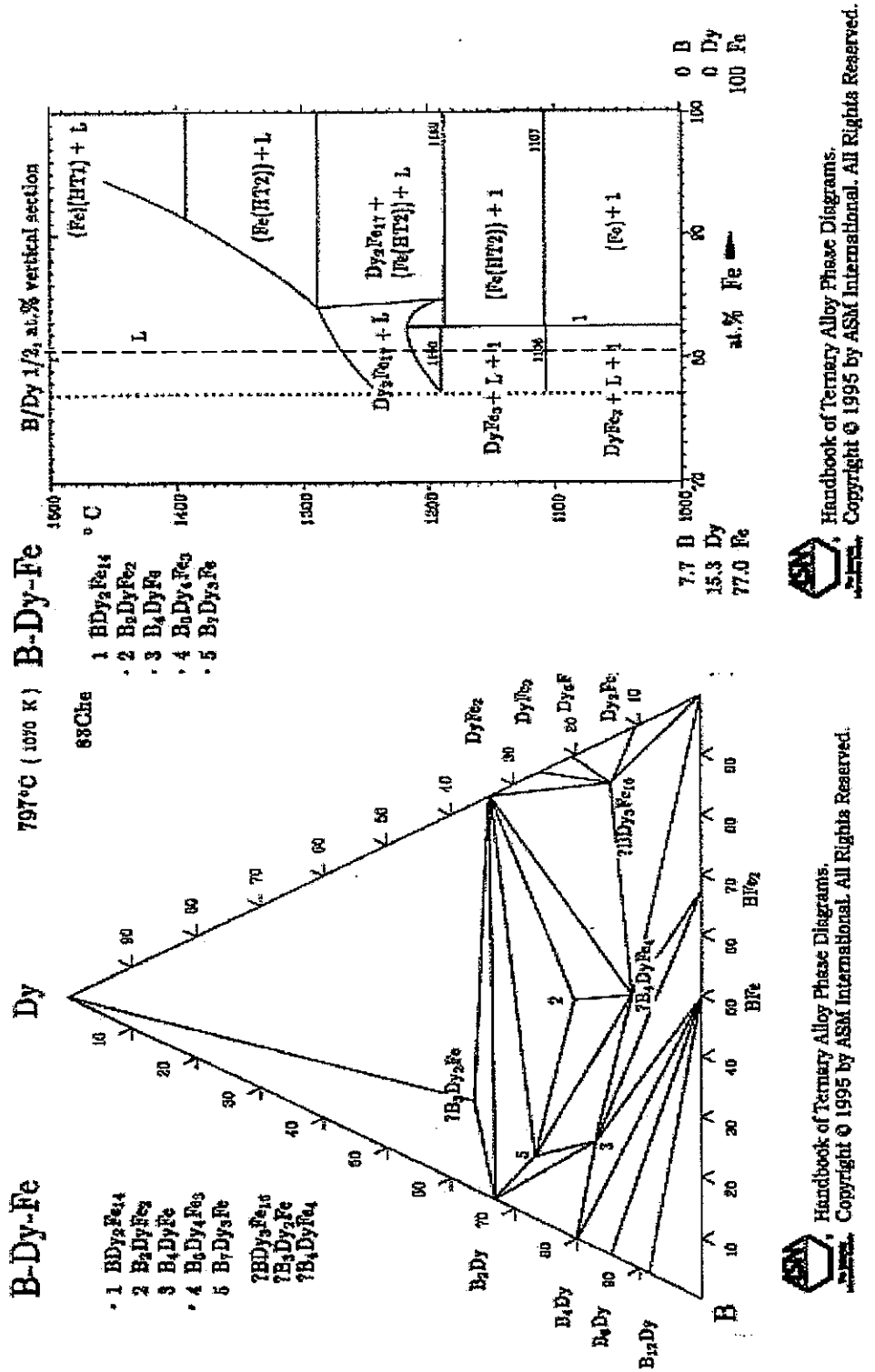

Figure 1: Dy-Fe-B phase diagram, isothermal and vertical section, with solidification path drawn in on the vertical section for the $MRE_2Fe_{14}B$ composition used in this study [9].

The solidification path for MRE-Fe-B is "expected" to closely resemble the path shown on Figure 1 on the Dy-Fe-B phase diagram. Presuming $MRE_2Fe_{14}B$ follows the Dy-Fe-B phase diagram means, there will be no low melting liquid in equilibrium with the hard magnetic phase making $MRE_2Fe_{14}B$ magnet alloy optimal for rapid solidification [3]. This equilibrium characteristic is unlike $Nd_2Fe_{14}B$ alloys which contain a small fraction of low melting eutectic that requires a cooling of around 600°C below the liquidus to completely eliminate liquid from the grain boundaries.

Microstructure and magnet alloy design have a direct effect on the magnetic properties through the linkage of solidification processing and annealing treatments [10]. Rapid solidification techniques have the ability to promote formation of the desired phases with microstructures needed for optimal magnetic properties. This has been proven in the production of other $RE_2Fe_{14}B$ magnet alloys.

Melt-spinning and atomization are being investigated as possible processing routes for $MRE_2Fe_{14}B$. The melt spinning technique gives direct control over the melt homogeneity, cooling rate and undercooling, and therefore microstructure, based on wheel speed [11,6]. The ribbon produced can be crushed, in an inert atmosphere, into a relatively fine powder with minimal loss of magnetic properties.

Polymer bonded magnets are cheaper to produce, have net shape formability, and the polymer binder can encapsulate the powder particle reducing irreversible loss due to oxidation and corrosion [7]. The reduction of light rare earth elements like Nd and Pr, which oxidize more readily than the heavy rare earths, also reduces irreversible loss due to corrosion [3]. However their downfall is in the area of magnetic energy density. A polymer bonded magnet will have a lower BH_{max} as compared to a fully dense sintered magnet of the same composition. The magnetic strength of a bonded magnet is dependent on the fill factor, f. The fill factor is the amount (in vol%) of magnetic material as compared to polymer binder [2], as follows:

$$(BH_{max})^{bond} = f^2(BH_{max}) \qquad (1)$$

As can be seen from equation (1) the strength of the bonded magnet is related to the square of the fill factor [4]. So a bonded magnet with a 71% fill factor will have 50% of the BH_{max} of a fully dense sintered magnet [2]. The geometry of flake powders creates difficulty in reaching a high fill factor. The flake geometry also has detrimental effects on the viscosity and flow characteristics of a polymer compound. The solution is to process $MRE_2Fe_{14}B$ particulate so that the active magnetic particulate has a spherical geometry. This increases the packing factor for the bonded magnets, since spheres have better flow characteristics needed for net shape forming. Creating spherical powders is easily accomplished with atomization in an inert environment [3].

High pressure gas atomization (HPGA) can create spherical powders with a very fine particle size. Particle size is dependent on the atomizing gas. For $MRE_2Fe_{14}B$, helium atomization gas is used to create a fine particulate with high yields that are less than 20μm. The sub-20μm particles are where the greatest undercooling is expected to be achieved for MRE-Fe-B as the catalysts for nucleation are more dispersed in the smaller particles [12].

Alloy design was completed using melt spinning due to the amount of material needed and quicker "turn-around", compared to HPGA. There are many different factors that could contribute to the differences in magnetic properties and microstructures seen in $MRE_2Fe_{14}B$ processed by HPGA and melt spinning [2,4,11]. The challenge lies in understanding how a $MRE_2Fe_{14}B$ magnet alloy composition that has great magnetic properties in ribbon form, can be modified to produce the same promising magnetic properties in the HPGA powder form. The difference seen in $MRE_2Fe_{14}B$ in the melt spun ribbon and HPGA powder are being investigated for this purpose.

EXPERIMENTAL PROCEDURE

The $MRE_2Fe_{14}B$ composition $[Nd_{0.5}(DyY)_{0.25}]_{2.2}Co_{1.5}Fe_{12.5}B$ was chosen for this investigation. Three different wheel speeds, 10, 16, and 22m/s, were used for melt spinning. All runs were completed in 1/3 atmosphere of helium. Samples from the three different wheel speeds were annealed, at temperatures of 700-800°C for 10-15min, to see how heat treatments affected the magnetic properties compared to the as-spun state.

The annealing process involved wrapping the ribbons in Ta foil. The Ta envelope was then sealed in a quartz capsule that had been evacuated and back filled with 1/3atm of UHP He gas. Both annealed and as-spun samples were tested for their magnetic properties, phases present, and morphology.

From the melt spinning results, alloys were selected for HPGA using helium as the atomizing gas. Helium was used to create a batch that had a high yield of sub 20μm particles. The composition $[Nd_{0.5}(DyY)_{0.25}]_{2.29}Co_{1.5}Fe_{12.5}B$ was prepared for HPGA. An extra 0.09 at% of the rare earths and yttrium were added to account for oxidation losses during the atomization process.

Samples of HPGA powder were sieved with ASTM screens for XRD to determine the phases present, and for magnetic measurements, determining remanence, coercivity, and BH_{max} as a function of particle size. To ensure the powders would not rotate in the field during magnetic measurement they were mounted in an epoxy. Powder samples were subjected to metallographic procedures to permit the morphology to be viewed with an SEM.

After determination of the as-atomized state, annealing effects on the HPGA powder were investigated using heat treatments of 700°C for 10min, 750°C for 15min, 800°C for 15min, and 1000°C for 24hr. The powder samples were also wrapped in a Ta envelope and sealed in a quartz capsule that had been evacuated and back filled with 1/3atm of UHP He gas. These powders were subjected to the same battery of tests for comparison to the as-atomized powders, as-spun ribbon, and annealed ribbons.

RESULTS

Ribbon samples were run at a wheel speed of 10m/s, attempting to underquench the $MRE_2Fe_{14}B$, and resulted in an unfavorable magnetic state, as seen from the magnetic results shown in Figure 4. Metallographic analysis showed an amorphous or nanocrystalline region on the wheel side of the ribbon, a transition midway through the ribbons thickness, and a probable two phase region on the free side, as illustrated in Figure 3. By examination of the phase diagram it is expected that the free side is MRE_2Fe_{17} and the wheel side is $MRE_2Fe_{14}B$. For this alloy system MRE_2Fe_{17} does not have the desired magnetic properties. XRD on the

free side and the wheel side of the ribbon sample established what primary phase was present on either side.

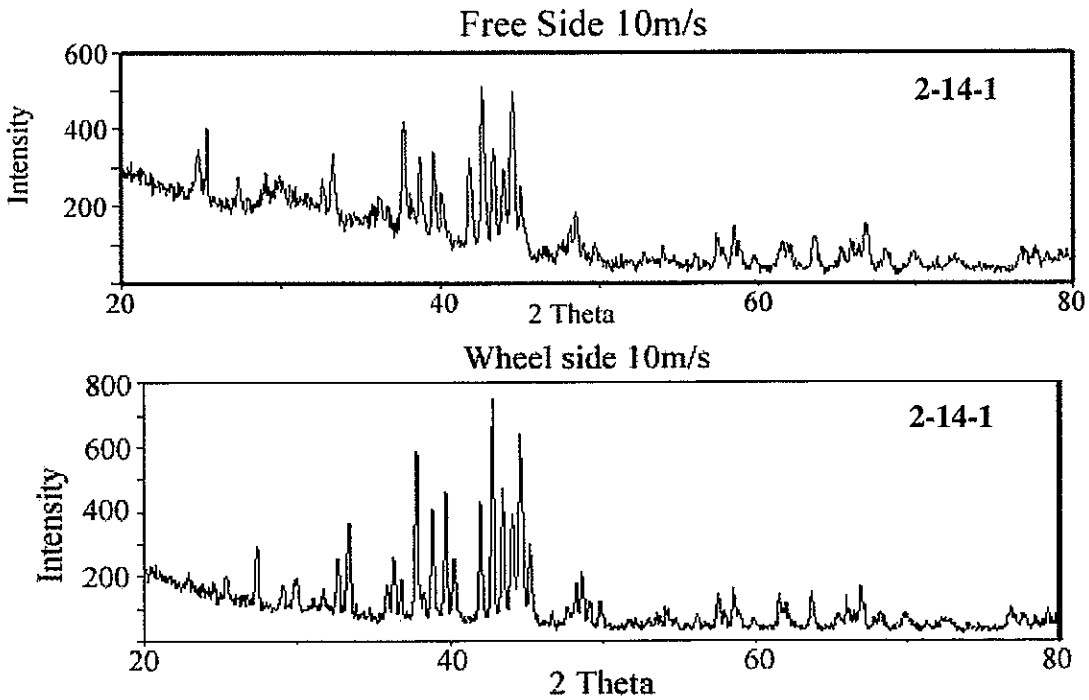

Figure 2: XRD traces for the free and wheel side of the 10m/s ribbon sample.

As seen from XRD results in Figure 2 the wheel side of the ribbon is predominantly an $MRE_2Fe_{14}B$ and the free side is an $MRE_2Fe_{14}B$, as well, with some indication of a secondary phase especially at low 2Θ angles. This means that the differences in the microstructure are due to differences in growth morphology and the onset of some microsegregation as solidification proceeds beyond the mid-thickness of the ribbon.

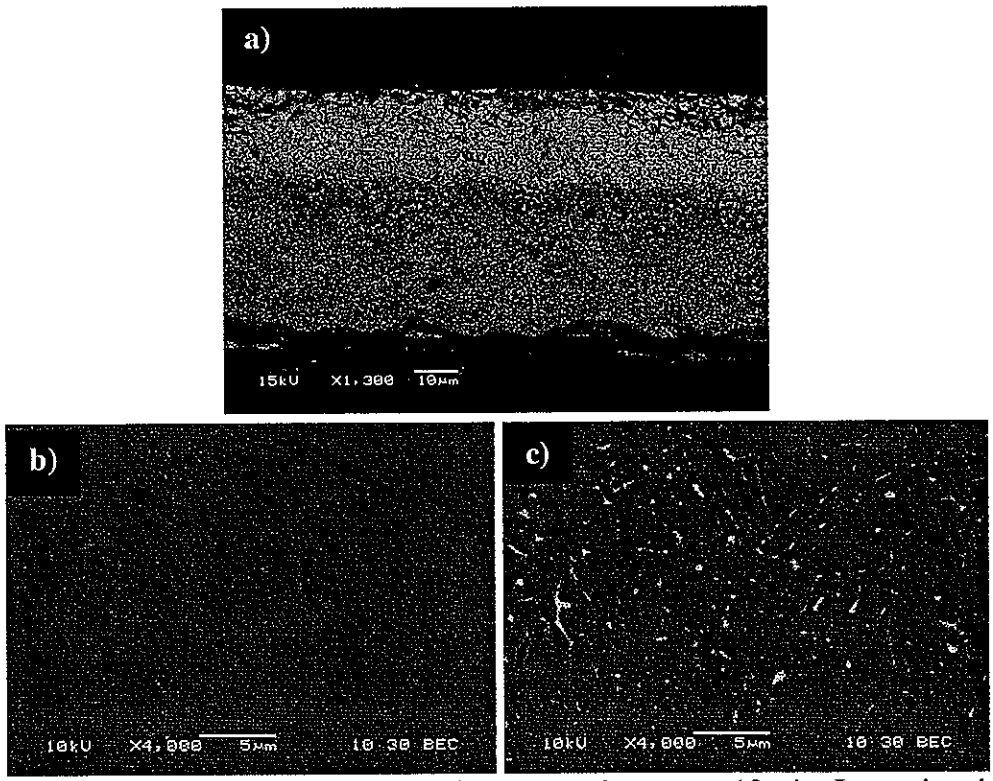

Figure 3: Etched and no etch $MRE_2Fe_{14}B$ ribbon sample spun at 10m/s. Image is oriented so the wheel side corresponds to the bottom of the micrograph and the free side to the top of the micrograph a) etched ribbon b) no etch wheel side c) no etch free side.

The magnetic results also show indications of a two-phase microstructure as seen in Figure 4. There is a dip in quadrant 2 and 4 that corresponds to a soft magnetic phase. However, since primary solidification of $MRE_2Fe_{14}B$ occurs on both sides of the ribbon the dip effect is likely to occur from extrinsic effects due to the second phase is present, which can be seen in the micrographs, but is not noticeable in the XRD trace. An annealing treatment of 750°C for 15min was performed on this material to try to equilibrate the microstructure. After annealing the magnetic loops still showed the same two phase magnetic behavior and the morphology of the free side and wheel side have not equilibrated, as seen in Figure 4.

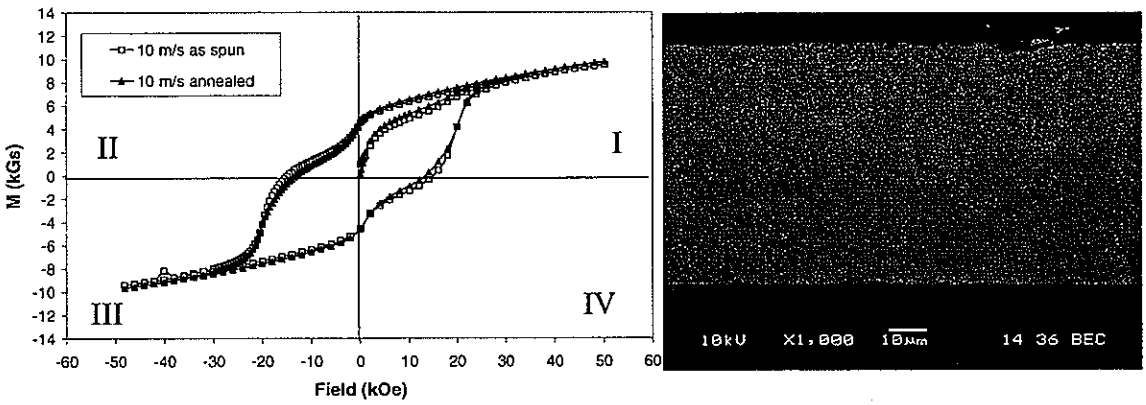

Figure 4: Hystresis loop for 10m/s sample again showing an apparent second phase in the material and micrograph of the annealed material.

The transition is seen across the length of the as-spun ribbon sample, and appears stable. Figure 5 is a collection of connected images that demonstrate the stability of the solidification feature across a distance on the ribbon.

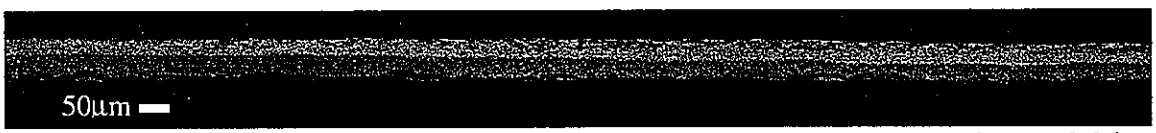

Figure 5: Image oriented with wheel side down. Length of image is 1.876mm x 0.06mm.

The amount of quenching seen in HPGA is lower than in melt-spun ribbon. This is due to the thermal conductivity difference of helium and copper. In addition, directionally of the solidification is different, due to the differences in quenching directionality. Ribbon samples will see higher solidification rate closer to the wheel surface and atomized powder will have the highest solidification rate on the surface of the particle and lowest at the center of the particle. Particle size will also affect the amount of undercooling, with particles finer than about 10µm diameter likely to experience completely adiabatic solidification at high undercoolings [14]. XRD traces show that the majority phase of the as-atomized $MRE_2Fe_{14}B$ powder is MRE_2Fe_{17}. The presence of MRE_2Fe_{17}, and lack of $MRE_2Fe_{14}B$, can again be seen in the magnetically soft hystresis loops for the as-atomized powders. This response is hardened after a 750°C anneal for 15 minutes increasing the coercivity from almost zero to

~8kOe. This increase was expected as the annealing treatment transformed the MRE_2Fe_{17} phase into the $MRE_2Fe_{14}B$ phase. This is seen in the XRD traces shown in Figure 6.

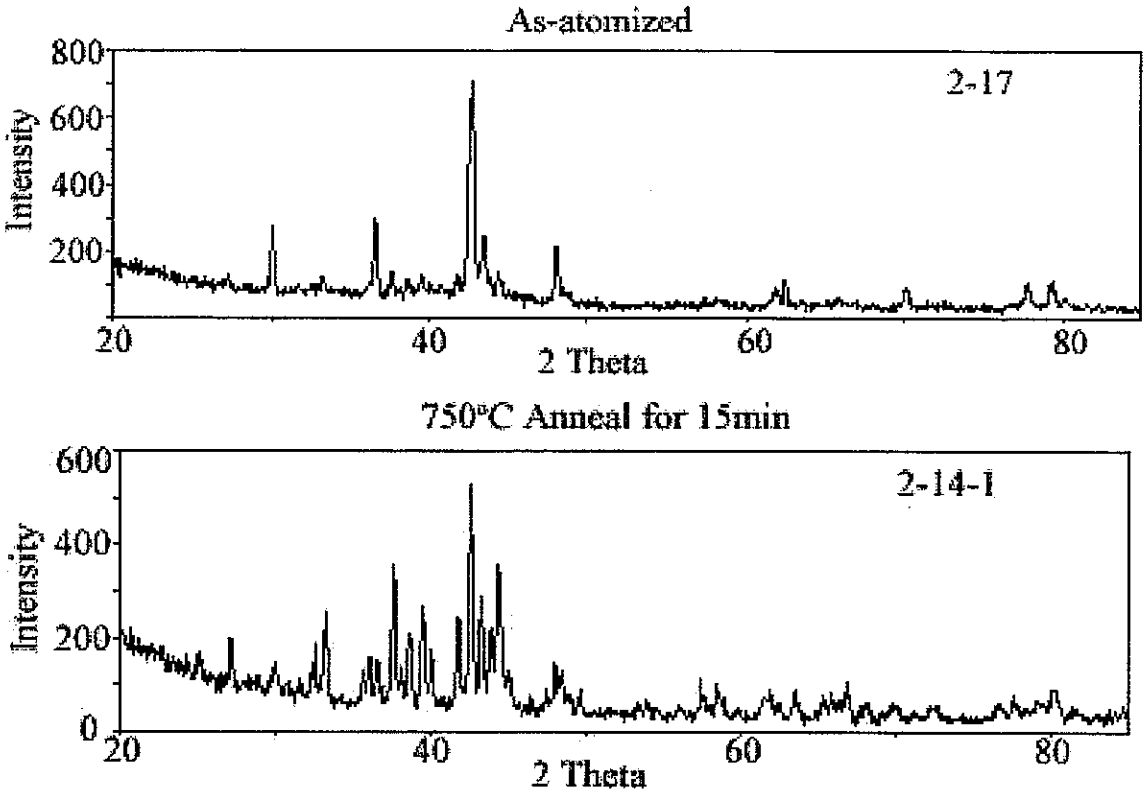

Figure 6: XRD trace of as-atomized and annealed powder.

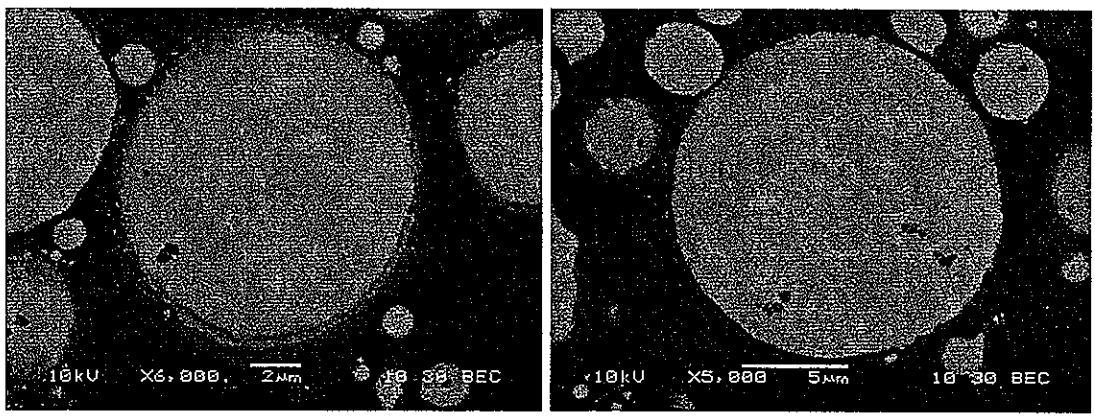

Figure 7: Microstructure of unetched as-atomized particles.

When comparing Figure 7 to Figure 3c similarities in the morphologies of the as-atomized powder and the free side of the melt spun ribbon are seen. A light phase separating a dark phase is present in both. On the free side of the melt-spun ribbon, the solidification rate may be similar to that of the sub 20μm HPGA powder. A comparison of the spacing width of the light regions in the 10m/s ribbon with that in the less than 20μm particles can be found in, Figure 8. A spacing of 0.24μm is the average spacing for the ribbon, where this spacing is seen in the HPGA powder at a particle size of ~16μm. However, it must be noted that the primary phase in the powder is MRE_2Fe_{17}, but the melt-spun ribbon has $MRE_2Fe_{14}B$ as the primary phase on the free side.

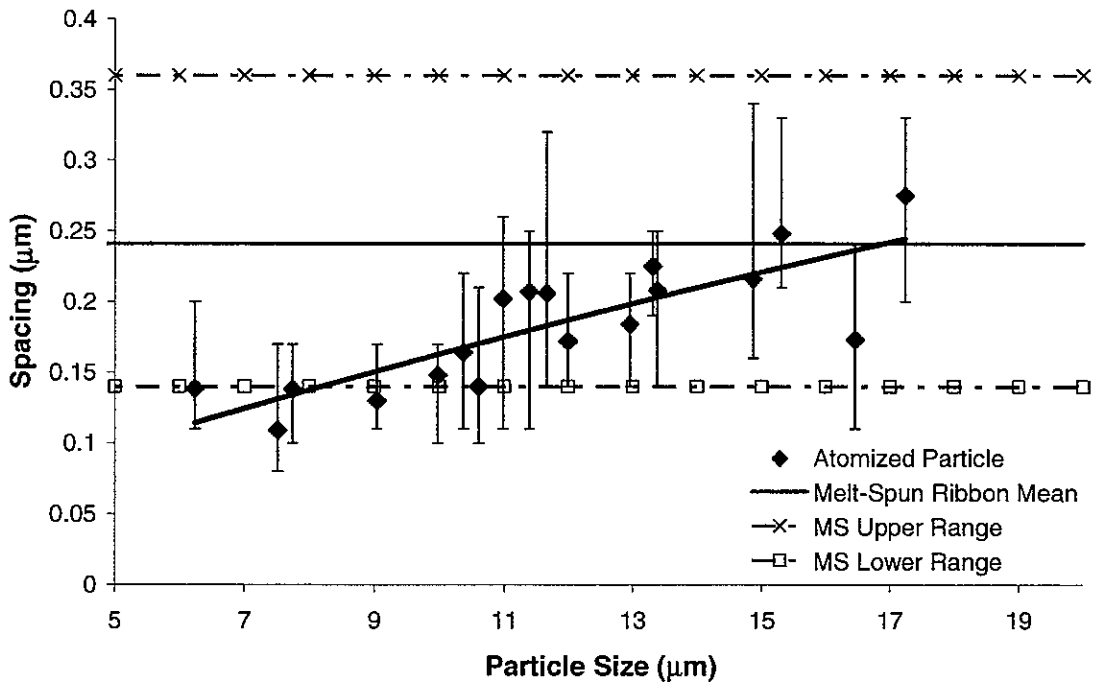

Figure 8: Spacing comparison between free-side of ribbon spun at 10m/s and –20μm powder. Dashed line represents average ribbon spacing and trend of spacing base on particle size is shown for the atomized $MRE_2Fe_{14}B$ powder.

DISCUSSION

Understanding what phases are forming and where they are forming is critical to the development of $MRE_2Fe_{14}B$. Due to the differences in melt spinning and HPGA processes, differing magnetic properties are being seen for the same $MRE_2Fe_{14}B$ composition. Looking

at the phase diagram it would seem that boron would be a deciding factor in how $MRE_2Fe_{14}B$ solidifies. In other words, the only phase in the Dy-Fe-B phase diagram that would consume boron from the melt is $MRE_2Fe_{14}B$ phase. The boron could be consumed in that phase or possibly in the $MRE_1Fe_4B_4$ phase, as predicted on the Nd-Fe-B phase diagram. Figure 9 demonstrates how $MRE_2Fe_{14}B$ might solidify.

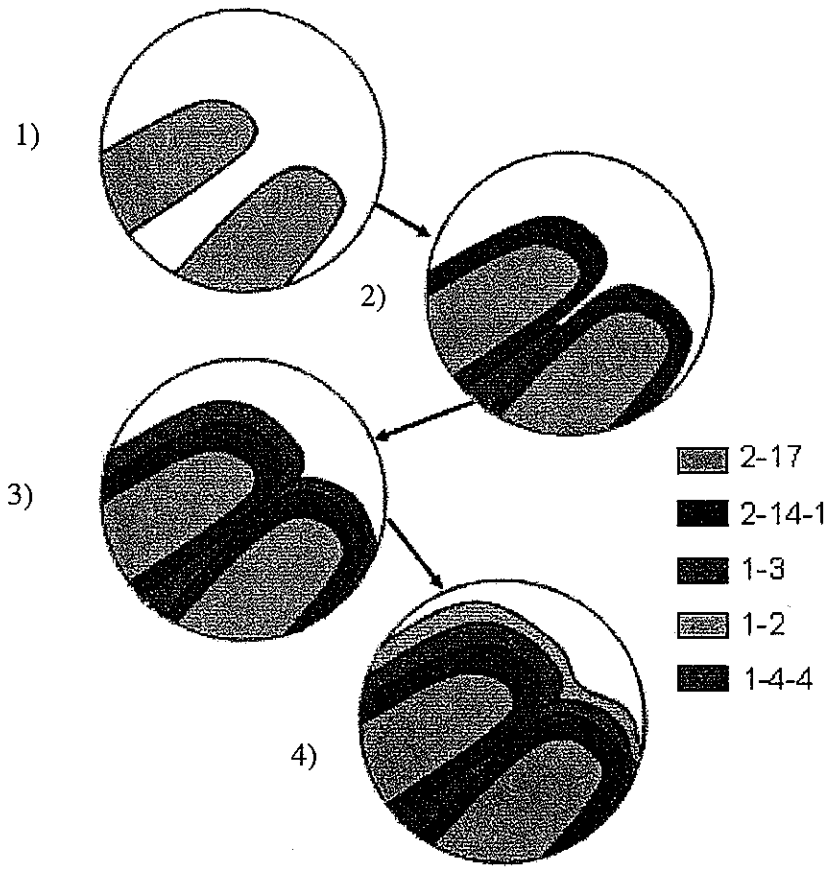

Figure 9: Schematic of possible solidification pattern seen in MRE for atomized powders.

Since MRE_2Fe_{17} is the majority phase in the HPGA powders, as determined from XRD results, MRE_2Fe_{17} must be the primary solidification product for this composition of $MRE_2Fe_{14}B$ in the as-atomized state. The next phase to nucleate will be the $MRE_2Fe_{14}B$ phase and will likely form a layer around the MRE_2Fe_{17} primary phase. Due to possible boron enrichment in the interdendritic region, it is likely that $MRE_2Fe_{14}B$ jumps to the behavior of the Nd-Fe-B phase diagram and creates the $MRE_1Fe_4B_4$ phase. As the material continues to cool, other possible phases could form creating a layered morphology.

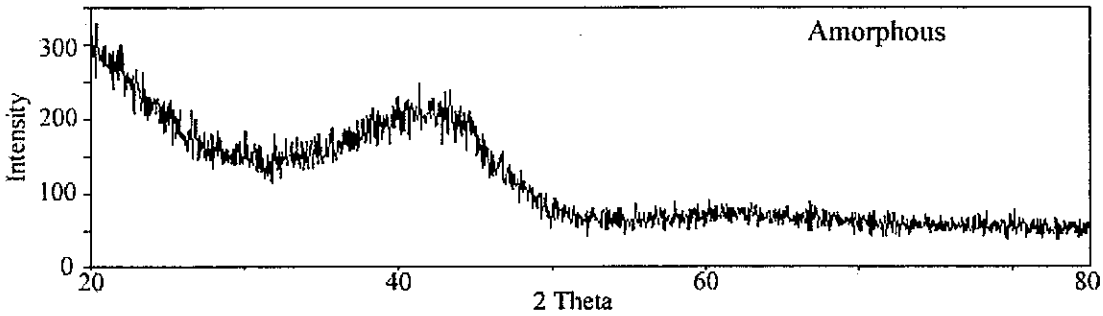

Figure 10: XRD trace for 16m/s as-spun.

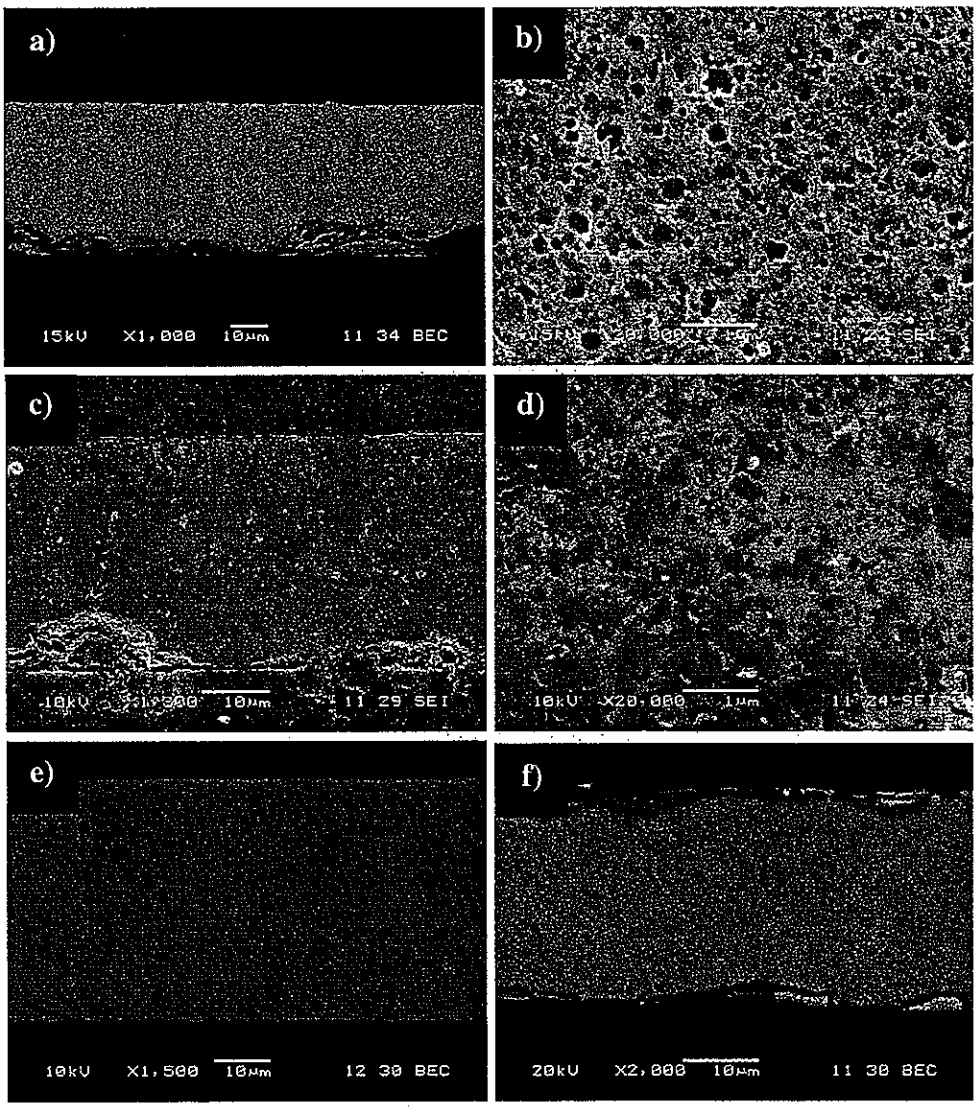

Figure 11: As-spun 16 and 22m/s ribbon etched and not etched. a) 16m/s etched b) 16m/s etched high magnification c) 22m/s etched d) 22m/s etched high magnification e) 16m/s no etch f) 22m/s no etch.

As expected, large amounts of quenching would result in the formation of $MRE_2Fe_{14}B$ in a nanocrystalline or amorphous structure. Wheel speeds of 16 and 22m/s did not show the growth morphology transition that was very apparent in the ribbon spun at 10m/s ribbon. XRD results, in Figure 10, (for 16m/s) show it to be an amorphous structure. Some nanocrystalline structures seem to be present, in the ribbon spun at 16m/s, which can be assumed from the magnetic results in Figure 12. Figure 11 contains the SEM micrographs for these samples.

At a wheel speed of 22m/s an amorphous structure was created and a subsequent annealing treatment of 700°C for 15min formed a microstructure in the material that possessed good hard magnetic properties. Figure 12 also shows the affect of a temperature increase on the magnetic properties of $MRE_2Fe_{14}B$. Coercivity is the property most affected, but even at 400K $MRE_2Fe_{14}B$ still has a BH_{max} of 8.72MGOe compared to 10.42MGOe for the room temperature measurement.

The annealing treatments used on ribbons made at wheel speeds of 10m/s and 16m/s did not significantly improve their magnetic properties. This is probable after the phenomenon seen in the less than 20μm as-atomized powder annealed at 1000°C for 24hrs. After such a treatment traditional $RE_2Fe_{14}B$ magnets would exhibit soft magnet characteristics due to extensive grain growth, an unknown mechanism in $MRE_2Fe_{14}B$ suppresses, this allowing the material to retain some of its magnetic properties as seen in Figure 13. The same mechanism may inhibit phase and morphology transformation in the 10 and 16m/s ribbon samples.

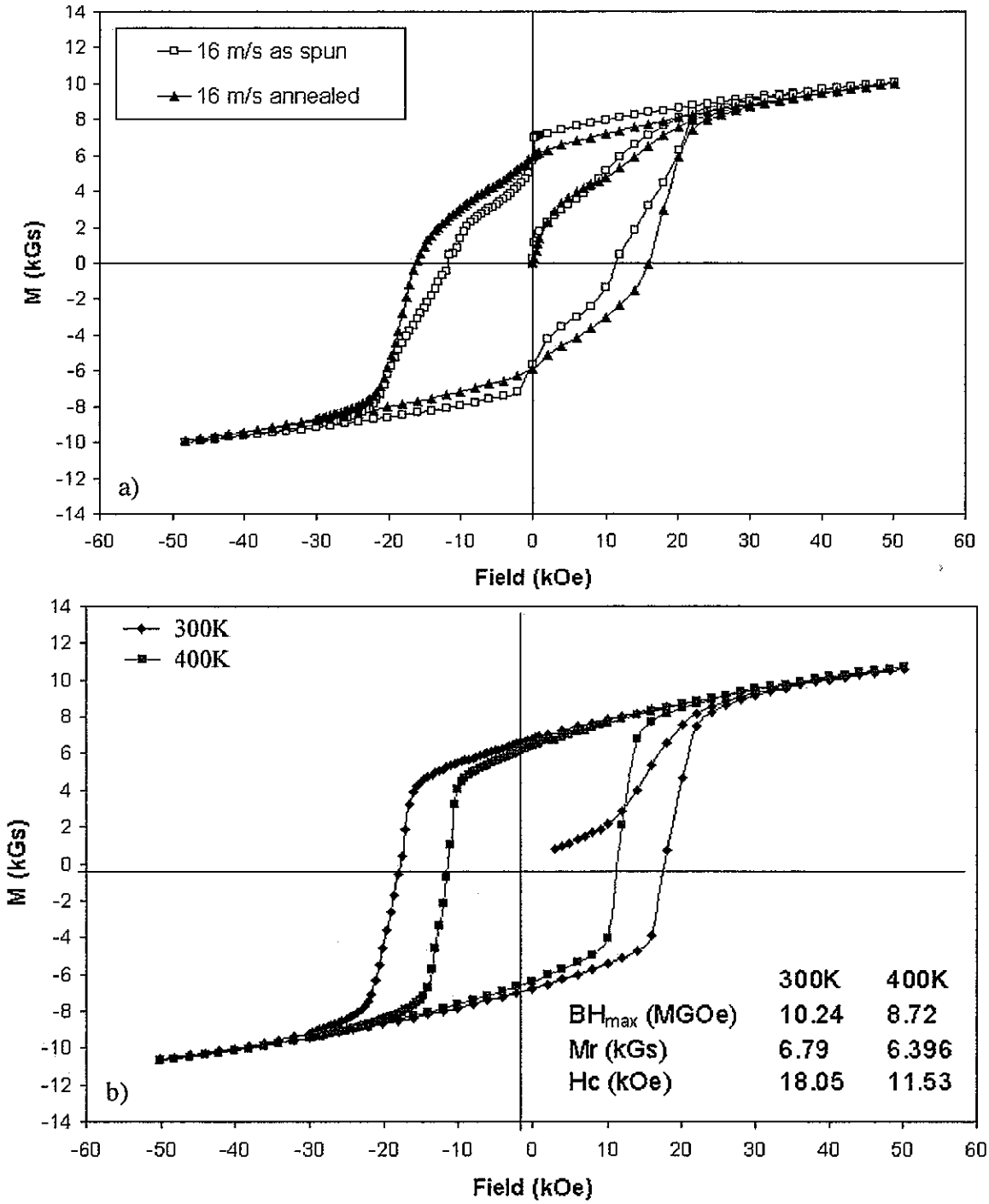

Figure 12: a) Hystresis loop for 16m/s as-spun and annealed. b) Hystresis loop for 22m/s annealed ribbon tested at 300 and 400K.

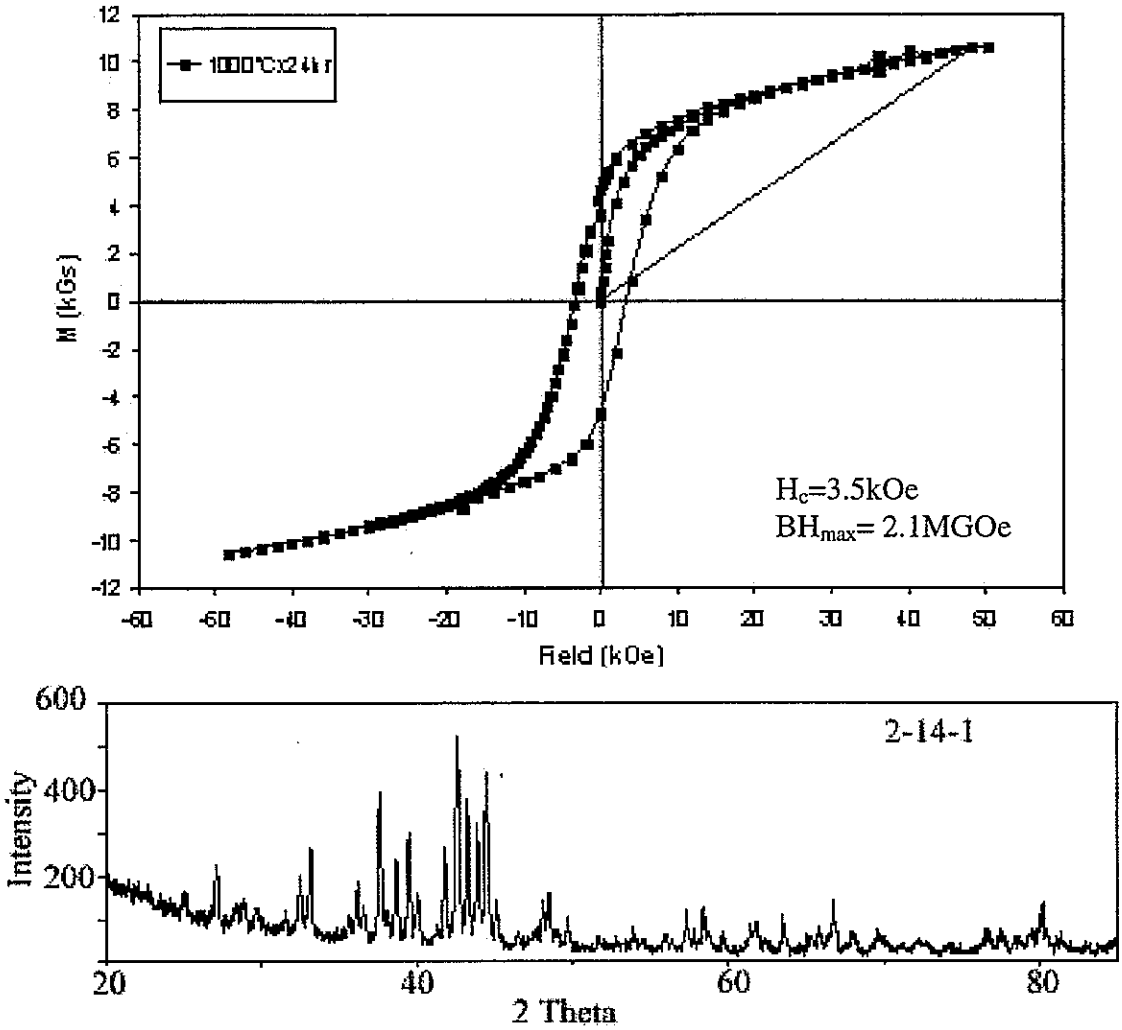

Figure 13: Hystresis loop for MRE powder annealed for 24hrs at 1000°C and corresponding XRD trace.

CONCLUSIONS

For the composition of $MRE_2Fe_{14}B$ presented in this study, MRE_2Fe_{17} forms as the primary phase in the as-atomized state. Annealing treatments on the HPGA powder will transform the MRE_2Fe_{17} to $MRE_2Fe_{14}B$, improving the magnetic properties of $MRE_2Fe_{14}B$. For melt-spun ribbon at 10m/s, $MRE_2Fe_{14}B$ is seen on the wheel and free side of the ribbon with an interface midway though the thickness separating different growth morphologies. The annealing treatment used on the 10m/s and 16m/s ribbon did not significantly improve their magnetic properties. The same unknown mechanism limiting expected grain growth in

the HPGA powders when annealed for along time at a high temperature may also be suppressing the phase and morphology transformation in the ribbon samples. Also increasing wheel speeds creates an $MRE_2Fe_{14}B$ microstructure favorable to exhibiting hard magnetic properties. Proper annealing treatments improve magnetic properties of melt-spun $MRE_2Fe_{14}B$ as seen in 22m/s sample.

ACKNOWLEDGEMENT

This work was supported by USDOE-EE-FCVT Program, Freedom Car Initiative, through Ames Laboratory contract no. W-7405-Eng-82.

REFERENCES

1. R. Fischer and H. Kronmüller. "The role of grain boundaries in nanoscaled high-performance permanent magnets". *Journal of Magnetism and Magnetic Materials.* 184 (1998) 166-172

2. D. Goll, H. Kronmüller. "High performance permanent magnets". *Naturwissenschaften.* 87 (2000) 423-438l.

3. ISURF 02935, McCallum, R.W., Xu, Youwen, Kramer, M.J., Anderson, I.E., and Dennis, K.W. "Permanent Magnet Alloy with Improved High Temperature Performance"

4. G.C. Hadjipanayis. "Nanophase hard magnets". *Journal of Magnetism and Magnetic Materials.* 200 (1999) 373-391.

5. R. Hermann, O. Filip. "Influence of melt convection on the microstructure of levitated and undercooled Nd-Fe-B alloys". *Journal of Magnetism and Magnetic Materials.* 263 (2003) 15-20.

6. Y.L. Tang, M.J. Kramer, K.W. Dennis, R.W. McCallum, and L.H. Lewis. "On the control of microstructure in rapidly solidified Nd-Fe-B alloys through melt treatment". *Journal of Magnetism and Magnetic Materials.* 267 (2003) 307-315.

7. J. Xiao and J Otaigbe. "Polymer bonded magnets III. Effect of surface modification and particle size on the improved oxidation and corrosion resistance of magnetic rare earth fillers". *Journal of Alloys and Compounds.* 309 (2000) 100-106

8. N. Hamada, C. Mishima, H. Mitarai, and Y. Honkura. "Development of Nd-Fe-B Anisotropic Bonded Magnet with 27 MGOe".

9. ASM International, *Handbook of Ternary Phase Diagrams*, 1995

10. W. Tang, K.W. Dennis, Y. Q. Wu, M.J. Kramer, I.E. Anderson, and R.W. McCallum. "Studies of new YDy-based $R_2Fe_{14}B$ magnets for high temperature performance (R=Y+Dy+Nd)". *IEEE Transactions on Magnetics.* 40 (4), July 2004.

11. M. Seeger, D. Köhler, H. Kronmüller. "Magnetic and microstructural investigations of melt-spun Fe(NdPr)B". *Journal of Magnetism and Magnetic Materials.* 130 (1994) 165-172.

12. I.E. Anderson and B.B. Bath. "Rapid Solidification of Copper-Based Alloys". *Rapidly Solidified Crystalline Alloys.* Compiled by S.K. Das, B.H. Kear, and C.M. Adam, TMS-AIME, Morristown, NJ, May 1-3, 1985, 219-244.

CHAPTER 3: MICROSTRUCTURE AND MAGNETIC PROPERTIES OF GAS ATOMIZED MIXED RARE EARTH IRON BORON

A paper published in *Advances in Powder Metallurgy & Particulate Materials - 2005*[1]

N.L. Buelow[2], I.E. Anderson[3*], R.W. McCallum[4], M.J. Kramer[5], W. Tang[6], and K.W. Dennis[7]

ABSTRACT

Novel mixed rare earth iron boron ($MRE_2Fe_{14}B$) permanent magnet alloys have the desirable ability to be gas atomized into powders with competitive magnetic properties. Current stoichiometric $Nd_2Fe_{14}B$ permanent magnets (having high flux density) are typically melt-spun to achieve the cooling rates necessary to create the amorphous or nanocrystalline phases desired for permanent magnets. Gas atomized powders have a spherical shape which is preferred for polymer bonded magnets as compared to the flake geometry of melt-spun powder. The most beneficial magnetic property of $MRE_2Fe_{14}B$ is the stabilization of coercivity, remenance and therefore energy product (BH_{max}) over a range of elevated operating temperatures (>150°C). With the use of glass formers the microstructure can be modified creating a fine dendritic structure, microcrystalline structure, and amorphous structure depending on particle size. Similar to flake particulate, as-atomized powders often need annealing treatments to modify the microstructure for optimal magnetic properties.

---

[1] Reprinted with permission from ADVANCES IN POWDER METALLURGY & PARTICULATE MATERIALS 2005, Metal Powder Industries Federation, 105 College Road East, Princeton, New Jersey 08540
[2] Graduate student Materials Science and Engineering and primary author
[3] Adjunct Professor of Materials Science and Engineering and Ames Lab-USDOE Senior Metallurgist
[*] Author for correspondence
[4] Adjunct Professor of Materials Science and Engineering and Ames Lab-USDOE Senior Materials Scientist
[5] Adjunct Professor of Materials Science and Engineering and Ames Lab-USDOE Scientist II
[6] Ames Lab-USDOE Post Doctoral Fellow
[7] Ames Lab-USDOE Assistant Metallurgist

INTRODUCTION

There is an increasing need for permanent magnets (PMs) that perform better and last longer in hostile environments. The automobile industry is showing great interest in developing commercially available hybrid/electric automobiles. This is driving the development of electric motors which in turn is calling for better and cheaper PM materials. Another stipulation is that these PMs must be easily integrated into a high output production line, dictating that near-net shape and preferably net shape manufacturing be possible.

Magnetic strength per unit volume of PM, or maximum energy product (BH_{max}), is one factor that dictates how an electric motor will be designed and will perform. High strength PMs are needed so that an automobile with an electric motor performs similarly to one powered by an internal combustion engine [1]. Along with the high magnetic strength, the volume and weight of the PM must be minimized. PMs with a high BH_{max} are well suited for motor applications. The PM material with the highest BH_{max} is currently $Nd_2Fe_{14}B$ [2]. However, the excellent magnetic properties of $Nd_2Fe_{14}B$ do not remain as the temperature is increased to operating temperatures approaching 150°C that are expected for hybrid/electric vehicles.

As the average operating temperatures increase, the intrinsic weakness in $Nd_2Fe_{14}B$ becomes apparent. The two magnetic properties that affect BH_{max}, remanence and coercivity, are highly temperature dependent [1]. As the operating temperature is increased, the BH_{max} of $Nd_2Fe_{14}B$ will decrease. Figure 1 shows the dependence of remanence and coercivity to temperature.

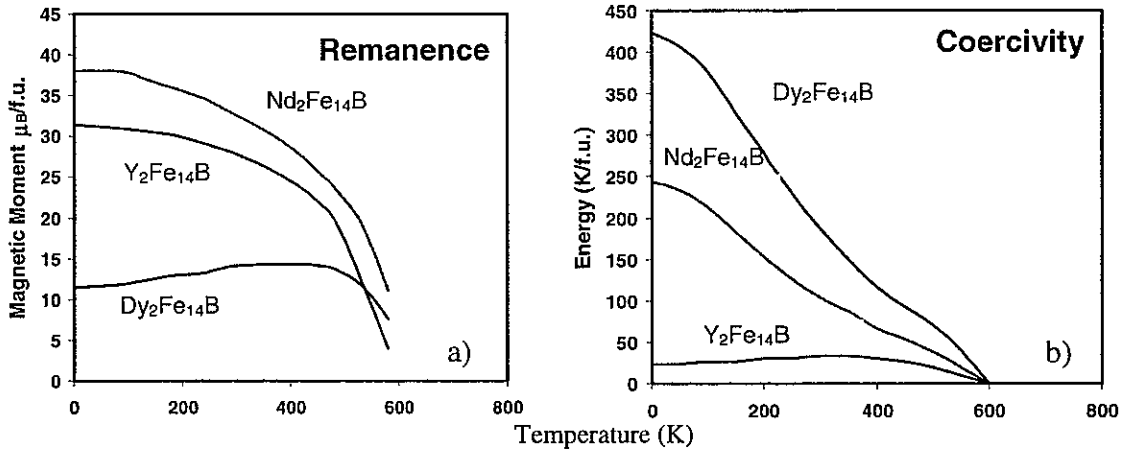

Figure 1: Comparison of magnetic properties of $Nd_2Fe_{14}B$ to two other 2-14-1 phases. a) Shows temperature dependence of remanence and b) shows the temperature dependence of the coercivity.

Stabilizing the temperature dependent magnetic properties without significant loss of BH_{max} is one of the alloy design goals for novel mixed rare earth iron boron ($MRE_2Fe_{14}B$) PM materials. This has been accomplished by alloying $Nd_2Fe_{14}B$, $Dy_2Fe_{14}B$, and $Y_2Fe_{14}B$ in hopes of creating a material that will posses a symbiosis of the temperature dependent magnetic properties [3]. This approach has proven successful in diminishing the loss of BH_{max} up to the Curie temperature. The stable temperature dependent properties allow $MRE_2Fe_{14}B$ to have a higher value of BH_{max} at operating temperatures above 125°C as compared to commercial $Nd_2Fe_{14}B$ (see Figure 2).

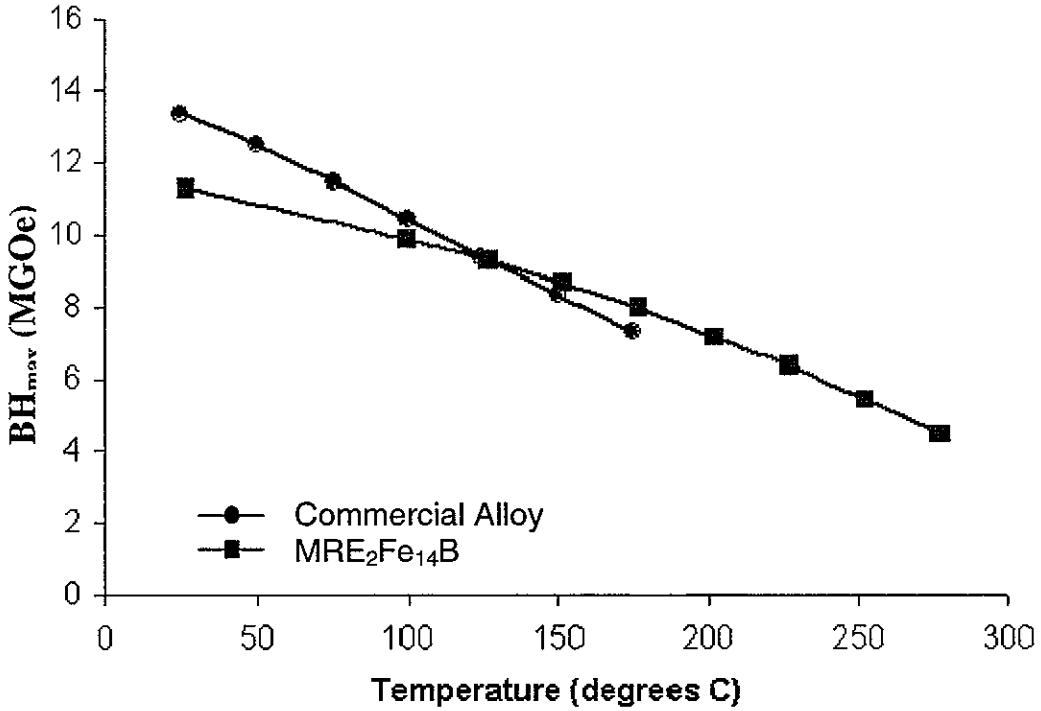

Figure 2: Temperature stability of BH_{max} of $MRE_2Fe_{14}B$ vs. a commercially available $Nd_2Fe_{14}B$.

The base alloy for the mixed rare earth family is $YDyFe_{14}B$. The base alloy is designed around the fundamental goal of creating a PM that will have increased stability of the temperature dependent magnetic properties, leading to a PM powder that will have minimal decrease in magnetic properties at operating temperature. Substituting yttrium and dysprosium for the neodymium in $Nd_2Fe_{14}B$ was done because the $Dy_2Fe_{14}B$ and $Y_2Fe_{14}B$ have more stable remanence and coercivity values while undergoing a temperature increase, respectively.

Another goal is to make $MRE_2Fe_{14}B$ into a spherical powder instead of the flake powder available in commercial $Nd_2Fe_{14}B$. These current $Nd_2Fe_{14}B$ powders are made via melt spinning which offers excellent control of the processing parameters that determine the microstructure [4]. Free-jet melt-spinning rapidly quenches the molten PM material on a rotating copper wheel, creating a ribbon with an overquenched (amorphous) microstructure. Annealing the as-spun crystallizes the desired phase and microcrystalline microstructure. The ribbon is then crushed into a fine powder, in an inert atmosphere, that can used to make

sintered fully dense isotropic and anisotropic PMs, or more typically, isotropic polymer bonded permanent magnets (PBMs)

PBMs are not as strong magnetically as sintered fully dense PMs, but their advantage, particularly for mass production, lies in their ability to be net shape processed. Sintered PMs are hard and brittle which requires cutting and grinding to shape the magnet. The difference in BH_{max} between polymer bonded and sintered fully dense PMs is accounted for in the relationship shown in Equation 1 [5].

$$(BH_{max})^{bond} = f^2(BH_{max}) \quad (1)$$

In equation 1, the BH_{max} is proportional to the fill factor (f), where (f) is the volume fraction of magnet powder in the bonded permanent magnet [5]. Note that this relationship is a comparison between an isotropic sintered fully dense magnet and an isotropic PBM.

Melt spinning is the proven method to create high performance PM powder for PBMs. However, the flake-type geometry of the crushed ribbon is a major limiting factor in forming PBMs. The flake geometry limits the loading fraction possible without a dramatic increase in relative viscosity. However, a spherical geometry is well suited for injection molding, having a lower relative viscosity as compared to flake particles, Figure 3 [6]. The lower relative viscosity of spherical powders blended with a polymer binder means higher loading factions of PM powder, which increases BH_{max}, and can be accomplished without a significant increase to injection pressure [6].

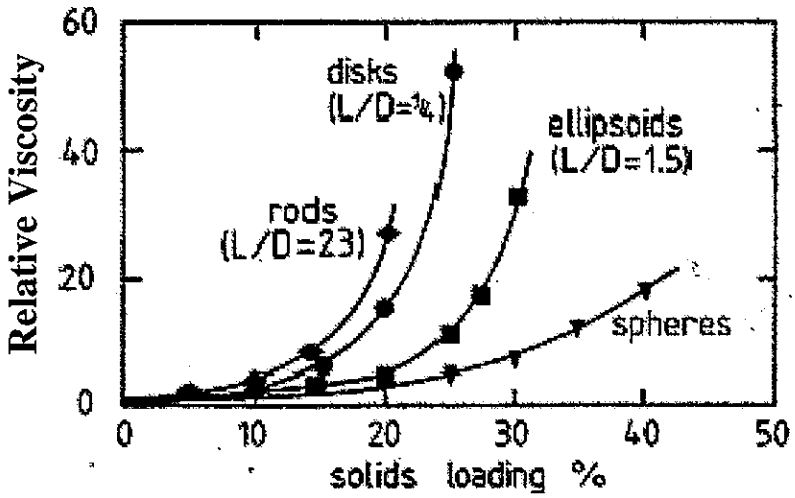

Figure 3: Relative viscosity of a polymer blending with metal powders with different geometries [6]. A disk shape powder can be considered similar to that of the flake powders.

The difficulty in using high-pressure gas-atomization (HPGA) as compared to melt spinning is related to factors that control the powder microstructure. The conductive cooling associated with initial stage of melt spinning, from direct quenching on the copper wheel, can achieve higher cooling rates than those seen in HPGA, although departure from the wheel during the final stage permits only convective cooling, especially for the free side (non-contact side) of the ribbon. Cooling rate in HPGA is controlled only by convective cooling through the atomizing gas. The difference in nucleation between the two processes must also be considered. Break-up of the melt stream at the nozzle introduces the beneficial mote isolation effect. Smaller atomized particles have a reduced number of active nucleation sites, increasing the undercooling [7]. Nucleation in melt spinning is heterogeneous as the microstructure will nucleate on the wheel surface and grow toward the free surface. Powders made via HPGA are solidified in flight without a contacting a surface, reducing the number of highly active heterogeneous nucleation sites and increasing the amount of undercooling. The reduction in nucleation sites requires HPGA powders to reach higher undercoolings to initiate nucleation of the $MRE_2Fe_{14}B$ phase [8]. In spite of these differences, melt spinning can still be a useful tool for alloy design for gas-atomized PM alloys, especially if the initial quench rate is reduced by the used of low wheel speeds.

EXPERIMENTAL PROCEDURE

Alloy design iterations were completed using free-jet melt-spinning. Samples were induction melted in a quartz crucible and then quenched on the rotating chill block in 1/3 atm ultra high purity (UHP) helium. As alloy design work continued on the melt spun alloys, $MRE_2Fe_{14}B$ alloy designs that had significant increments in magnetic properties at low wheel speeds where prepared by HPGA.

Atomization was completed using UHP helium as the atomizing gas to get the maximum breakup of the melt stream due to helium's high velocity and the maximum convective cooling from helium's high heat transfer coefficient, compared to other inert atomizing gases. The atomized powder was then collected and separated using ASTM standard sieves.

After sieving <53μm, the powder samples were prepared for XRD and SEM observation. Larger particles were analyzed first, working down to the smallest particles. The powders were placed in small epoxy mounts. Four of the small epoxy mounts where held in phenolic resin. The phenolic mount used a copper filled phenolic as the face to increase the conductivity. Mounts were then polished using oil as the lubricant instead of water. Water will hydrolyze the rare earths in the $MRE_2Fe_{14}B$ particles. The mounts were polished down to 1μm and then etched with an acid etch. Nitric, acetic, phosphoric, and lactic acids were mixed and diluted with methanol to a 1:3 ratio (combined acid volume to methanol volume). Particles showing promising phase selection and microstructure were tested for magnetic properties.

After testing the powders in the as-atomized state, an annealing treatment was preformed. This heat treatment was done to promote growth of the $MRE_2Fe_{14}B$ phase to enhance the magnetic properties. To do this heat treatment, the powder samples were wrapped in a tantalum pouch and placed in a quartz capsule in a 1/3 atm of UHP helium. The powders were annealed at 750°C for 15 minutes. After annealing the powders, XRD, SEM and SQUID magnetometer measurements were done to determine phase selection, morphology, and magnetic properties, respectively.

RESULTS

Particles that contained the maximum amount of $MRE_2Fe_{14}B$ phase, along with secondary phases, had the best chance of having a high $BH_{max.}$ XRD results, Figure 4, revealed that no as-atomized particles of the $YDyFe_{14}B$ composition had a dominant amount of $MRE_2Fe_{14}B$ phase in their microstructures, although the coarsest (+45μm dia.) powder trace does show the clearest peaks for $MRE_2Fe_{14}B$ phase along with the majority MRE_2Fe_{17} phase. This result focused the search on the smaller particles which will experience the highest cooling rate and will therefore have the greatest probability of containing the $MRE_2Fe_{14}B$ in some small proportion, at least after annealing.

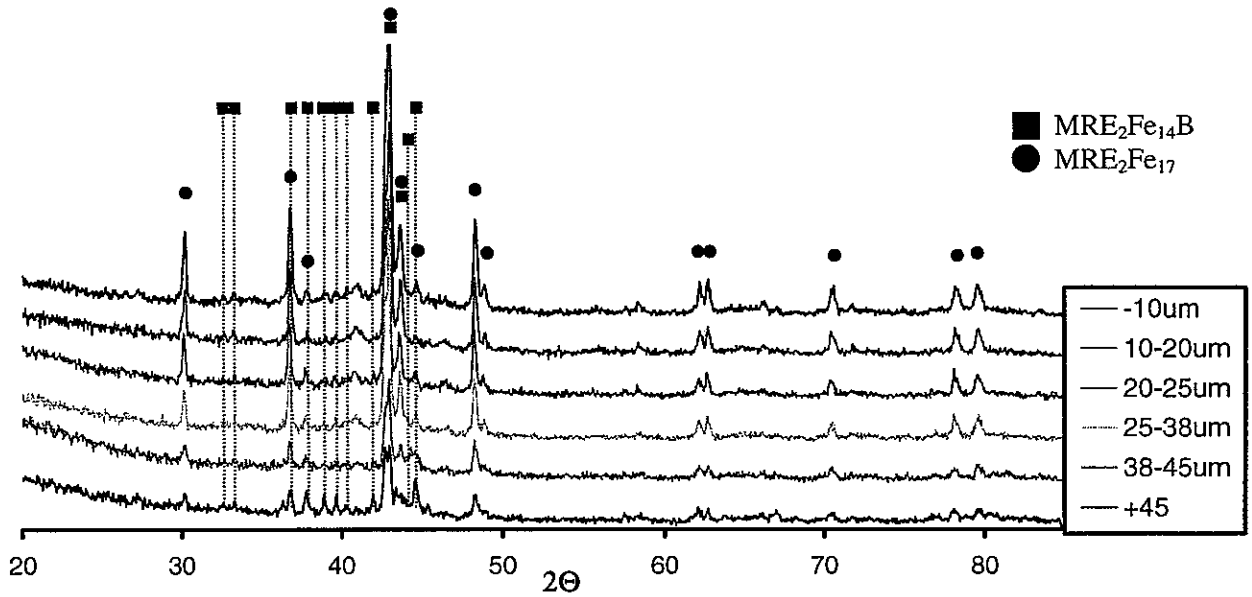

Figure 4: X-ray traces for the different particle sizes of HPGA $YDyFe_{14}B$

The microstructure of $YDyFe_{14}B$ is considered the baseline for all improvements to the MRE family of PMs. Microstructures seen in Figure 5 are for as-atomized spherical powders of $YDyFe_{14}B$ and appear dendritic in nature. This dendritic microstructure is seen through the full range of particle sizes investigated. XRD reveals that the primary phase that makes up the microstructures is MRE_2Fe_{17}, but there is a possibility that $MRE_2Fe_{14}B$ exists interdendritically as a second phase as-detected marginally in the XRD results.

Unfortunately, the interdendritic phase regions were too narrow to permit useful WDS (electron probe) or EDS measurements.

In particles of less than 10μm, high enough cooling rates had been reached to form an amorphous shell. Inside that shell, the structures were still dendritic. This was encouraging as cooling rates similar to those seen in melt spinning could be reached in the small particle range. It should be noted that previous report of melt-spun ribbon microstructures in cross-section [3] did reveal an amorphous region on the wheel side of ribbon samples that were melt spun at only 10m/s.

Improvements in alloy design were accomplished through the addition of neodymium, zirconium, and cobalt. Neodymium was added to boost the remanence of $MRE_2Fe_{14}B$ [9], and cobalt was used to increase the Curie temperature and add to the temperature stability of $MRE_2Fe_{14}B$ [10]. These additions did not attribute to any significant change in microstructure. The zirconium was then added to refine the microstructure. Zirconium is known to increase the number of heterogeneous nucleation sites, thus decreasing the average crystallite size leading to a finer microstructure [11].

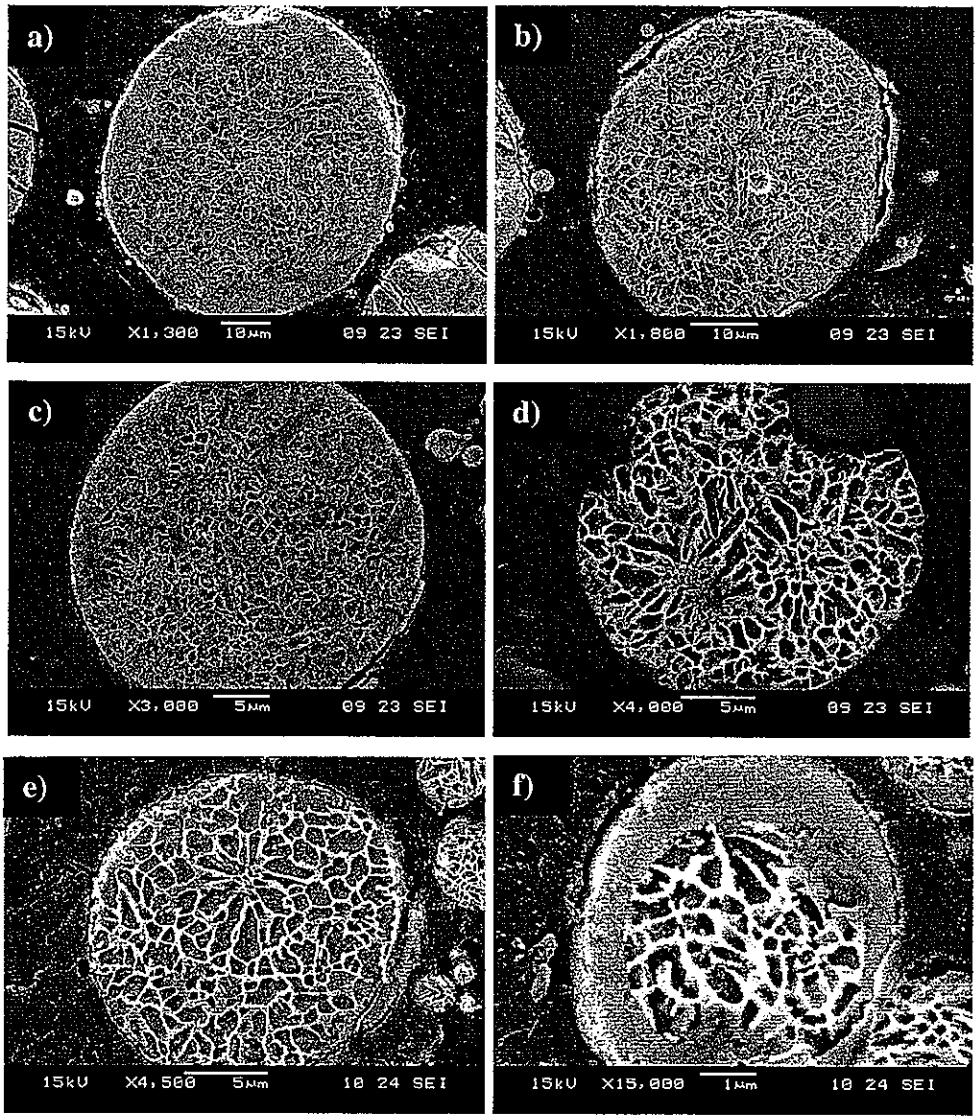

Figure 5: Microstructures for different particle sizes of $YDyFe_{14}B$ a) +45µm particles b) 38-45µm particles c) 25-38µm particles d) 20-25µm particles e) 10-20µm particles f) -10µm particles

The X-ray traces for the as-atomized powders of $MRE_2Fe_{14}B$ composition $[Nd_{0.45}(YDy)_{0.25}]_{1.8}Zr_{0.4}Co_{1.5}Fe_{12.5}B$ are shown in Figure 6. The larger particles, 10-53µm, show MRE_2Fe_{17} as the primary solidification product. At a 5-10µm particle size, the $MRE_2Fe_{14}B$ phase shows up as either the primary or a large vol% of secondary solidification product. There is still a strong peak for the MRE_2Fe_{17} phase accompanying the $MRE_2Fe_{14}B$ phase. The peaks for the 5-10µm, and especially, the -5µm particles also start to broaden, indicating increasing amounts of nanocrystalline and amorphous features in the solidified

microstructure. Below 5μm a significant portion of the powder sampled was amorphous, as evidenced by the baseline "hump" that rises below the 42° 2Θ region.

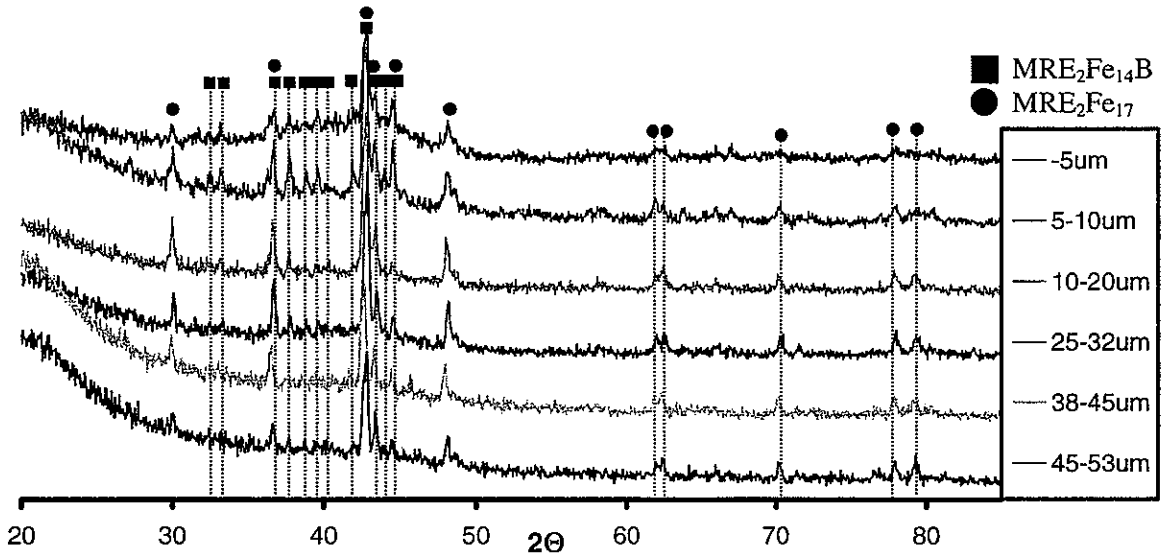

Figure 6: X-ray traces for several different HPGA powder size distributions for the $MRE_2Fe_{14}B$+Zr alloy composition.

Microstructures caused by the 0.03wt% addition of zirconium are seen in Figure 7a-h. The dendritic structure is consistent down to particle sizes of 10μm. New microstructures are seen in the particles <10μm. As seen in Figure 7g, the microstructure is no longer dendritic but appears to be microcrystalline, one step closer to the desired structure for optimum magnetic properties.

Some of the particles in the 5-10μm range had amorphous shells around their circumference (see Figure 7g). The amorphous shells are not necessary for forming the microcrystalline microstructures, as this structure can solidify without the accompanying amorphous shell (see Figure 7h). The amorphous shell only occurred on ~10% of the particles in the 5-10μm range. This feature is again encouraging as the solidification front appeared to be moving very fast, creating an amorphous phase and other fine features. This relates to a high undercooling, increasing the chance of forming the $MRE_2Fe_{14}B$ phase. In the <5μm particles the solidification front moved fast enough to make the particle matrix amorphous with small nucleation sites mixed in.

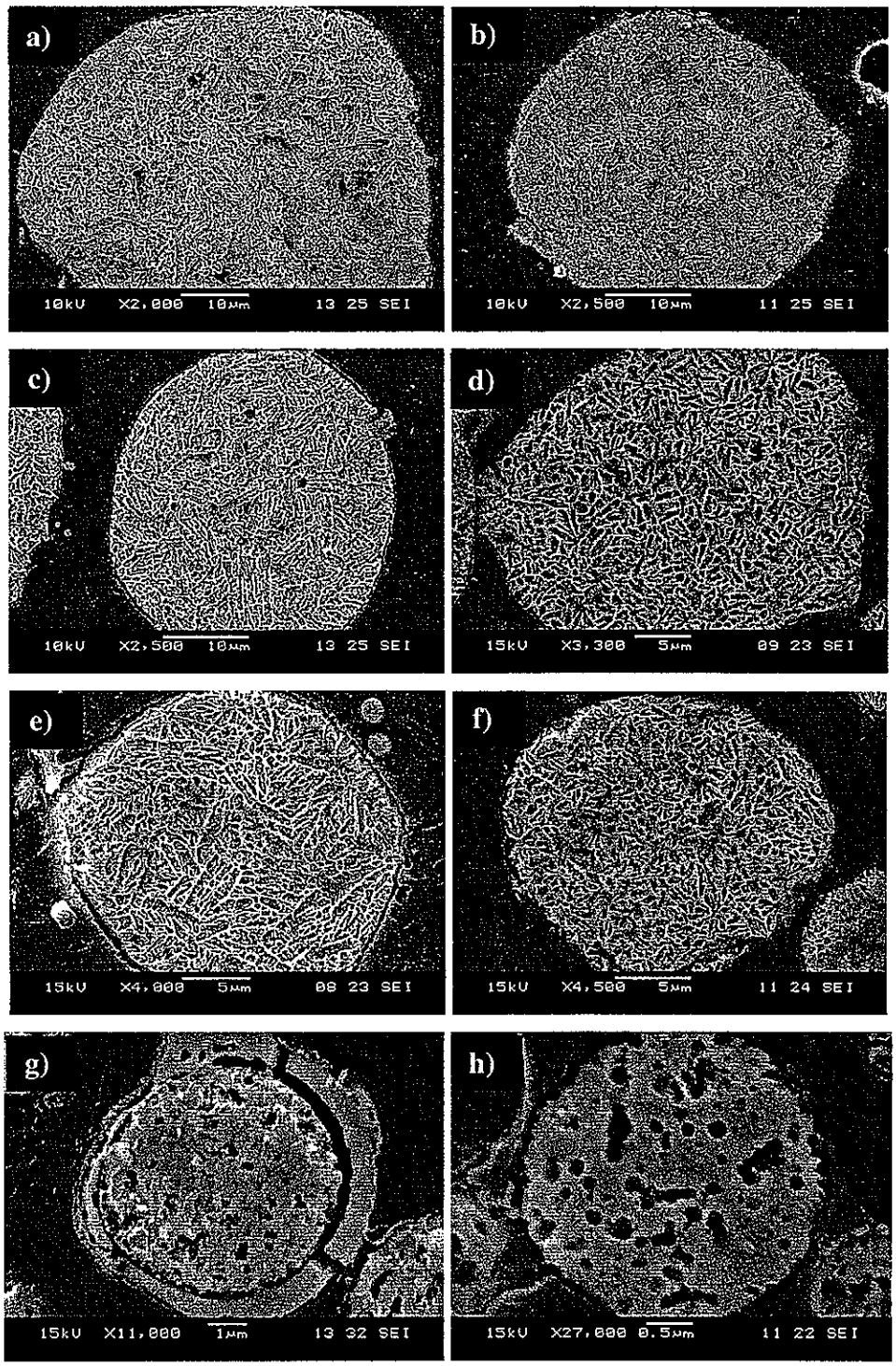

Figure 7: Microstructure of the different particle sizes. a) 45-53µm particles b) 38-45µm particles c) 32-38µm particles d)25-32µm particles e) 20-25µm particles f)10-20µm particles g)5-10µm particles h) -5µm particles

DISCUSSION

For $MRE_2Fe_{14}B$ to have the most effective magnetic properties, the microstructure must be carefully controlled. It has been know for years that cooling rate affects the phase composition and the microstructure. Figure 8 shows a schematic time-temperature-transformation (TTT) diagram for the $MRE_2Fe_{14}B$ system. This TTT diagram could be considered typical for the $YDyFe_{14}B$ system and the addition of the 0.03wt% of zirconium will modify the TTT curve shown. Three solidification paths are shown as examples in Figure 8. The first cooling rate will be the fastest and will form an amorphous particle avoiding the nose of both curves. This overquenched state is desirable as it will be easy to anneal the material to the proper nanocrystalline microstructure. The next slowest cooling rate will create a particle that has cooled fast enough to avoid forming MRE_2Fe_{17} and will form $MRE_2Fe_{14}B$ only. The phase composition may be correct but the concern will be with the size of the microstructure. Finally, the last cooling rate shown, the slowest, cuts though the MRE_2Fe_{17} phase which means the microstructure will consist of MRE_2Fe_{17} as the primary phase and $MRE_2Fe_{14}B$ as the secondary phase.

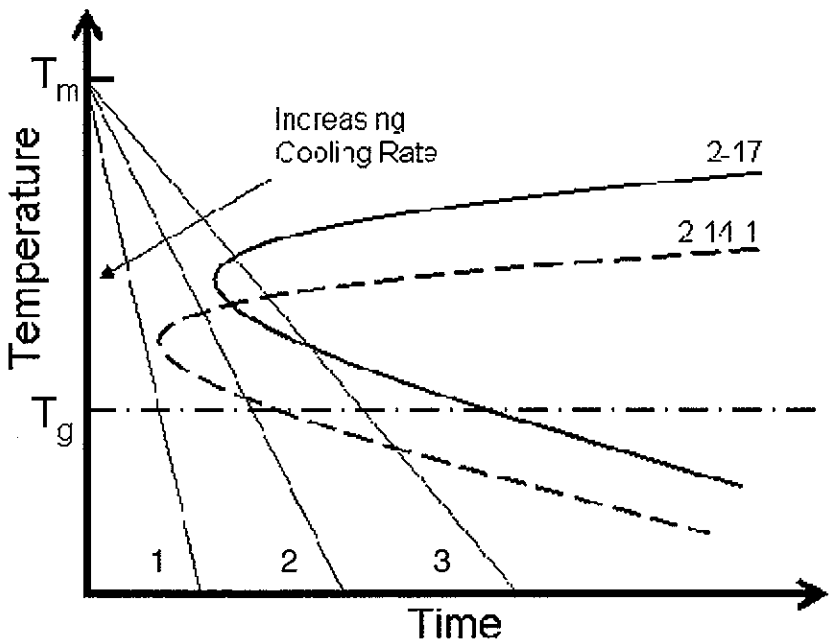

Figure 8: Schematic TTT curves explaining the formation of the phases seen in the $MRE_2Fe_{14}B$ microstructures. Three cooling rates are shown.

Zirconium is effective in reducing the cooling rate needed to arrive at the desired microstructure with the correct phase composition. In effect, the 0.03wt% zirconium addition shifts the noses of the MRE_2Fe_{17} and $MRE_2Fe_{14}B$ curves shown in Figure 8 to longer times. The possibility of creating the $MRE_2Fe_{14}B$ phase, with a fine structure, increases as the requirement for extreme cooling rates is lessened. This will lead to more $MRE_2Fe_{14}B$ overall. The size of the particles that contain $MRE_2Fe_{14}B$ will also increase due to the zirconium.

The difference in the microstructure of the $MRE_2Fe_{14}B$ alloys with and without the zirconium can be seen by comparing the secondary dendrite arm spacing (SDAS) of the two powders (Figure 9). Visually comparing the two particles in Figure 9, the effect of the 0.03wt% zirconium addition is apparent. The two particles are of similar size and the secondary phase in the particle with zirconium is much denser than the particle not containing zirconium. The change in the fraction of the primary phase and interdendritic phase was dramatic. The $YDyFe_{14}B$ had the primary phase as 61% of the surface area as measured by an image analysis method from a series of similar SEM micrographs. With the zirconium addition, the primary phase only occupied 31% of the analyzed surface. On average, the upper range of the SDAS for the zirconium added $MRE_2Fe_{14}B$ was below that of the average SDAS for the $MRE_2Fe_{14}B$ without the zirconium addition. The reduction in SDAS was not uniform for all particle sizes. There was no trend for increasing or decreasing effectiveness due to the addition of zirconium based on particle size.

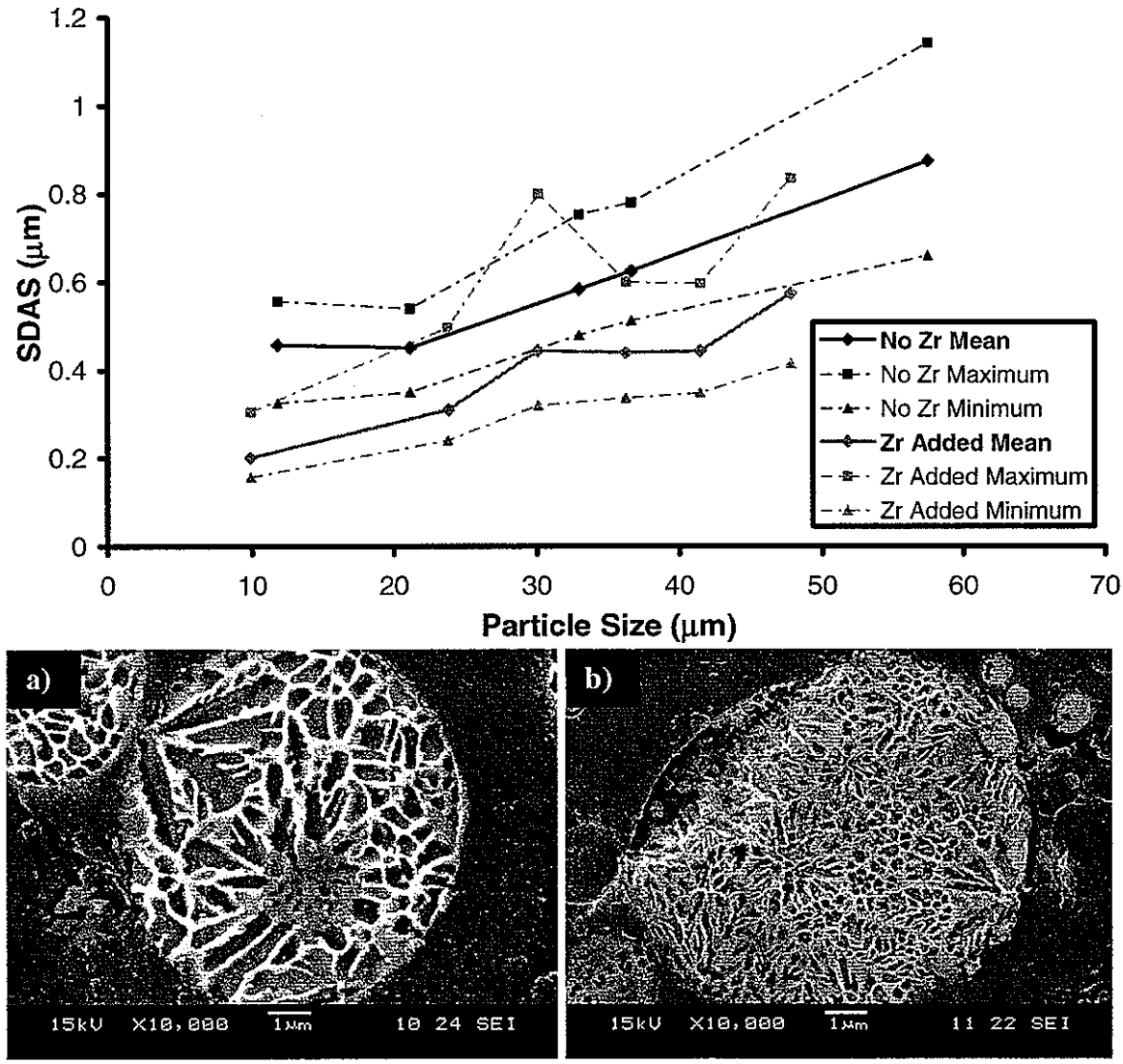

Figure 9: Comparison of the SDAS of $MRE_2Fe_{14}B$ with and without the addition of zirconium. Microstructure images are given for comparison of a) the MRE without 0.03wt% zirconium addition and b) with the zirconium addition.

Zirconium appears to be able to reduce the SDAS by increasing the frequency of heterogeneous nucleation events. When looking at the smaller particles for both alloys, the nucleation sites on one plane can be determined. In the case of the $YDyFe_{14}B$ the number of nucleation sites for that plane of polish can be determined by counting the number of sites that dendrites have grown from. For the MRE alloy with zirconium the nucleation sites show up as black dots. These sites did not grow into large dendrites as the particle had solidified before long-range growth could take place. Using the afore mentioned method to determine

nucleation frequency, the zirconium addition seemed to successfully increase the number of nucleation sites by about ten times. Figure 10 shows particles that were used to determine the number of nucleation points on a single plane for both alloys.

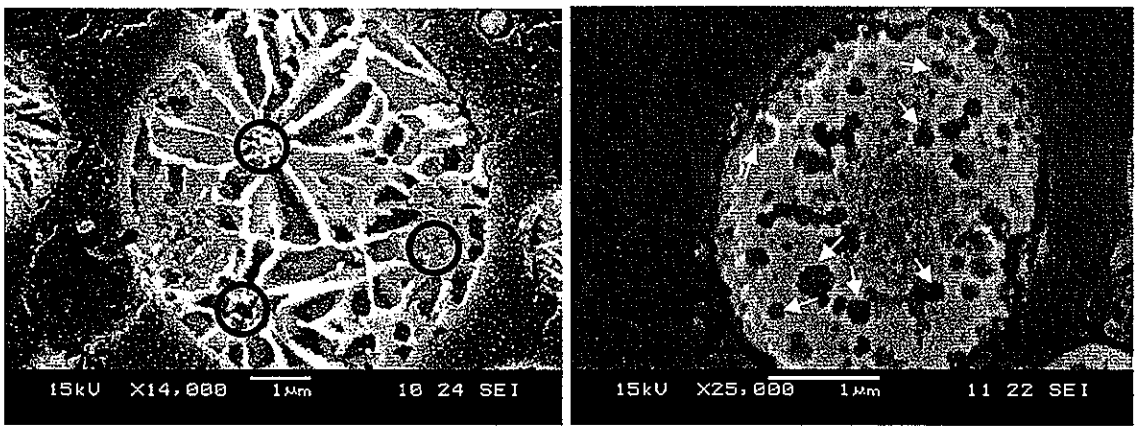

Figure 10: The a) $YDyFe_{14}B$ has circles drawn around nucleation events. The black dots on the surface of b) represent the nucleation events for the alloy with 0.03wt% zirconium added.

The 0.03wt% zirconium addition was effective at reducing the SDAS and also in changing the primary solidification product to $MRE_2Fe_{14}B$ instead of MRE_2Fe_{17}. This was verified by the microprobe data shown in Table 1. Zirconium appears to be effective in reducing the cooling rates needed to solidify $MRE_2Fe_{14}B$, allowing a greater volume fraction of the $MRE_2Fe_{14}B$ phase to be present in the particles. Due to the small size of the phases scanned, the activated volume may contain data from phases around and below the phase of interest.

Table 1: Microprobe data for the two different alloys.

	$YDyFe_{14}B$			$MRE_{1.8}Zr_{0.4}Co_{1.5}Fe_{12.5}B$		
Phase	MRE (wt%)	Fe (wt%)	B (wt%)	MRE+Zr (wt%)	Fe+Co (wt%)	B (wt%)
Primary	20.70%	78.36%	0.35%	21.64%	70.90%	1.15%
Interdendritic	22.41%	75.41%	0.68%	21.17%	74.13%	0.3%
MRE_2Fe_{17}	23.04%	86.76%	0.00%	25.38%	87.34%	0.00%
$MRE_2Fe_{14}B$	23.04%	71.45%	1.0%	25.38%	71.88%	1.0%

X-ray data that was presented for a large number of particles sizes is similar, but upon closer inspection of the small size fractions, a difference can be seen. Comparison of XRD results for particles less than 10μm without zirconium to particles between 5-10μm with zirconium is shown in Figure 11. The alloy with the zirconium addition showed more peaks consistent with the $MRE_2Fe_{14}B$ phase as compared to the alloy without zirconium.

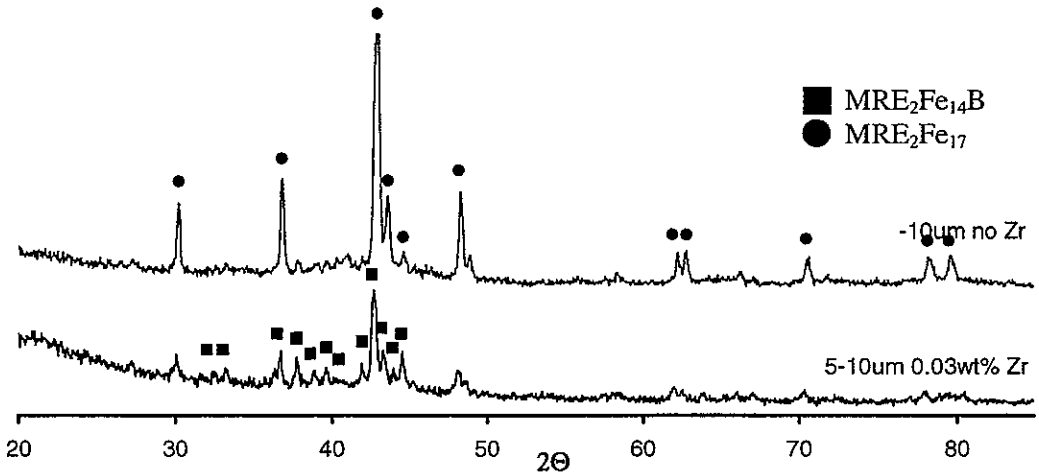

Figure 11: XRD data comparing small particle sizes. The alloy with the zirconium addition shows more characteristic $MRE_2Fe_{14}B$ peaks, which are labeled.

The optimal microstructure for PMs depends on the type of PM that will be produced. For $MRE_2Fe_{14}B$ the desired microstructure is one that is nanocrystalline with the $MRE_2Fe_{14}B$ phase as the primary solidification product. The $MRE_2Fe_{14}B$ phase composition will give the material high remanence and coercivity much like other $RE_2Fe_{14}B$. The remanence is a result of the coupling of the 4f spins of the Rare Earths and the 3d spins of the transition metals [12]. Coercivity is mostly affected by the nanocrystalline microstructure. If the materials are underquenched, large grains will form domain walls and, as a result, reverse domains will easily nucleate which will reduce both the coercivity and the remenance [2].

Due to the geometry of the spherical powders the magnetic poles are forced close together creating a demagnetization field that must be corrected for. Spheres have the highest demagnetizing factor as there is no long axis for the poles to separate along. The demagnetizing field in essence is the field that develops in the PM to resisting the external applied field. Equation 2 is used to correct for the demagnetizing field in order to accurately view the internal field [2].

$$H_{in} = H_{app} - N_d M \quad (2)$$

Where H_{in} is the exact internal field, H_{app} is the applied magnetic field, N_d is the demagnetizing factor (for spheres, N_d is 0.333), and M is the measured magnetization [2]. This correction has been applied to the all the following magnetic loops.

For the $YDyFe_{14}B$ alloy, the primary solidification product was the MRE_2Fe_{17}, which has very low intrinsic coercivity. These large dendritic structures will be able to support domain walls and therefore, reverse domains can nucleate. Even at the small particle sizes, MRE_2Fe_{17} is the primary phase and the solidification structure is dendritic. This combination of phase selection and growth morphology will limit the coercivity of the material limiting the ultimate magnetic strength. Figure 12 shows the magnetic hysteresis loop for the as-atomized particles less than 20μm of $YDyFe_{14}B$.

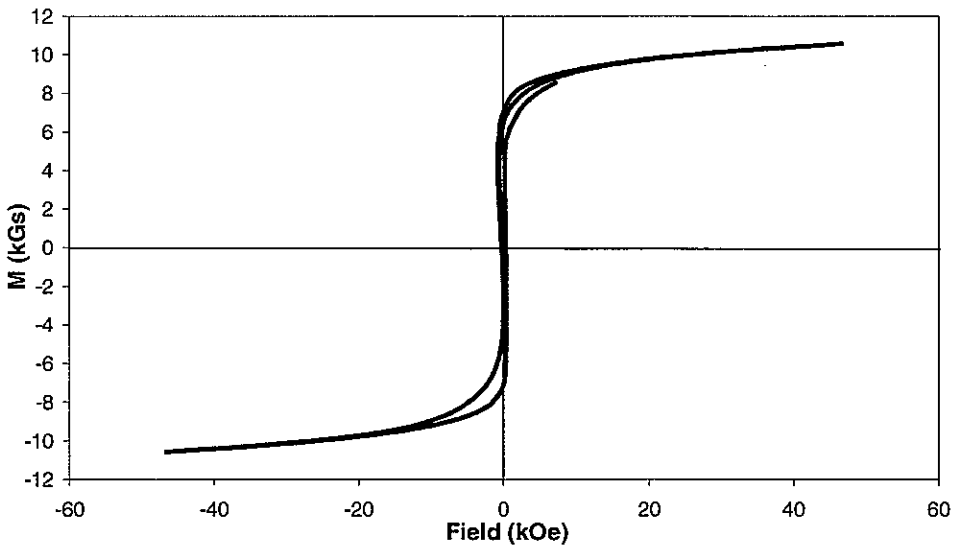

Figure 12: Hystresis loop for $YDyFe_{14}B$, showing the lack of coercivity due to the MRE_2Fe_{17} phase with correction for demagnetizing field due to spherical geometry of powder.

For the $MRE_2Fe_{14}B$ alloy with the 0.03wt% zirconium addition, the as-atomized phase composition was MRE_2Fe_{17} with dendritic growth morphology for the larger particles. The magnetic properties are similar to those seen in the $YDyFe_{14}B$ material, Figure 12. In the range of 5-10μm, more $MRE_2Fe_{14}B$ phase was present in the powder which increased the

magnetic properties. The loop in Figure 13 shows the increases in magnetic properties of the particles in this diameter range. This loop may not have the square shape associated with hard magnetic properties. The loop is improved over the loop for the less than 10μm particles for the $YDyFe_{14}B$. The loop encloses more area in the first and third quadrants as compared to the loop for $YDyFe_{14}B$ in Figure 12. This increase is an effect of the increased volume of $MRE_2Fe_{14}B$ in the particles due to the zirconium addition. An annealing treatment will transform the remaining MRE_2FEe_{17} into $MRE_2Fe_{14}B$ increasing the enclosed area in the second and fourth quadrants. The effect of the annealing treatment is explained in detail below.

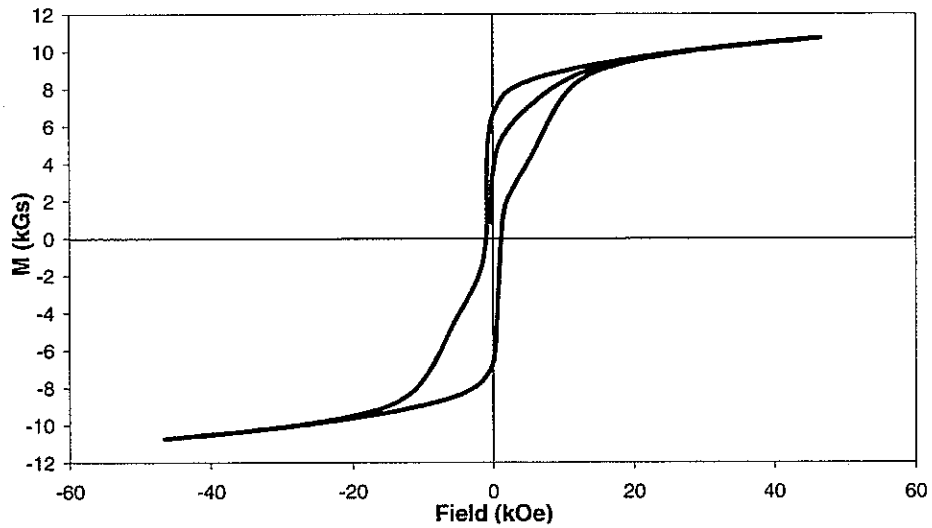

Figure 13: Magnetic properties due to the addition of 0.03wt% zirconium to powder particles in the range of 5-10μm. Demagnetization factor for spherical geometry of powders is considered.

Annealing treatments were also effective in increasing the vol% of the $MRE_2Fe_{14}B$ phase in powders with a zirconium addition. The as-atomized state particles less that 20μm showed signs of $MRE_2Fe_{14}B$ but were primarily MRE_2Fe_{17}. Annealing the MRE powders transformed a major portion of MRE_2Fe_{17} into $MRE_2Fe_{14}B$, as shown in Figure 14. The increased $MRE_2Fe_{14}B$ volume fraction was determined by the increased intensity of the $MRE_2Fe_{14}B$ peaks in the annealed state, although this transformation is not obvious in SEM microstructure comparison, given in Figure 15.

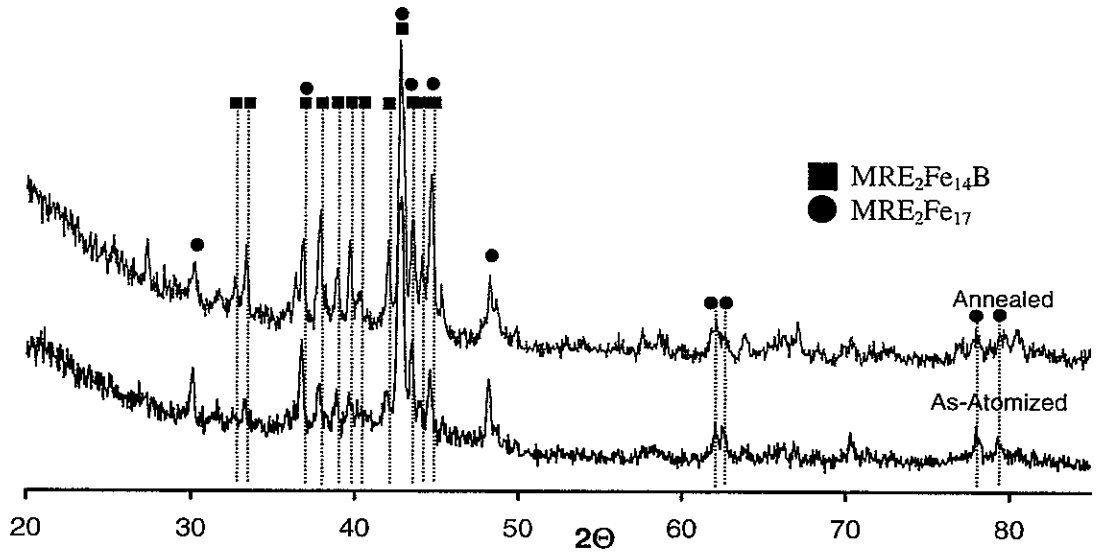

Figure 14: The as-atomized structure shows some vol% $MRE_2Fe_{14}B$, the annealed structure shows an increase in that vol% after a 15 minute anneal at 750°C.

The concern when annealing $MRE_2Fe_{14}B$ powders is promoting too much grain growth while trying to form $MRE_2Fe_{14}B$. Large grains lead to irreversible loss of magnetic properties due to reverse domains. Figure 15 shows the increased coercivity of the annealed powder as compared to the as-atomized powder. The increase in coercivity increases the BH_{max} of the powder.

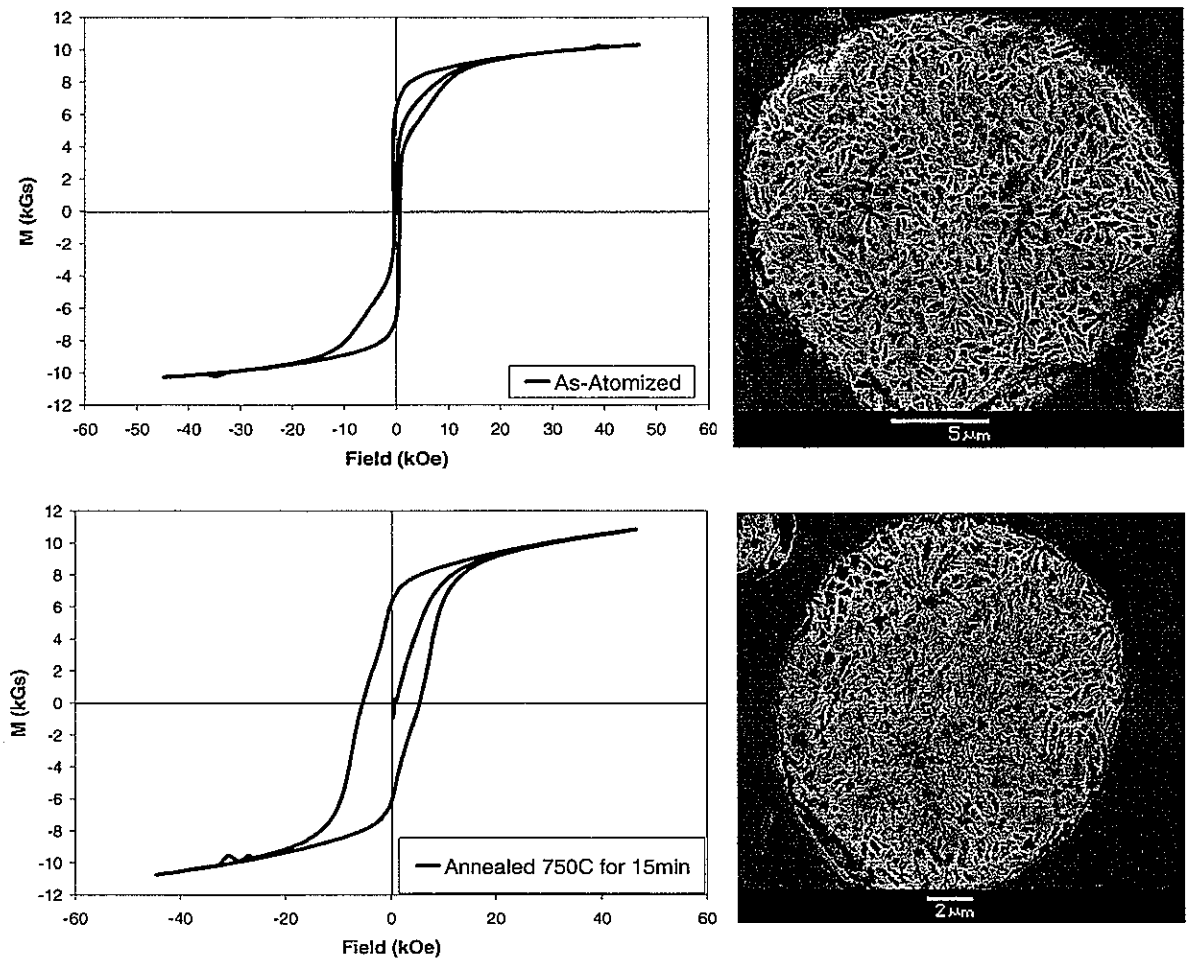

Figure 15: Change in magnetic properties from as-atomized to annealed and the corresponding powder microstructure. Demagnetization due to geometry of particles has been corrected for.

CONCLUSIONS

The process of creating an optimized PM out of HPGA $MRE_2Fe_{14}B$ is well on its way. The base alloy $YDyFe_{14}B$ showed that the material could be atomized to a fine particle size, promoting high cooling rates and undercooling. Although the microstructure and phase constitution was largely dendritic with a primary MRE_2Fe_{17} phase, HPGA of these alloys was considered possible with continued refinement to the alloy design. Alloy design improvements included additions to increase remanence, coercivity, and Curie temperature on the magnetic side, and the use of a glass former, zirconium, to increase the possibility of getting the desired nanocrystalline microstructure. When compared to particles without the

addition of zirconium it was seen visually that the vol% of interdendritic phase had increased compare to particles without zirconium. The zirconium addition was successful in increasing the amount of $MRE_2Fe_{14}B$ in particles <10μm. Also, in the less than 10μm range, amorphous shells and completely amorphous particles are present. Annealing treatments can also be used successfully to grow the microstructure to arrive at the best possible magnetic properties.

ACKNOWLEDGEMENT

This work was supported by USDOE-EE-FCVT Program, Freedom Car Initiative, through Ames Laboratory contract no. W-7405-Eng-82. The authors are also grateful for the EMPA results contributed by Alfred Kracher of Ames Laboratory.

REFERENCES

1. ISURF 02935, R.W. McCallum., Y. Xu, M.J. Kramer, I.E. Anderson, K.W. Dennis. "Permanent Magnet Alloy with Improved High Temperature Performance"

2. D.C. Jiles. *Introduction to Magnetism and Magnetic Materials.* Chapman and Hall. London. 1991.

3. N.L. Buelow, I.E. Anderson, R.W. McCallum, M.J. Kramer, W. Tang, and K. Dennis, "Comparison of Mixed Rare Earth Iron Boride Gas Atomized Powders to Melt Spun Ribbon for Bonded Isotropic Permanent Magnets," in Advances in Powder Metallurgy & Particulate Materials-2004, compiled by W.B. Jones and R.A. Chernenkoff, MPIF, Princeton, NJ, part 10 (2004) pp. 230-244.

4. M. Seeger, D. Köhler, H. Kronmüller. "Magnetic and microstructural investigations of melt-spun Fe(NdPr)B". *Journal of Magnetism a nd Magnetic Materials.* 130 (1994) 165-172.

5. D. Goll., H. Kronmüller. "High performance permanent magnets". *Naturwissenschaften.* 87 (2000) 423-438l.

6. R. M. German, *Powder Injection Molding 1st ed*: Metal Powder Industries Federation, Princeton, New Jersey. 1990.

7. I.E. Anderson and M.P. Kemppainen. "Undercooling Effects in Gas Atomized Powders". *Undercooled Alloy Phases*, E.W. Collings and C.C. Koch Eds., 1986, TMS-AIME, New Orleans, p 269.

8. D.A. Porter, K.E. Easterling. *Phase Transformations in Metals and Alloys 2nd ed.* Chapman and Hall. London. 1992.

9. W. Tang, K.W. Dennis, Y. Q. Wu, M.J. Kramer, I.E. Anderson, and R.W. McCallum. "Studies of new YDy-based $R_2Fe_{14}B$ magnets for high temperature performance (R=Y+Dy+Nd)". *IEEE Transactions on Magnetics.* 40 (4), July 2004.

10. W. Tang, K.W. Dennis, Y.Q. Wu, M. J. Kramer, I. E. Anderson and R. W. McCallum "New YDy-based $R_2(Fe,Co)_{14}B$ Melt-spun Magnets (R=Y+Dy+Nd)", Presented in The 5th Pacific Rim International Conference on Advanced Materials and Processing, November 2-5, 2004. Beijing, China.

11. W. Tang, K.W. Dennis, Y. Q. Wu, M. J. Kramer, I. E. Anderson and R. W. McCallum, "Effect of Zr substitution on microstructure and magnetic properties of new YDy-based $R_2Fe_{14}B$ magnets (R=Y+Dy+Nd)", Presented in the 49th Annual Conference on Magnetism and Magnetic Materials, Jacksonville, Florida, November, 7-11, 2004.

12. I.E. Anderson, W. Tang, R.W. McCallum. "Particulate processing and high-performance permanent magnets". *International Journal of Powder Metallurgy.* Vol 40:6 (2004) 37-60.

CHAPTER 4: PROPERTIES OF POLYMER BONDED PERMANENT MAGNETS MADE WITH MELT-SPUN RIBBON

A paper published in *Advances in Powder Metallurgy & Particulate Materials - 2005*[1]

N.L. Buelow[2], I.E. Anderson[3*], R.W. McCallum[4], M.J. Kramer[5], W. Tang[6], and K.W. Dennis[7], and S. Constantinidies[8]

ABSTRACT

Usage of neodymium-iron-boron permanent magnets in sintered and bonded form is growing rapidly as the price of raw materials has declined relative to alternatives. While sintered magnets offer the highest energy output, bonded magnets offer complex shape and magnetization patterns. Bonded magnets are also net shape and can often reduce subsequent assembly steps through insert and multi-component molding. With improvements to the constituent magnetic powders of polymer bonded magnets, useful energy products can be obtained. Of particular interest is the novel mixed rare earth iron boron system ($MRE_2Fe_{14}B$). Melt spun $MRE_2Fe_{14}B$ ribbon can be crushed in an inert environment creating a fine powder that is suitable for polymer bonding. Environmental testing will give insight into the robustness of the magnetic properties and the effect of surface coatings during short and long term exposure to elevated temperature.

---

[1] Reprinted with permission from ADVANCES IN POWDER METALLURGY & PARTICULATE MATERIALS 2005, Metal Powder Industries Federation, 105 College Road East, Princeton, New Jersey 08540
[2] Graduate student Materials Science and Engineering and primary author
[3] Adjunct Professor of Materials Science and Engineering and Ames Lab-USDOE Senior Metallurgist
[*] Author for correspondence
[4] Adjunct Professor of Materials Science and Engineering and Ames Lab-USDOE Senior Materials Scientist
[5] Adjunct Professor of Materials Science and Engineering and Ames Lab-USDOE Scientist II
[6] Ames Lab-USDOE Post Doctoral Fellow
[7] Ames Lab-USDOE Assistant Metallurgist
[8] Director of Technology Arnold Magnetic Technologies Corp

INTRODUCTION

Size and weight restrictions influence many engineering designs. Recent permanent magnet (PM) alloy designs have excellent magnetic strength in a small volume, giving a small device the same power as a larger device [1]. The size reduction is the result of PMs with enhanced magnetic properties. Maximum energy product is a measure of the work a PM can do outside its volume. PMs with a high BH_{max} value contain a lot of energy per volume [2]. These new PMs have finely tuned alloy designs and microstructures that directly affect the magnetic properties. Microstructure is the extrinsic factor limiting the intrinsic capabilities of an alloy design. Several processing methods are used to control the microstructure and, therefore, optimize the magnetic properties of PMs. Strip casting and grinding [3], melt spinning [4], hydrogen-decomposition-desorption-recombination [5], and gas atomization [6] are processes that can exert good control over the microstructure. The final output of these methods is a PM powder that can be shaped into different types of commercially useful PMs.

Advanced PM powders have two final forms, sintered fully dense and polymer bonded. Sintered fully dense PMs have a high BH_{max}, but are difficult to fabricate due to their brittle nature [7], which limits the available geometries, and may be attacked by the environment in which they operate [8]. Although much is being done, and has been done, to improve the manufacturability and chemical robustness of sintered fully dense PMs, a polymer bonded magnet (PBM) offers a ready solution to the mechanical, corrosion, and manufacturing issues associated with sintered PMs [9]. A PBM binds the brittle PM powders in a polymer matrix, improving the mechanical properties, compared to sintered PMs. The polymer matrix also encapsulates the PM powders, effectively separating them from the environment. Net shape manufacturing is possible with PBM since the polymer matrix is fluidized at temperatures lower than those which would have a negative effect on the PM microstructure.

PBMs are limited in the BH_{max} value they can achieved as compared to sintered fully dense PMs. As a comparison between bonded PMs and sintered PMs, the BH_{max} of a PBM is proportional to the square of the fill factor (f), where the fill factor is the volume percent of

PM powder in the PBM, see Eq. 1 [10]. This gives the percentage of BH_{max} the PBM will be able to reach as compared to a sintered fully dense isotropic PM.

$$(BH_{max})^{bond} = f^2(BH_{max}) \quad (1)$$

High loading fractions of PM powders are needed to maximize the BH_{max} of a PBM. PBMs will not be able to compete with sintered magnets in terms of BH_{max}. However, they can offer many other advantages sintered magnets do not offer, compensating for the lack of BH_{max}.

Rare earth iron boron PM powders have high BH_{max} values and are currently used in high performance PBMs [11]. Of particular interest is the novel mixed rare earth iron boron ($MRE_2Fe_{14}B$) PM alloy family. This alloy family has excellent temperature dependent magnetic properties. $MRE_2Fe_{14}B$ was designed to minimize the loss of BH_{max} as the temperature of the system is increased [11]. Like other commercial $RE_2Fe_{14}B$ PM powders that are intended for PBMs, $MRE_2Fe_{14}B$ was produced first via melt-spinning, which has control parameters that can dictate the microstructure [12]. This process yielded $MRE_2Fe_{14}B$ in an overquenched (partially amorphous) form that can be annealed to the proper microstructure, with improved magnetic properties [13].

High temperature polymers are also being considered for use with $MRE_2Fe_{14}B$ powders to maximize the temperature range in which the PBMs can operate. Polyphenylene sulfide (PPS) is a high melting temperature polymer that can be blended with $MRE_2Fe_{14}B$ powder to create a PBM. PPS comes in a powdered form which makes it ideal for blending with $MRE_2Fe_{14}B$ powders.

A major concern when working with any of the rare earth PMs is irreversible loss of magnetic properties that occurs as a result of corrosion [8]. The powders in PBMs are encapsulated in the polymer binder as a result of the fabrication process, but exposure to high temperature or humidity, as well as immersion in some fluids can promote deleterious powder surface reactions, in spite of the polymer matrix. Fortunately, the PM powders can also be passivated to further increase their resistance to corrosion. The addition of a

passivated layer can be accomplished through the use of a modified fluidized bed process [14] and its effect will be reported.

EXPERIMENTAL PROCEDURE

The $MRE_2Fe_{14}B$ alloy composition $[Nd_{0.45}(YDy)_{0.25}]_{2.2}Co_{1.5}Fe_{12.5}B$ was used in all the experiments for this study and was produced via melt-spinning which yielded an overquenched partially amorphous ribbon. This ribbon was annealed at 700^0C for 15 minutes to optimize the microstructure. During the annealing process the ribbon was wrapped in a tantalum foil packet and sealed in a quartz vessel at 1/3 atm of ultra high purity helium. Due to the small scale of the lab process, ~8g, seven melt-spinning runs had to be done to produce adequate material for the bonding process. A piece of annealed ribbon was tested from each batch to ensure consistent magnetic properties. After testing the consistency of the magnetic properties across the entire batch, the ribbon was crushed into a flake form. This was accomplished by placing the annealed ribbon on a 425μm ASTM standard sieve along with ceramic grinding media. Vibration was applied to the sieve, in an inert environment, to promote low energy crushing of the $MRE_2Fe_{14}B$ ribbon. Samples of flake were then blended with epoxy, and PPS.

To protect the $MRE_2Fe_{14}B$ powders from irreversible losses due to corrosion, a modified gaseous fluorination process was used to passivate the surface of the powders. The experimental fluorination process was a small batch process, with ~7g per run. The powder was sealed in a reaction chamber and heated to 160°C in an atmosphere of flowing argon, the carrier gas. To ensure that the flakes were coated evenly, they were stirred magnetically. Due to the geometry of the flake powder, pure gaseous fluidization is extremely difficult, thus the addition of magnetic stirring. When the particles reached the reaction temperature, 160°C, the nitrogen trifluoride (NF_3) reaction gas flow was begun at 0.5% of the total gas flow through the chamber. The reaction on the flake surface was considered complete when the residual gas analyzer used to monitor the exhaust gas showed an increase and stabilization of the NF_3 concentration and a decrease and stabilization of the nitrogen concentration. The NF_3 and nitrogen were monitored continuously during the fluorination process.

When the sample had completed the fluorination process, a small sample was prepared for thermal gravimetric analysis (TGA), Auger, and x-ray photoelectron spectroscopy (XPS). TGA determined if the coating was effective in preventing air oxidation. Auger and XPS determined the thickness and chemical composition of the fluoride coating. Finally, all the powders, treated $MRE_2Fe_{14}B$, untreated $MRE_2Fe_{14}B$, and commercial powders (used as a standard) were bonded with epoxy or PPS for environmental testing. The pressed PBM were then machined to a permeance coefficient of two which is determined by the length and diameter of the sample.

A set of the bonded PMs were also subjected to a short term irreversible loss test (STILT). This involves pulse magnetization of the bonded PMs and measurement of the Helmholtz flux in the as-bonded state at ambient temperature giving a baseline flux for the PBMs. The PBMs then were heated for one hour, in air, at a specified temperature. Then, the sample was allowed to cool to room temperature for one hour and the Helmholtz flux was measured again. This process was continued, with a temperature increase each time, to the specified maximum temperature. The final step is to re-saturate the tested PBM and to measure its Helmholtz flux again to determine the actual irreversible loss due to microstructural degradation.

RESULTS

For the PM powders to retain their magnetic properties, protection from the environment in which they operate is needed. Encapsulating the powder in the polymer matrix of the PBM is effective, generally, in limiting environmental access to the PM powders under normal ambient conditions. However, for applications involving elevated temperatures, for example, another form of protection is, needed, consisting of the addition of a passive layer on the surface of each particle. TGA experiments, Figure 1, subjected passivated and unpassivated $MRE_2Fe_{14}B$, along with two commercial PM powders to a 5°C/min temperature ramp up to 300°C. The powders were then held at 300°C for three hours. This temperature schedule was done in an atmosphere of flowing dry air. Inspection of the relative weight gain in Figure 1 shows the passivation process was effective in growing a protective layer around the powder particles that reduced the amount of mass gain,

as compared to unpassivated $MRE_2Fe_{14}B$ and commercial Nd-Fe-Nb-B powder, as determined by TGA.

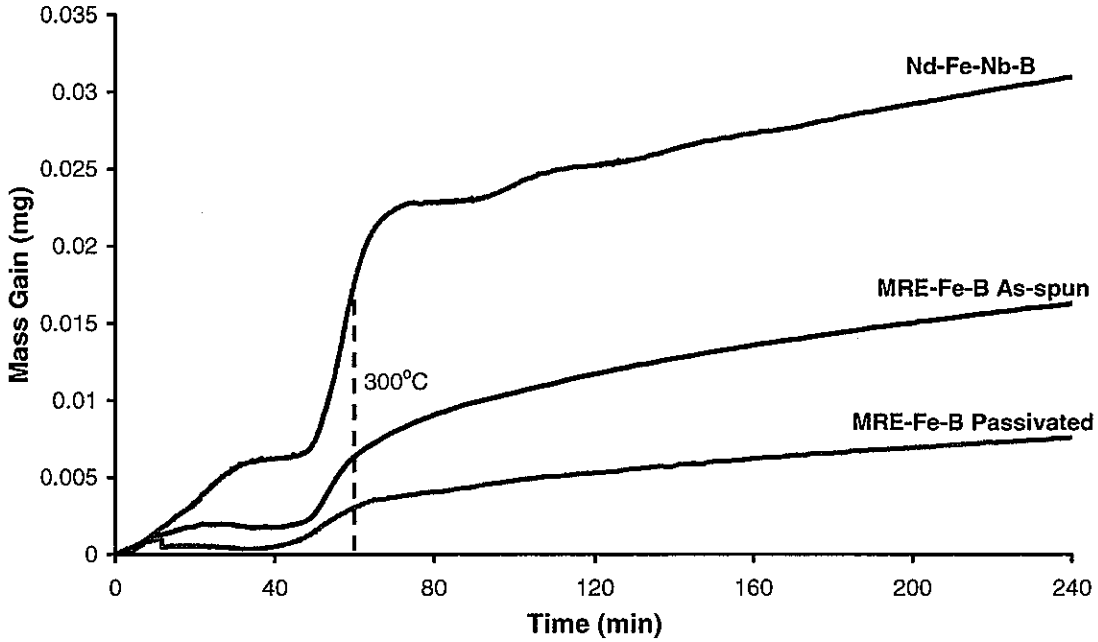

Figure 1: TGA results for $MRE_2Fe_{14}B$ in a passivated and unpassivated state with comparisons to two commercial PM alloys.

Thickness of the coating is important as it was assumed that growing the passive coating would consume rare earth from the near-surface region of each powder particle. Removal of rare earth from the magnetic phase will reduce the BH_{max} of the PM powders, decreasing the BH_{max} of the PBM. An optimal coating thickness must be determined that protects the powders but doesn't represent a significant decrease in BH_{max}. Coating thickness and composition were determined using Auger and XPS.

Data from Auger (see Figure 2) shows three of the four primary elements in the passive surface coating: fluorine, iron, and oxygen. Rare earths are hard to identify specifically with Auger due to their similar energy spectrums overlapping with each other and with associated iron peaks. The oxygen peak was the first to dissipate as the surface layers were removed by argon ion sputtering for only 15 cycles, or about 15nm. As the number of sputtering cycles increased the oxygen peak, present on the surface, disappears as the Auger scans deeper into the particle. Quantifying the difference between iron and

fluorine in the fluoride, $(RE)F_3$ compound proves to be difficult for particles with a thin layer of fluorine on the surface. A strong fluorine signal is needed because the fluorine peak shows up as a shoulder at 656eV [15] on the iron peak at 650eV [16]. Knowing this, the depth to which the fluorine reacted is determined by observing drift or splitting in the iron peak. The intensity of the fluorine peak as compared to the iron peak appeared to decrease as a function of distance from the particle surface. As the fluorine peak disappeared, the shoulder had less of an influence on the iron peak, causing the iron peak to shift and change shape (at a depth of about 40nm), as a good indication of coating thickness. The most encouraging result shown in Figure 3 is that the fluorine peak persisted further into the particle than the oxygen peak. This means the oxygen did not reach the $MRE_2Fe_{14}B$ phase and, therefore, will not affect the magnetic properties.

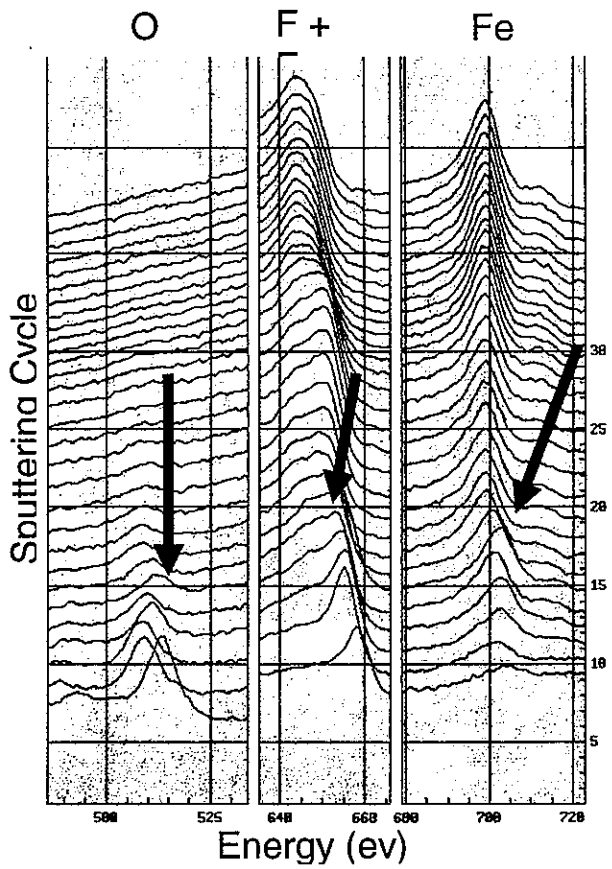

Figure 2: Auger results for O, F+Fe, and Fe at taken at different depths in the microstructure. One sputtering cycle removes ~1nm of material.

XPS was used, as well, to determine the approximate depth and the elements that were present in the passive surface layer. This analytical method has better energy resolution, but samples a much larger area (multiple flake particulates), as compared to Auger. The increased energy resolution allowed for better separation of the iron and fluorine peaks, as well as the individual rare earth spectrums. As noted, XPS samples a much larger surface area than Auger, requiring that the small flakes be laid out in a flat mosaic pattern to make a sample that is ~1mm^2.

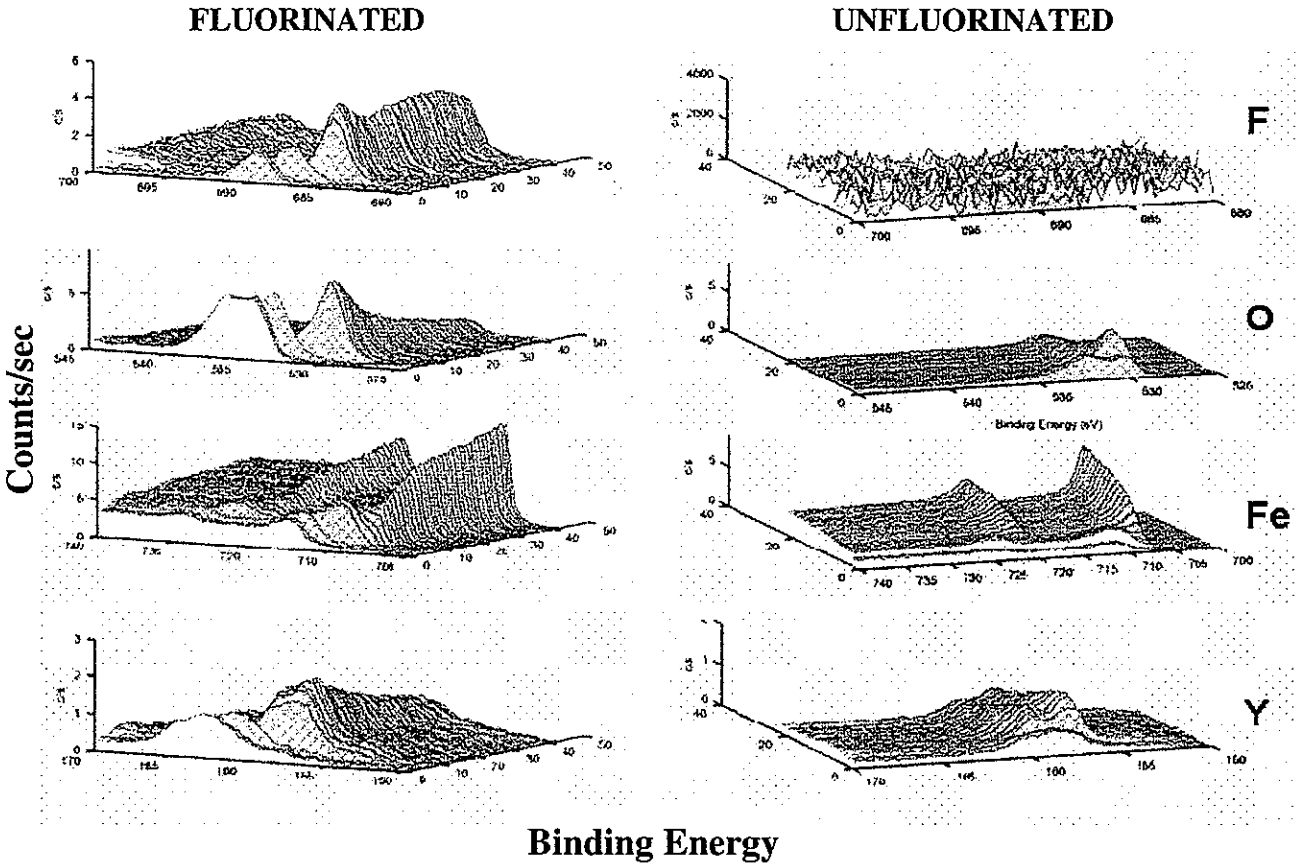

Figure 3: XPS results showing the difference in surface composition for passivated and unpassivated $MRE_2Fe_{14}B$.

XPS reasonably determined the elements contributing to the passive coating, see Figure 3. Yttrium showed up on the surface of the particles along with the iron, fluorine, and oxygen which had been previously determined with Auger. This was determined by looking

at the significant shift in the peaks associated with yttrium as compared to essentially no shift for dysprosium and neodymium. The surface peaks were shifted to a lower bonding energy level as compared to the peaks measured deeper in the bulk of the material. There is a possibility of dysprosium and neodymium appearing in some small proportion in the passive layer, but XPS shows that yttrium seems to be the preferred reactant with the fluorine.

As stated earlier the thickness of the surface coating is important and it was found that the fluorine does react with the REs, especially yttrium, creating a mixture of RE-F-O, Fe-F, and O-F compounds in the passive layer. The thicknesses of the coating ranged from 5 to 80nm. Coatings in the range of 15nm appeared to be thick enough to prevent substantial corrosion of the particulate and to reduce the associated irreversible loss of magnetic properties. This decision was based on the ability to establish a reduced depth at which the oxygen peaks penetrated, relative to the fluorine peaks, especially from the Auger results.

DISCUSSION

Before testing $MRE_2Fe_{14}B$ in a bonded magnet form, it was necessary to demonstrate a reduction in the loss of magnetic properties over a temperature range as compared to commercial $Nd_2Fe_{14}B$, as unbonded ribbon fragments. This initial test was completed in the ideal environment of a vibrating sample magnetometer (VSM) that was fitted with a superconducting 9T magnet, which could fully saturate each sample. The BH_{max} values of $MRE_2Fe_{14}B$ and commercial Nd-Fe-Nb-B were measured over a range of temperatures, terminating at the Curie temperature, to investigate the loss of BH_{max} as a function of temperature, Figure 4.

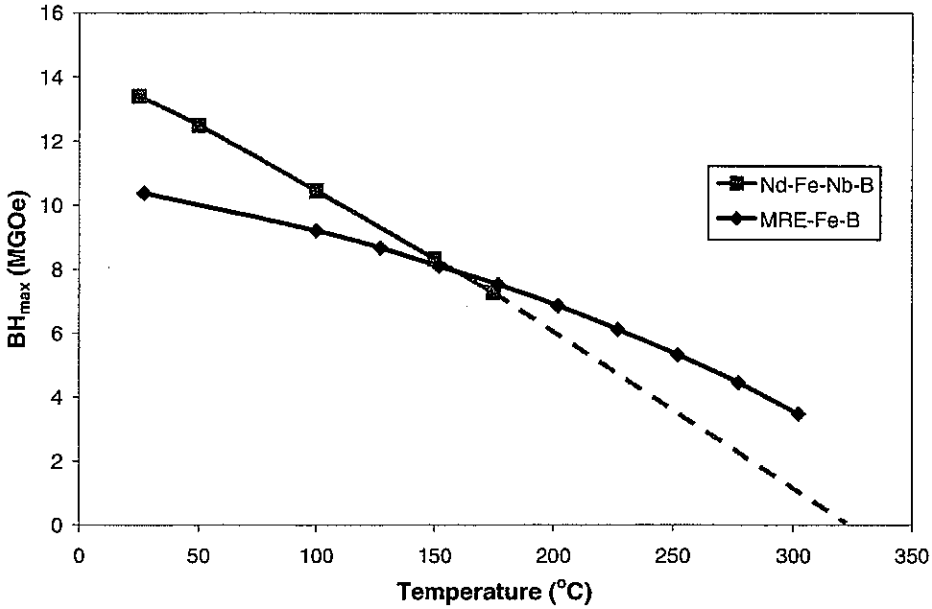

Figure 4: BH_{max} as measured using a VSM for both alloys.

The $MRE_2Fe_{14}B$ alloy $[Nd_{0.45}(YDy)_{0.25}]_{2.2}Co_{1.5}Fe_{12.5}B$ only had a 27% loss in BH_{max} as compared to a 50% loss of BH_{max} for the commercial Nd-Fe-Nb-B in the temperature range of 25 to 200°C. Thus, the ability to stabilize the BH_{max} over an increased temperature range was demonstrated. However, testing of $MRE_2Fe_{14}B$ now needed to move out of the ideal test situation (aligned ribbon pieces in the VSM) into one that better simulates real systems. Polymer bonded PMs made with $MRE_2Fe_{14}B$ gave insight on how the powders will interact with associated binders.

Initial tests were done with unpassivated $MRE_2Fe_{14}B$ flake bonded in a compression molded epoxy matrix. This is the preferred method for making industrial STILT samples. The epoxy used is a one part dry epoxy blended with magnetic particles and compressed to densify the sample. Samples bonded with PPS were heated to soften the PPS. Compression molding was used to cause PPS to wet the surface of the particles, bonding and removing most of the air from the PBM. Large amounts of air in the bonded magnets can create voids which reduce magnetic strength and act as stress concentration points.

Table 1: Comparison of the trapped air and density of the epoxy and PPS bonded magnets.

EPOXY	% Total Vol	EPOXY	% Total Vol
Nd-Fe-Nb-B	76.7%	$MRE_2Fe_{14}B$	75.1%
Epoxy	9.6%	Epoxy	9.4%
Zinc Stearate	0.5%	Zinc Stearate	0.5%
Air	13.2%	Air	15.0%
PPS	% Total Vol	PPS	% Total Vol
Nd-Fe-Nb-B	54.5%	$MRE_2Fe_{14}B$	65.4%
PPS	39.3%	PPS	32.1%
Air	6.2%	Air	2.5%
		$MRE_2Fe_{14}B$ FL	59.5%
		PPS	29.2%
		Air	11.4%

The data in Table 1 was measured from the PBMs used in the STILT. Using the measured weight of the PBM samples along with the known density of the materials that make up the bonded magnets, the vol% of each material that comprises the PBM was determined. Air is used to make up the remainder of the volume in the calculations, should the sum of the volume of PM powder and binder be less than 100%. Lower loading fractions of PM powders were used when bonding with PPS. The reason that the untreated $MRE_2Fe_{14}B$ PM flake bonded with PPS is loaded higher than Nd-Fe-Nb-B and $MRE_2Fe_{14}B$ FL (fluorinated $MRE_2Fe_{14}B$), is due to a change in sample size during the bonding process. A large PPS and $MRE_2Fe_{14}B$ sample was blended, and a small batch was removed from the large batch. It was assumed that the proportion of $MRE_2Fe_{14}B$ powder to PPS would be constant, but this did not hold true. However, STILT test results are normalized, canceling out the effect of the flake powder loading in the samples. The STILT flux measurements, shown in Figures 5, 6, and 7 are represented as a percentage of the starting flux.

The first STILT results (see Figure 5) used epoxy as the binder phase for the bonded magnets to compare commercially available $Nd_2Fe_{14}B$ PM powder to $MRE_2Fe_{14}B$ powder. The PBM containing $MRE_2Fe_{14}B$ flake powder in this test did not have a passive layer; it was bonded in an as-annealed condition. The passivation process was not developed well enough to be used on the powder samples for this test. Figure 5 displays the results of the STILT measurements for these epoxy bonded magnets.

The epoxy bonded magnets made from commercial flake powders (Nd-Fe-Nb-B) outperformed the PBMs with $MRE_2Fe_{14}B$ powder, as shown in Figure 5. Not only did Nd-Fe-Nb-B lose less flux as a function of increasing temperature, but also had the least irreversible loss, after resaturation, due to structural damage. The maximum difference in flux loss, and irreversible flux loss, between the $MRE_2Fe_{14}B$ PBMs and the commercial PBMs is ~1%.

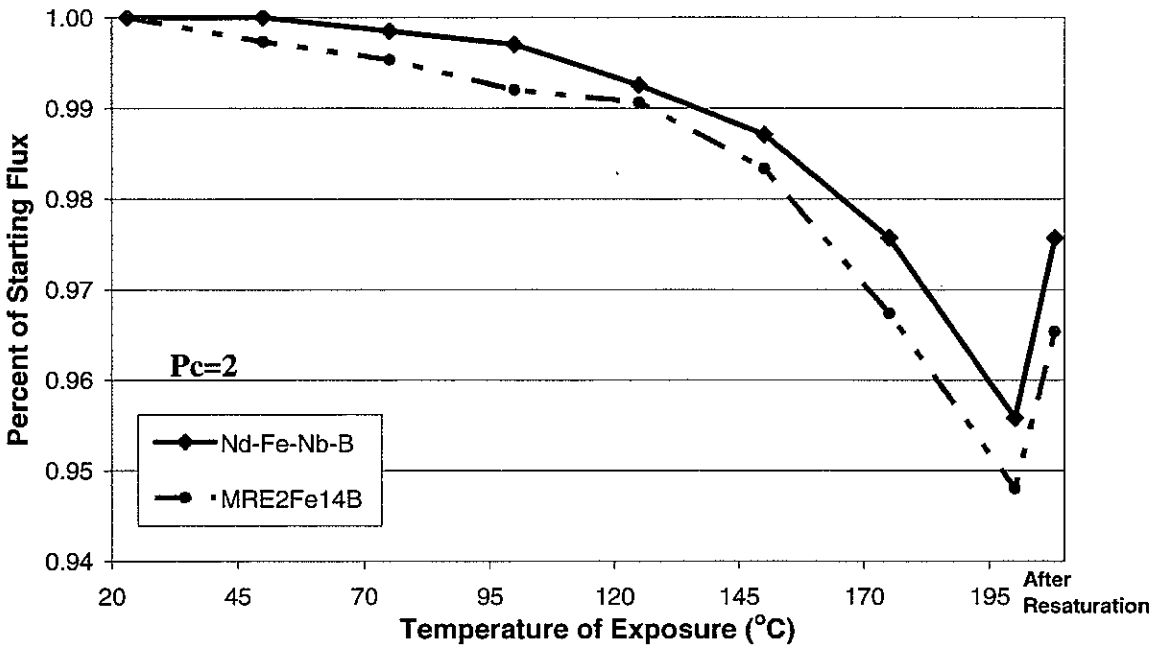

Figure 5: Epoxy bonded magnets subjected to STILT, comparing commercial Nd-Fe-Nb-B and $MRE_2Fe_{14}B$ powder.

The epoxy used to bond the two different types of powders was known to attack the powders that make up the PBM. The exothermic reaction that cures the epoxy may have been detrimental preferentially to the unprotected $MRE_2Fe_{14}B$ powders, increasing the magnetic loss before the start of the STILT. During STILT testing, an increase in the rate of flux loss for each temperature exposure above 150°C apparently caused the epoxy to become more aggressive to the PM powders. To eliminate this possibility the commercial PM powder and the $MRE_2Fe_{14}B$ powder were compression molded using PPS, which is known not to have an exothermic curing reaction. The attack due to the epoxy binder reinforced the need to protect the $MRE_2Fe_{14}B$ powders from their environment.

$MRE_2Fe_{14}B$ was designed to work at higher temperatures than commercial Nd-Fe-Nb-B by using the yttrium dysprosium, and cobalt additions to increase the useful operating temperature range. PPS is considered the binder of choice for $MRE_2Fe_{14}B$ due to the fact it is minimally reactive, hydrophobic, solvent resistant, and mechanically strong at the operating temperatures of interest [17]. The STILT results involving PPS bonded PBMs are more encouraging than the results for the epoxy bonded PBMs, especially in the fluorinated $MRE_2Fe_{14}B$, see Figure 6.

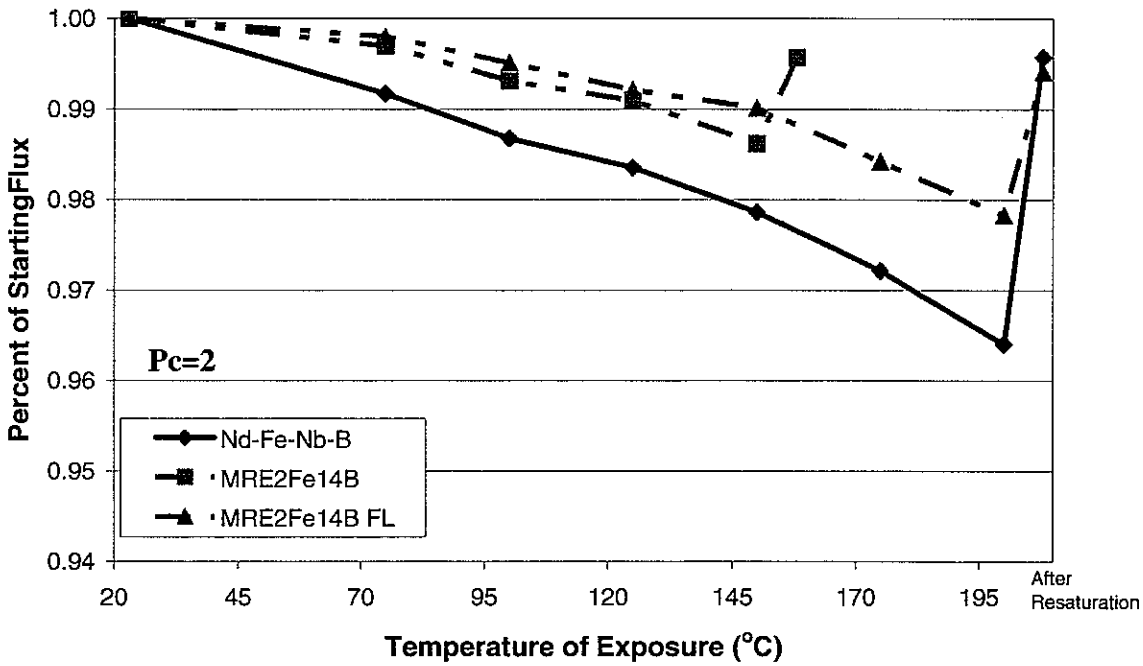

Figure 6: STILT results for bonded magnets using PPS as the binder phase for the commercial Nd-Fe-Nb-B and $MRE_2Fe_{14}B$.

The $MRE_2Fe_{14}B$, fluorinated and unfluorinated, PPS bonded PMs showed less loss of Helmholtz flux than Nd-Fe-Nb-B powders. The passivated $MRE_2Fe_{14}B$ powder in PBM form resisted the loss of Helmholtz flux better than the commercial Nd-Fe-Nb-B PBM and the untreated $MRE_2Fe_{14}B$ PBM. The untreated $MRE_2Fe_{14}B$ PBM was not tested (yet) to 200°C, as were the other two samples shown in Figure 6. Assuming that the untreated $MRE_2Fe_{14}B$ follows the same trend as seen up to 150°C, it will still experience less loss than the Nd-Fe-Nb-B. However, upon resaturation it was found that the commercial alloy PBM

experienced less structural damage than the fluorinated $MRE_2Fe_{14}B$. This issue will hopefully be resolved in the next iteration of the $MRE_2Fe_{14}B$ family of alloys, using TiC to pin the grain boundaries [6].

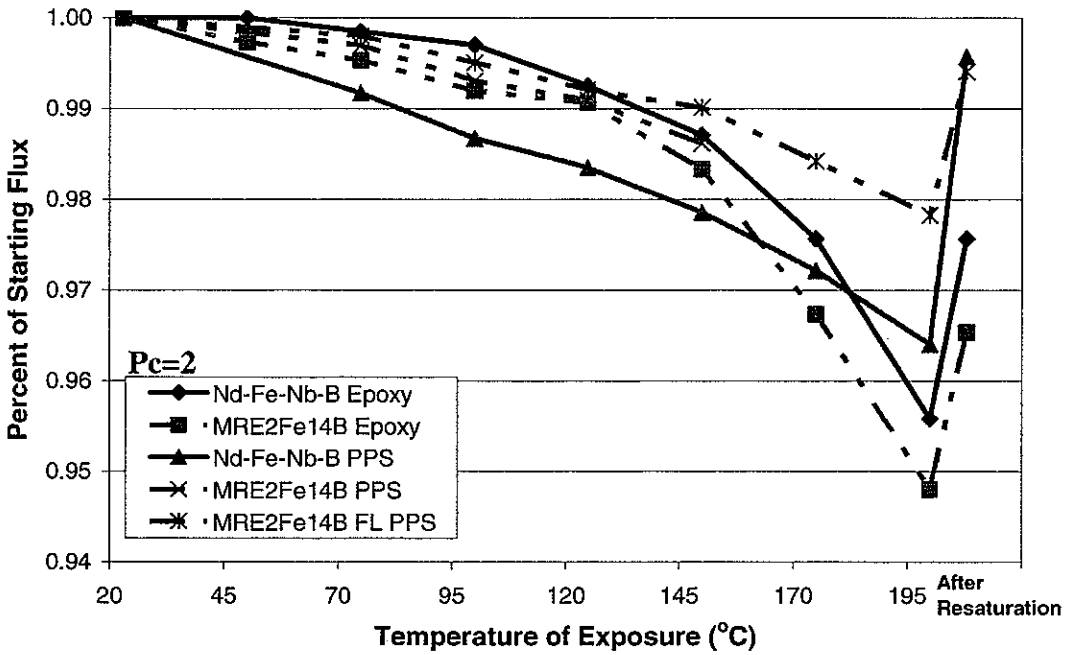

Figure 7: Direct comparison of the Epoxy and PPS bonded magnets that were subjected to STILT.

The use of PPS as a binder phase to decrease the loss of flux as a result of the STILT was successful for the Nd-Fe-Nb-B PM and the $MRE_2Fe_{14}B$ PBM as compared to their epoxy bonded versions, see Figure 7. The effect of the epoxy binder my not be as severe as first thought, but there still appears to be an effect on both types of powders. This is best noted in a comparison of the data from the epoxy and PPS versions of the Nd-Fe-Nb-B alloy in Figure 7. Actually, the results for the highest (200°C) exposure and the final flux loss after resaturation for Nd-Fe-Nb-B were better for the PPS version than the epoxy bonded PM. PPS bonded and fluorinated $MRE_2Fe_{14}B$ powder was able to outperform the commercial Nd-Fe-Nb-B alloy bonded in epoxy and in PPS, regardless, but as mentioned above, progress is needed on the issue of structural damage in the fluorinated $MRE_2Fe_{14}B$ powders.

CONCLUSIONS

$MRE_2Fe_{14}B$, tested in flake form, reduced the percentage of BH_{max} lost over commercial Nd-Fe-Nb-B up to 200°C, as determined by VSM. In the unprotected state $MRE_2Fe_{14}B$ was vulnerable to attack from the epoxy, as shown by the increased loss at 150°C both the Nd-Fe-Nb-B and $MRE_2Fe_{14}B$ PBMs, increasing the need for a protective coating for $MRE_2Fe_{14}B$ powders. A gaseous fluorination system was developed specifically for the creation of a passive surface layer on the $MRE_2Fe_{14}B$ flake powders. Optimal minimum coating thickness was determined to be 15nm, as determined by Auger and XPS. The passive fluoride layer was proven effective against corrosion, showing the least amount of mass gain during TGA experiments. Polymer bonded magnets using PPS did not cause as much structural damage to the $MRE_2Fe_{14}B$ powder the epoxy as shown by the reduction in loss of Helmholtz flux. $MRE_2Fe_{14}B$ flake, with the protective fluoride coating, had less loss of Helmholtz flux than the untreated $MRE_2Fe_{14}B$ and the commercial PM powder.

ACKNOWLEDGMENTS

This work was supported by DOE-EE-FCVT Program, Freedom Car Initiative, USDOE-EE is acknowledged through contract no. W-7405-Eng-82. The authors are grateful for the STILT testing at Arnold Magnetics Technologies on an industrial partnership basis and the Auger electron and XPS work performed by Jim Anderegg at Ames Laboratory.

REFERENCES

1. A. Hütten. "Processing, Structure, and Property Relationships in Nd-Fe-B Magnets". *JOM* March (1992), 11-15.

2. D.C. Jiles. *Introduction to Magnetism and Magnetic Materials.* Chapman and Hall. London. 1991.

3. J. Bernardi, J.Fiddler, M. Sagawa, Y. Hirose. "Microstructural analysis of strip cast Nd-Fe-B alloys for high $(BH)_{max}$ magnets". *Journal of Applied Physics.* Volume 83, Number 11, 1 June 1998. 6396-6398.

4. G.C. Hadjipanayis. "Nanophase hard magnets". *Journal of Magnetism and Magnetic Materials.* 200 (1999) 373-391.

5. R.W. Gao, J.C. Zhang, D.H. Zhang, Y.Y. Dai, X.H. Meng, Z.M. Wang, Y.J. Zhang, H.Q. Liu. "Dependence of the magnetic properties on the alignment magnetic field for NdFeB bonded magnets made from anisotropic HDDR powders". *Journal of Magnetism and Magnetic Materials.* 191 (1999) 97-100.

6. D.J. Branagan, T.A. Hyde, C.H. Sellers, and R.W. McCallum. "Developing rare earth permanent magnet alloys for gas atomization". *Journal of Physics D: Applied Physics.* 29 (1996) 2376-2385.

7. A. Li, W. Li, S. Dong, X. Li. "Sintered Nd-Fe-B magnets with high strength". *Journal of Magnetism and Magnetic Materials.* 265 (2003) 331-336.

8. J. Xiao and J. Otaigbe. "Polymer bonded magnets III. Effect of surface modification and particle size on the improved oxidation and corrosion resistance of magnetic rare earth fillers". *Journal of Alloys and Compounds.* 309 (2000) 100-106.

9. I.E. Anderson, W. Tang, R.W. McCallum. "Particulate processing and high-performance permanent magnets". *International Journal of Powder Metallurgy.* Vol 40:6 (2004) 37-60.

10. D. Goll, H. Kronmüller. "High performance permanent magnets". *Naturwissenschaften.* 87 (2000) 423-4381.

11. ISURF 02935, R.W McCallum., Y, Xu, M.J. Kramer., I.E. Anderson, K.W. Dennis "Permanent Magnet Alloy with Improved High Temperature Performance"

12. M. Seeger, D. Köhler, H. Kronmüller. "Magnetic and microstructural investigations of melt-spun Fe(NdPr)B". *Journal of Magnetism and Magnetic Materials.* 130 (1994) 165-172.

13. W. Tang, K.W. Dennis, Y. Q. Wu, M.J. Kramer, I.E. Anderson, and R.W. McCallum. "Studies of new YDy-based $R_2Fe_{14}B$ magnets for high temperature performance (R=Y+Dy+Nd)". *IEEE Transactions on Magnetics.* 40 (4), July 2004.

14. M.L. Anderson. *Surface Passivation and Electrochemical Behavior of Gas Atomized $LaNi_{4.75}Sn_{0.25}$ for Battery Applications.* Masters Thesis. Iowa State University. (2000).

15. D. Raiser, J.P. Deville. *Journal of Electron Spectroscopy and Related Phenomena.* 57, 91 (1991).

16. M.P. Seah. "Distinction between adsorbed monolayers and thicker layers in Auger electron spectroscopy", *Journal of Physics F: Metal Physics.* Vol. 3 August 1973. 1538-1547.

17. Ticona. "Designing with Fortran Polypenylene Sulfide" http://www.ticona.com/tools/search/lit_details.cfm?docid=27. [Accessed 18 June 2005]

CHAPTER 5: NEW $RE_2Fe_{14}B$ (RE=Y+Dy+Nd) FLAKE AND SPHERICAL POWDER FOR ISOTROPIC BONDED PERMANENT MAGNETS

A paper submitted for publication in *Materials Science and Engineering A - 2005*[1]

N.L. Buelow[2], I.E. Anderson[3*], R.W. McCallum[4], M.J. Kramer[5], W. Tang[6], and K.W. Dennis[7], and S. Constantinidies[8]

ABSTRACT

In recent years concerns have been raised about the temperature dependent magnetic properties of $Nd_2Fe_{14}B$. Novel mixed rare earth iron boron ($MRE_2Fe_{14}B$) was developed to address this issue by reducing the loss of BH_{max} at 200°C by half compared to commercial $Nd_2Fe_{14}B$. This ability to reduce the loss of magnetic properties was observed when testing ribbon pieces in a SQUID magnetometer and when the ribbon pieces were made into a polymer bonded magnet. The ability to retain high temperature magnetic properties was increased though the addition of a protective fluoride layer, 15-40nm thick, grown on the surface of the particles using a modified fluidized bed process. The next challenge is to make fine spherical $MRE_2Fe_{14}B$ via high-pressure gas-atomization with a microstructure and magnetic properties that emulate melt-spun ribbons. Melt-spinning will be used to do the alloy design steps, where estimated microstructures and the phase compositions of atomized powders can be determined from melt-spinning at low wheel speeds.

---

[1] Pre-printed with the permission of *Materials Science and Engineering A*
[2] Graduate student Materials Science and Engineering and primary author
[3] Adjunct Professor of Materials Science and Engineering and Ames Lab-USDOE Senior Metallurgist
[*] Author for correspondence
[4] Adjunct Professor of Materials Science and Engineering and Ames Lab-USDOE Senior Materials Scientist
[5] Adjunct Professor of Materials Science and Engineering and Ames Lab-USDOE Scientist II
[6] Ames Lab-USDOE Post Doctoral Fellow
[7] Ames Lab-USDOE Assistant Metallurgist
[8] Director of Technology Arnold Magnetic Technologies Corp.

INTRODUCTION

The permanent magnet (PM) alloy of choice for use in high performance PBM is an $Nd_2Fe_{14}B$ alloy composition (Nd-Fe-Nb-B) that has been melt-spun so that the flake particulate has a highly refined microstructure consisting of the hard magnetic $Nd_2Fe_{14}B$ phase [1]. Intrinsically, $Nd_2Fe_{14}B$ PMs have an excellent maximum energy product (BH_{max}). Applications, e.g. electric motors, utilizing high performance $Nd_2Fe_{14}B$ PMs can be reduced in size and retain the same power as similar systems without high performance PMs [2]. However, $Nd_2Fe_{14}B$ has another intrinsic property that limits the available range of operating temperatures.

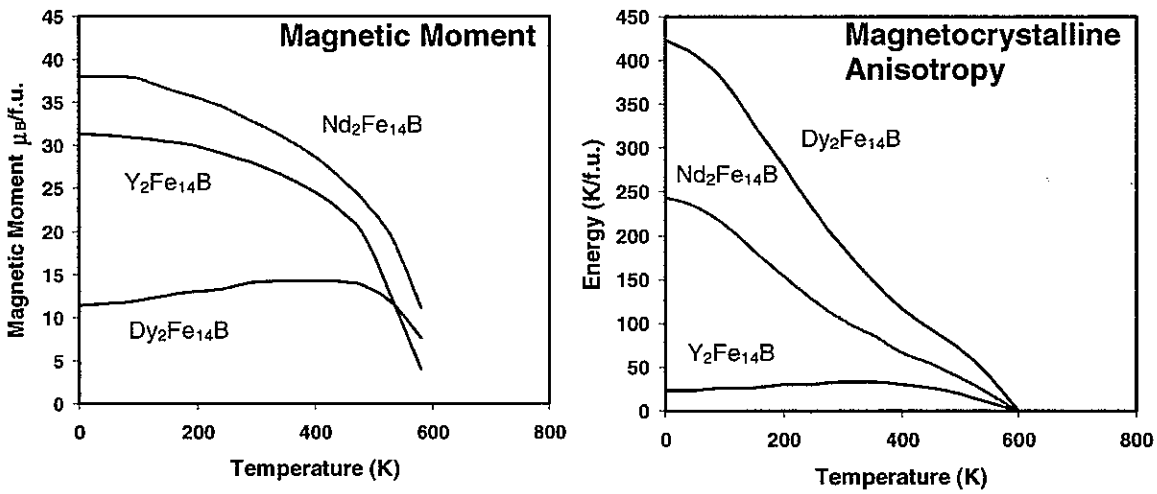

Figure 1: Temperature dependent magnetic properties of three different $RE_2Fe_{14}B$ phases.

The magnetic properties, remanence and coercivity, of $Nd_2Fe_{14}B$ are inversely proportional to temperature. Figure 1 shows the temperature dependent magnetic properties of three $RE_2Fe_{14}B$ phases. $Nd_2Fe_{14}B$ shows significant loss of both magnetic moment and magnetocrystalline anisotropy as a function of increasing temperature. $Dy_2Fe_{14}B$ shows stabilization of the magnetic moment and the magnetocrystalline anisotropy of $Y_2Fe_{14}B$ is stable as the temperature is increased [4]. Reducing the loss of magnetic moment and magnetocrystalline anisotropy over a temperature range will decrease the loss of remanence and coercivity, respectively.

The mixed rare earth iron boron ($MRE_2Fe_{14}B$) alloy family is being developed from these three $RE_2Fe_{14}B$ systems to improve on the high temperature performance of commercial $Nd_2Fe_{14}B$ powder, typically Nd-Fe-Nb-B, with out excessive loss of ambient temperature magnetic properties [4]. Powders from these new alloys are intended for bonding in a polymer matrix in what is termed a polymer bonded permanent magnet (PBM). Magnetic moments in the powder will be unaligned due to random physical positioning of each individual particle in the PBM, thus producing an isotropic PBM.

The alloy design approach utilizing the three $RE_2Fe_{14}B$ phases shown in Figure 1 assumed that an ideal alloying behavior existed between the three $RE_2Fe_{14}B$ phases and would result in an $MRE_2Fe_{14}B$ possessing a symbiosis of the magnetic properties from the three constituent $RE_2Fe_{14}B$ phases [5]. A highly refined microstructure made by rapid solidification also was desirable as it will optimize the magnetic properties of $MRE_2Fe_{14}B$. Rapid solidification techniques have the ability to create an optimally fine microstructure with minimal microsegregation within the particulate [6]. Melt-spinning and high-pressure gas-atomization (HPGA) are rapid solidification techniques are being pursued to process $MRE_2Fe_{14}B$ into a suitable PM powder.

Melt-spinning and HPGA are both capable of reaching cooling rates of 10^6K/s which, for $Nd_2Fe_{14}B$, is able to form amorphous and nanocrystalline microstructures [7]. Melt-spinning, at a high wheel speed creates an overquenched microstructure which can be annealed to form a microstructure that is optimal for hard magnetic properties in ribbon form. The ribbon is typically crushed in an inert environment, resulting in a fine isotropic powder. HPGA cannot reach the through thickness cooling rates seen in melt-spinning at high wheel speeds, but HPGA produces a spherical PM powder directly, eliminating the need for a crushing step.

The spherical form of the HPGA powders also is beneficial in a manufacturing sense for bonded magnet production. Figure 2 shows how a multimodal spherical packing can increase the volume loading of PM powder in a PBM [8]. More PM powder loading in a PBM increases the value of BH_{max} according to Equation 1.

$$(BH_{max})^{bond} = f^2(BH_{max}) \tag{1}$$

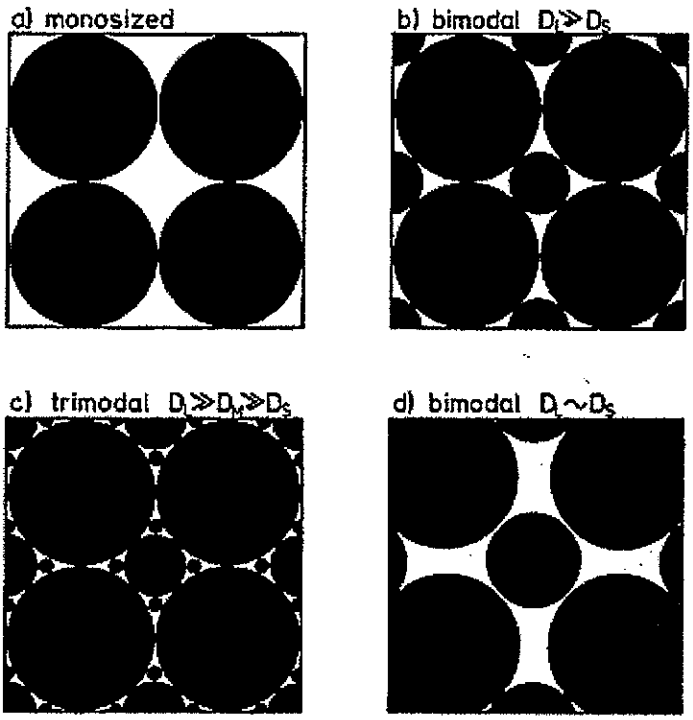

Figure 2: Multimodal packing using spheres with a range of particle diameters [8].

As given in Equation 1, the square of the fill factor (f), i.e, the vol% of PM powder in a PBM, gives the percentage of BH_{max} that a PBM will be able to obtain as compared to an isotropic sintered fully dense PM made from the same material [9]. Also, in Figure 3, the effect of particle geometry is considered on the polymer/powder compound that must be used to mold each PBM to net shape. Flake powders, created from the melt-spinning process, are similar to discs (see Figure 3) and experience a sharp increase in relative viscosity at high solids loading as compared to spherical powders which have a lower relative viscosity at increased solids loading [8]. Lower relative viscosity of blended polymer and spherical PM powders will reduce the pressure requirements (at the same solids loading) for injection molding of blended material [8], for example.

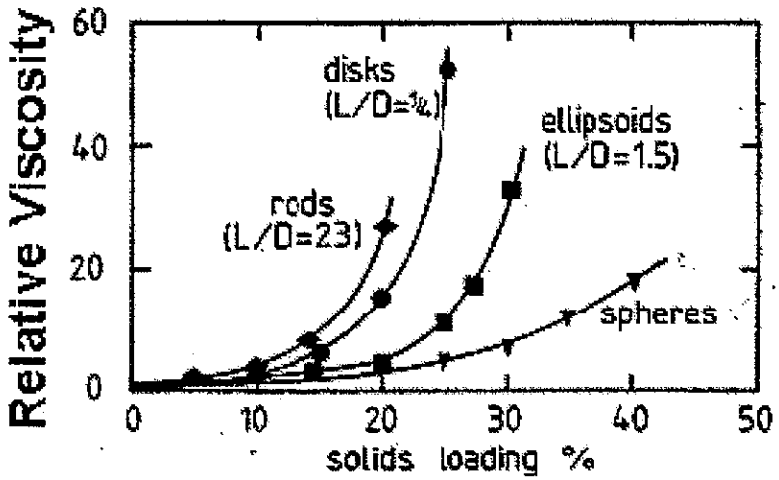

Figure 3: Relative viscosity as a function of solids loading with different geometry particles [8].

EXPERIMENTAL PROCEDURE

Melt-spinning is the commercially preferred method for creation of commercial PM powders. The melt-spinning method can be reduced to a laboratory scale with a batch size of ~8g, as compared the HPGA laboratory scale which produces a 5kg minimum sample size. Alloy design of $MRE_2Fe_{14}B$ for HPGA was performed using melt-spinning, where details of the process have been given elsewhere [10, 11, 12]. More iterations of different $MRE_2Fe_{14}B$ alloy composition could be completed before processing a limited set of selected compositions via HPGA. High wheel speeds (25m/s) were used to simulate commercial melt-spinning and low wheel speeds (10m/s) were used to simulate solidification conditions available during HPGA.

High wheel speeds overquenched the ribbon making it ideal for heat treatment. The overquenched ribbon was annealed at 700°C for 15 minutes in an inert ultra high purity helium atmosphere to obtain a microstructure preferred for hard magnetic properties. The ribbon was made into a powder by placing the annealed ribbon on a 425μm ASTM standard sieve with ceramic grinding media. The sieve was vibrated, in an inert atmosphere, to promote low energy crushing of the ribbon. The crushed ribbon was then subjected to a passivation process where a protective fluoride layer was grown on the surface using a modified fluidized bed process. The modification was the addition of a magnetic stirrer to

assist the gas flow in the fluidization of the powder particles to ensure that an even passive layer is grown across all surfaces of the particle. The fluoride layer was grown at 160°C in a flowing atmosphere of argon at 300 sccm carrying 0.5% NF_3.

This material was intended for commercial (high temperature exposure) environmental testing in a bonded magnet form. Commercial PM and $MRE_2Fe_{14}B$ powders were blended with polyphenyl sulfide (PPS) (58vol% PM powder) and compression molded. The mold was heated to 315°C in a nitrogen atmosphere to promote PPS melting and wetting of the PM powder particles. All PBM samples were machined to a permeance coefficient (Pc) which is a function of the PBMs diameter and length. Molded samples were subjected to a short term irreversible loss test (STILT). To begin each STILT trial, PBM samples were saturated at high field and the Helmholtz flux was measured. Increasingly higher temperatures were used to promote flux loss, saturation was measured after each temperature increase, after cooling to ambient temperature. The maximum temperature tested during STILT was 200°C after which the PBM samples were resaturated to observe actual irreversible loss.

The ribbons made with the low wheel speed were prepared for microstructural, XRD, and magnetic comparisons, in the as-spun state, against a range of different spherical particle sizes in the as-atomized state that were characterized in the same manner. The HPGA process used helium as the atomizing gas to achieve an average particle diameter (d50) of ~20μm, maximizing the amount of powders that have seen the maximum quench rate possible, where other details of the process have been given elsewhere [5]. The gas atomized $MRE_2Fe_{14}B$ spherical powders were size classified, using a series of ASTM standard sieves down to 20μm to separate the <53μm particles out of the full atomized batch. Air classification was used subsequently to separate the <20μm particles into <5μm, 5-10μm, and 10-20μm samples.

RESULTS

Melt-spinning results have been very encouraging and have lent credibility to the alloy design approach behind stabilizing the temperature dependent magnetic properties [10, 11, 12]. As stated above, the $MRE_2Fe_{14}B$ PM alloy family was designed to operate at

elevated temperatures, not with an optimum at room temperature. This rationalizes the lower BH_{max} of $MRE_2Fe_{14}B$ at reduced temperatures, compared to that of commercial $Nd_2Fe_{14}B$ (Nd-Fe-Nb-B) for the results presented in Figure 4. The two alloy compositions of $MRE_2Fe_{14}B$ shown in Figure 4 have only lost ~25% of their room temperature BH_{max} at 150°C. However, a commercial modified composition of $Nd_2Fe_{14}B$ has experienced ~50% loss of its room temperature BH_{max} at 150°C. $MRE_2Fe_{14}B$ is able to equal the commercial alloy in BH_{max} at ~125°C, for the TiC modified $MRE_2Fe_{14}B$ composition, and has a higher BH_{max} at temperatures exceeding 125°C up to its Curie temperature, above 400°C [11]

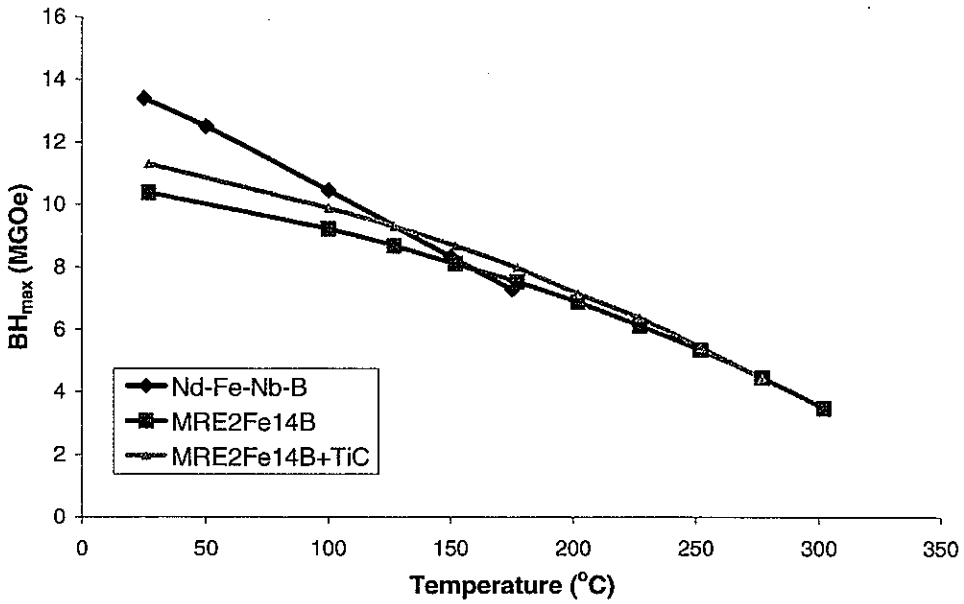

Figure 4: BH_{max} vs. temperature comparing two different $MRE_2Fe_{14}B$ alloys to commercial $Nd_2Fe_{14}B$.

This initial test was completed in the ideal environment of a vibrating sample magnetometer (VSM) that was fitted with a superconducting 9T magnet, which could fully saturate each sample. In the ideal inert test environment $MRE_2Fe_{14}B$ has a higher BH_{max} than commercial $Nd_2Fe_{14}B$ at elevated temperatures. However, $MRE_2Fe_{14}B$ must retain those properties in an actual working environment. Due to a reduction in the amount of heavy rare earth in $MRE_2Fe_{14}B$, and the lack of a low melting eutectic with a RE-rich phase that can coat grain boundaries of $ND_2Fe_{14}B$ grains in non-stoichiometric alloys, it is at an advantage

from a corrosion standpoint. The heavy rare earths corrode readily, but not as readily as the light rare earths [4] and the Nd-rich phase in non-stoichiometric (Fe-poor) $Nd_2Fe_{14}B$ alloys is also a well-recognized corrosion site [3]. To maximize the chemical robustness of the magnetic properties, a protective fluoride coating for $MRE_2Fe_{14}B$ was developed. This coating was grown using the rare earths in the near-surface region of the powder by reacting them with NF_3 [13].

TGA determined if the fluoride coating was effective in protecting the particles from corrosion. The temperature schedule for TGA was an increase of 5°C/min up to 300°C and a hold at 300°C for 3hrs in an atmosphere of flowing dry air. Three samples were tested: commercial $Nd_2Fe_{14}B$, as-annealed $MRE_2Fe_{14}B$, and fluorinated $MRE_2Fe_{14}B$. Results are shown in Figure 5. The fluorinated $MRE_2Fe_{14}B$ experienced the least amount of mass gain as compared to the commercial $Nd_2Fe_{14}B$ and the as-annealed $MRE_2Fe_{14}B$. As expected, the as-spun $MRE_2Fe_{14}B$ experienced less mass gain from TGA than the commercial $Nd_2Fe_{14}B$ which has only "light" rare earth components, i.e., neodymium and a minor amount of Pr [14].

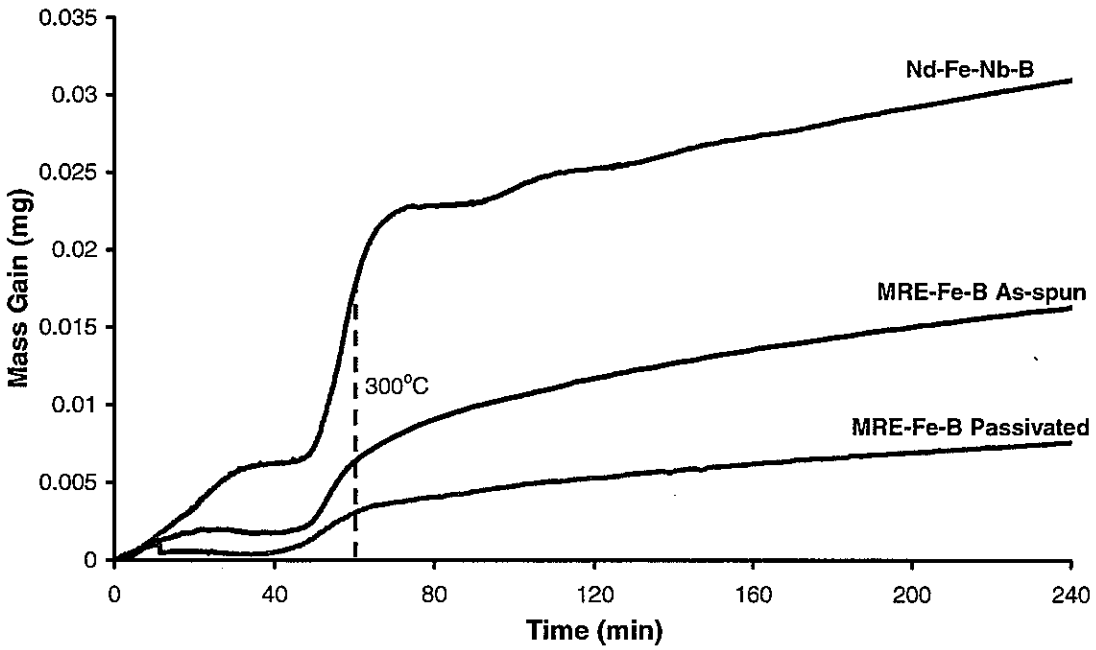

Figure 5: Mass gain for three PM powder samples as a function of temperature in an atmosphere of flowing dry air.

Auger and XPS determined the elemental selectivity of the fluoride coating and the depth to which the fluorine reacted. Due to the characteristic kinetic energies of the Auger electrons for Fe and F, 650eV [15] and 656eV [16] respectively, peak separation is difficult, impeding accurate quantification of the surface composition. However, a shift in the combined F + Fe peak can be observed from the Auger output giving an estimation of the depth at which the fluoride layer terminates. Figure 6 shows the Auger results for F, Fe, and O for a (alloy comp) ribbon fragment that had been treated with fluoride from a 1.0% NF_3 (in argon) gas mixture at 160°C for a series of 15 exposure cycles [13], in early experiments without magnetic stirring. The minimum desirable coating thickness was determined by the depth at which the O signal had significantly decrease, ~15nm into the surface of the powder, in many separate measurements. The importance of determining a maximum thickness is to ensure that the rare earth (RE) that was consumed to grow the fluoride coating does not significantly reduce the magnetic properties. An optimal maximum thickness was determined by observing approximate penetration depth of the fluorine, as determine by Auger, and then comparing it to the color of the particle. Particles between the 15 and 40nm range have a bronze (translucent) color to them.

Auger showed the presence of an oxy-fluoride (O-F) on the surface of the particle, not the intended RE_1F_3 coating, perhaps indicating an inability of the fluoride reaction to reduce (and replace) a pre-existing RE oxide film. Overlapping characteristic Auger spectrums makes determination of the specific RE participating in the fluoride coating difficult. XPS has better energy resolution for RE elements and it was found that yttrium was the preferred reactant with fluorine in the protective coating. The protective fluoride coating on the $MRE_2Fe_{14}B$ particles is most likely a mixture of Y-F and O-F.

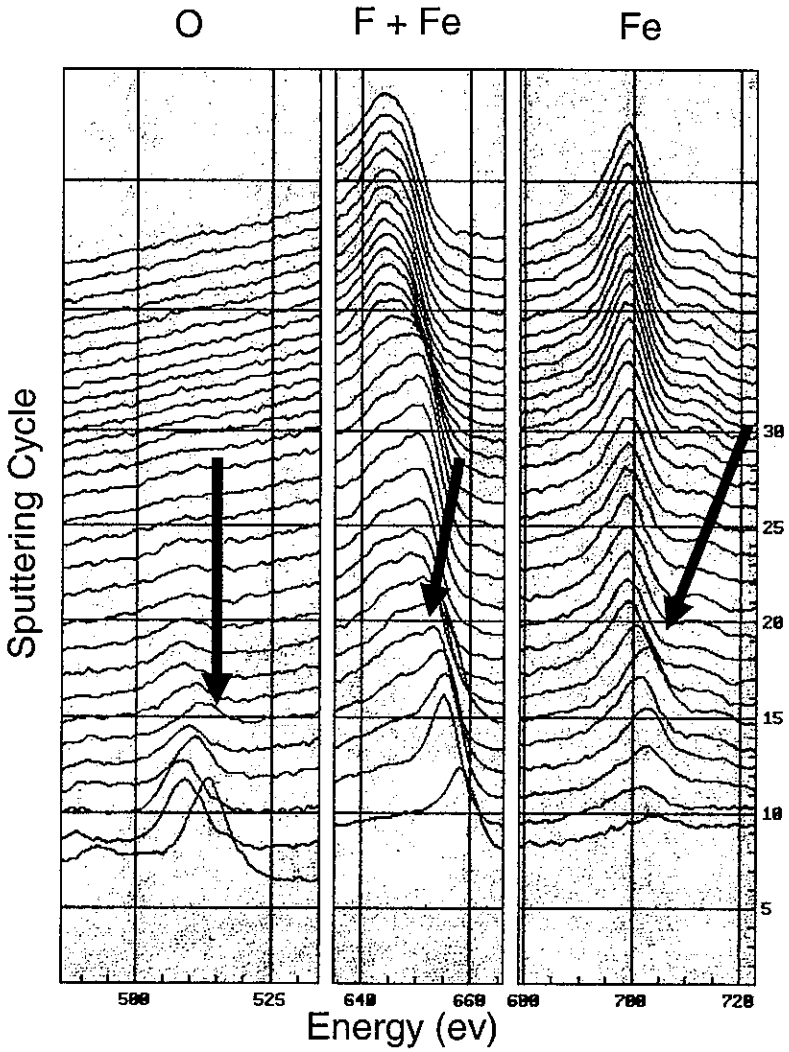

Figure 6: Characteristic Auger electron spectrum for the fluorine, iron, and oxygen in the protective coating on $MRE_2Fe_{14}B$.

The alloy design strategy behind $MRE_2Fe_{14}B$ focuses on high temperature operation. Therefore, a high temperature polymer binder is needed to replace the current commercial epoxy and nylon binders [17]. PPS is regarded as the binder of choice for $MRE_2Fe_{14}B$ powders due the approximate 300°C softening point of PPS along with the intrinsic solvent resistance, being hydrophobic and having high strength. Commercial Nd-Fe-Nb-B and $MRE_2Fe_{14}B$ powders were subjected to STILT trials to compare their ability to retain flux as a function of temperature in an air atmosphere. The STILT results are shown in Figure 7.

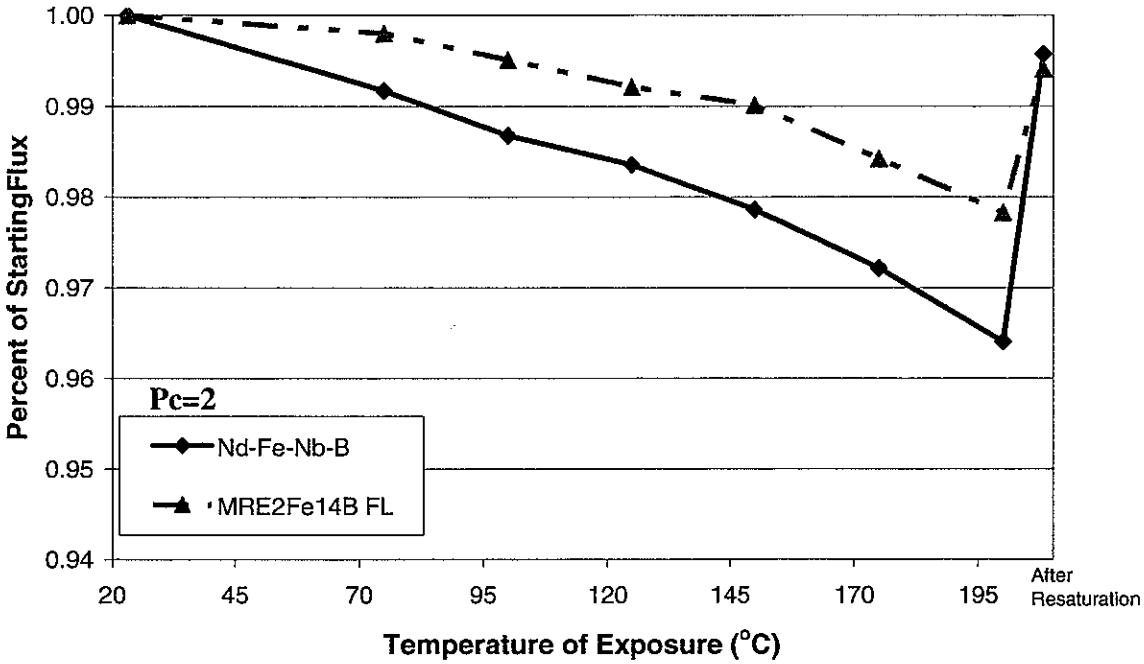

Figure 7: STILT for fluorinated $MRE_2Fe_{14}B$ (MRE2Fe14B FL) and a commercial $Nd_2Fe_{14}B$ powder bonded in PPS.

The $MRE_2Fe_{14}B$ was able to retain more flux over a temperature range from 25°C to 200°C. Although the commercial alloy lost more flux over the temperature range tested it was able to regain slightly more flux after being resaturated as compared to the $MRE_2Fe_{14}B$. This means that the loss seen in the commercial alloy is not due to corrosion or structural damage, but is a function of the intrinsic temperature dependent magnetic properties of $Nd_2Fe_{14}B$.

DISCUSSION

High performance $Nd_2Fe_{14}B$ PM flake powders have been in the commercial market as a universal particulate filler for bonded magnets for many years, but certain important deficiencies still limit the ability of a PBM to be used in applications that currently use sintered fully dense PMs. One deficiency arises because of the flake shape and is mostly due to the packing factor and relative viscosity issues discussed earlier. A simple change in geometry due to a change in processing method will allow PBMs a more competitive advantage as an alternative to sintered fully dense PMs. If HPGA is able to directly produce

fine spherical powders with an optimum microstructure and magnetic properties, an increase in packing factor and a reduction in the relative viscosity of the blended PM and polymer powders can result, which is advantageous to high-output injection molding.

To accomplish the challenge of translating a promising $MRE_2Fe_{14}B$ alloy design from melt-spinning to gas atomization processing, a considerable amount of experimental work is required and is still on-going. The difficulty in using melt-spinning to do alloy design for HPGA relates to cooling rate and type of cooling used to achieve rapid solidification. Melt-spinning uses direct contact with a rotating copper wheel to quench the molten material, therefore, quench rate is dependent on melt superheat and wheel speed [18]. In HPGA the quench rate is dependent on the break-up of the melt stream and the ability of the atomizing gas to convectively cool the molten droplets [19]. The spherical powders made by HPGA experience containerless solidification. Containerless solidification limits the number and type of active nucleation sites, and requires higher undercooling levels to activate nucleation of the phases seen in a melt-spun version of the same alloy composition [20]. Melt-spinning also involves contact with the wheel surface, with an increased potency heterogeneous nucleation. This could effectively decrease the energy barrier to nucleation of the desired $MRE_2Fe_{14}B$ phase or an undesired phase, e.g. MRE_2Fe_{17}. This high nucleation potency of the wheel surface often motivates the use of high wheel speeds to exploit "kinetic undercooling" from the high quench rate to bypass any crystalline nucleation, preferring instead the glassy "overquenched" phase in these alloys.

It is possible to estimate microstructure and phase composition of the HPGA powders from the microstructure of melt-spun ribbon. Using cooling rate models for gas atomized powders [21] and melt-spun ribbon [22] (along with experimental data for melt-spun ribbon [23]) the particulate size that will see an average cooling rate similar to the average cooling rate of melt-spun ribbon, based on ribbon thickness, can be determined (see Figure 8). The heat transfer coefficient (h) for melt spinning was varied from values that would be expected experimentally to the maximum possible value ($\sim 10^6$ W/m^{2}K) [24] to give a range of cooling rates possible in melt-spinning. From these calculations it was estimated that particles <20μm could see average cooling rates similar to average cooling rates of ribbon spun at a low wheel speed. However, due to the difficulty, (near impossibility), of experimentally

measuring cooling rates of very fine HPGA particles, there is some inherent error in the calculations. This is why the cooling rates appear higher than expected for HPGA powders. So a range of powder sizes encompassing the predicted particle size must be tested.

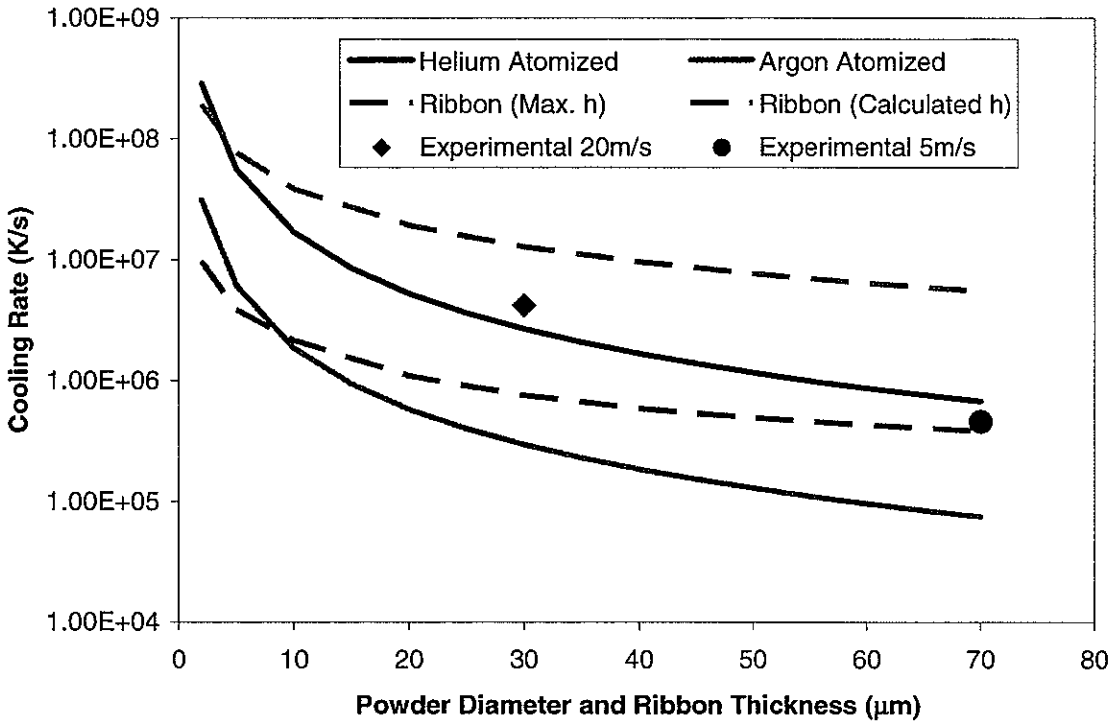

Figure 8: Calculated cooling rates for melt-spun ribbon and gas atomized powders accompanied by experimentally determine cooling rates for melt-spun ribbon.

Using the calculated average cooling rates, a wheel speed of 10m/s and particles <53μm were used for this study. XRD of the free side and the wheel side of $YDyFe_{14}B$ melt-spun ribbons yielded the $MRE_2Fe_{14}B$ phase with little sign of the MRE_2Fe_{17}, see Figure 9.

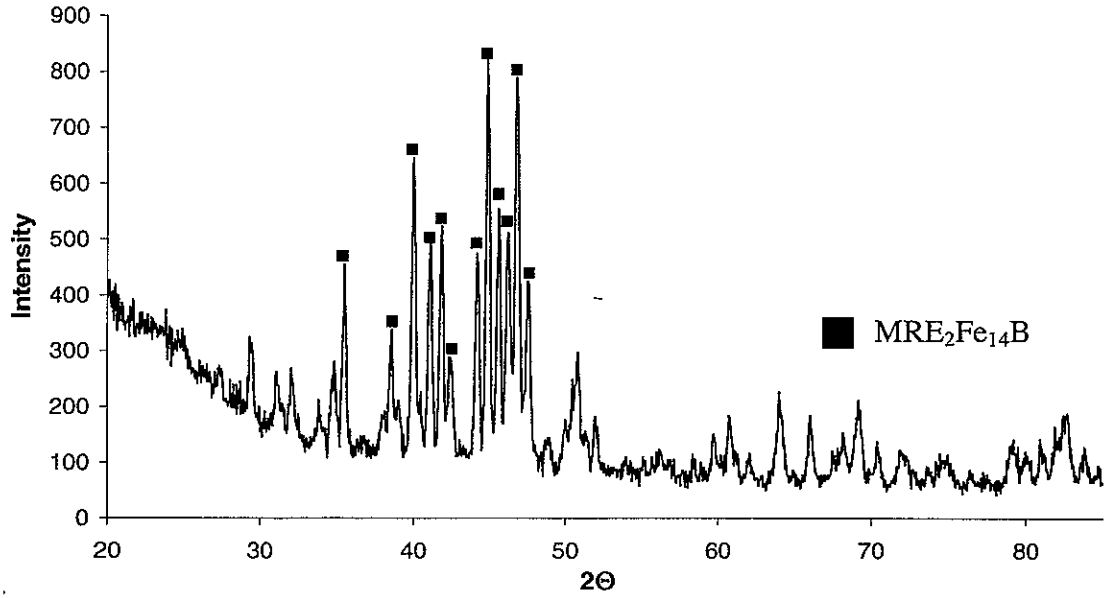

Figure 9: XRD data for the free side of $YDyFe_{14}B$ showing a characteristic $MRE_2Fe_{14}B$ pattern.

The MRE_2Fe_{17} phase field covers the $MRE_2Fe_{14}B$ peritectic line compound and would be the primary phase at reduced undercooling. For all the gas atomized particle sizes analyzed of the same alloy the MRE_2Fe_{17} phase was the primary phase, as determined by XRD in Figure 10.

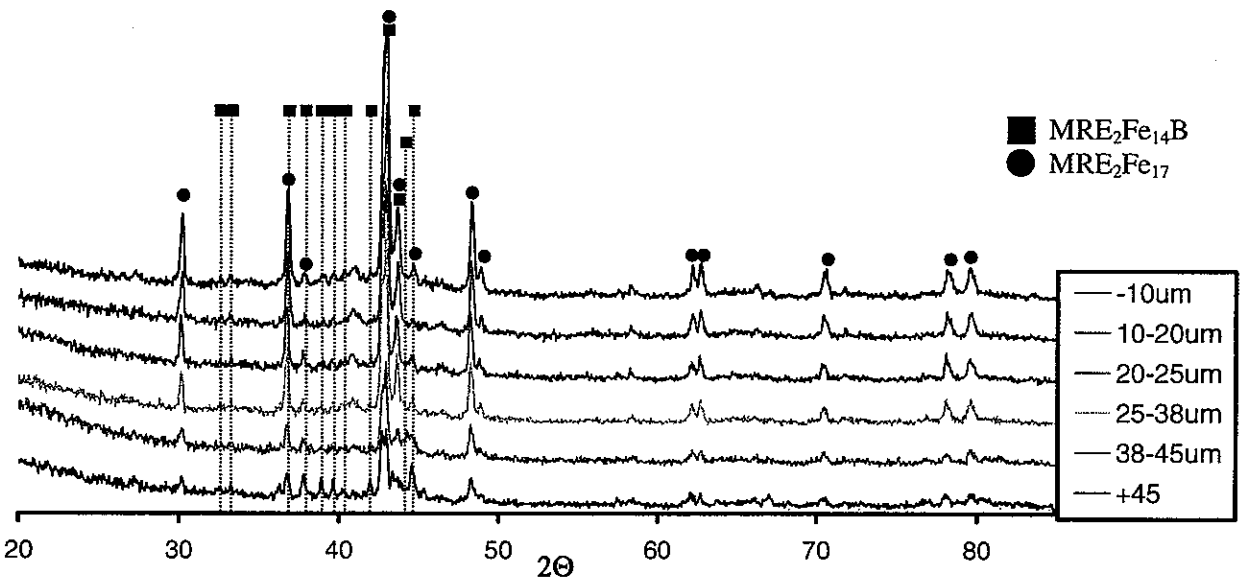

Figure 10: XRD data for $YDyFe_{14}B$ showing a characteristic MRE_2Fe_{17} pattern. Peaks characteristic of MRE_2Fe_{17} and $MRE_2Fe_{14}B$ are labeled.

Investigation of the microstructure of HPGA powders and melt-spun ribbon of $YDyFe_{14}B$ revealed another difference. All of the powders had a dendritic structure while the ribbon had a nanocrystalline structure on the wheel side and a microcrystalline structure on the free side. The high degree of cracking seen on the free side of the ribbon is due to the high degree of crystallinity. The microstructures for the <10μm powders, the smallest tested, and the free side of the melt-spun ribbon, where the slowest cooling rate are seen, see Figure 11.

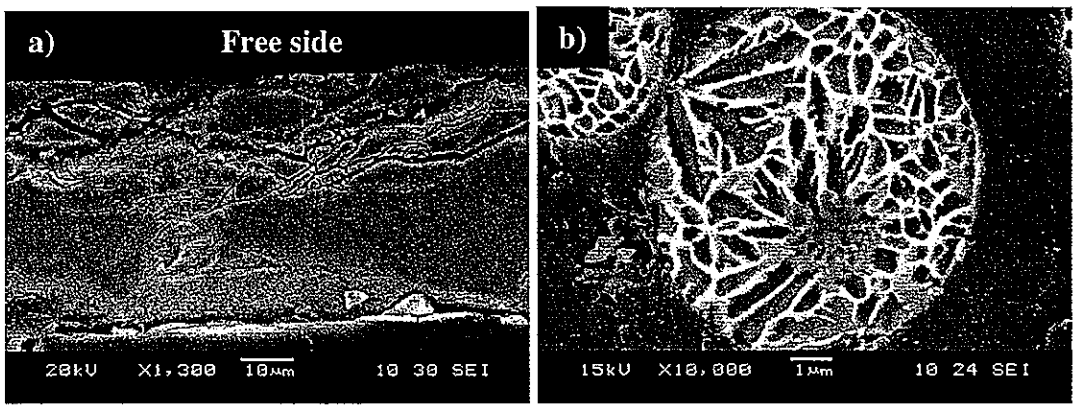

Figure 11: Polished and etched SEM microstructures of $YDyFe_{14}B$ from (a) a transverse section of the melt spun ribbon and of (b) a central cross-section of a typical atomized particle <10μm.

The $YDyFe_{14}B$ composition was not able to reach cooling rates high enough to quench out a microstructure optimal for magnetic properties using HPGA. Therefore, a potent nucleation catalyst was added to decrease the quench rate needed to form the desired phase and microstructure. This alloy design step used Zr as the nucleation catalyst creating $[Nd_{0.45}(YDy)_{0.25}]_{1.8}Zr_{0.4}Co_{1.5}Fe_{12.5}B$ ($MRE_2Fe_{14}B$+Zr). $MRE_2Fe_{14}B$+Zr was again melt-spun at a low wheel speed (10m/s) and compared to HPGA powders <53μm. XRD revealed that the free side was composed of the $MRE_2Fe_{14}B$ phase and that the powders >10μm were primarily MRE_2Fe_{17}, Figure 12 and 13 respectively.

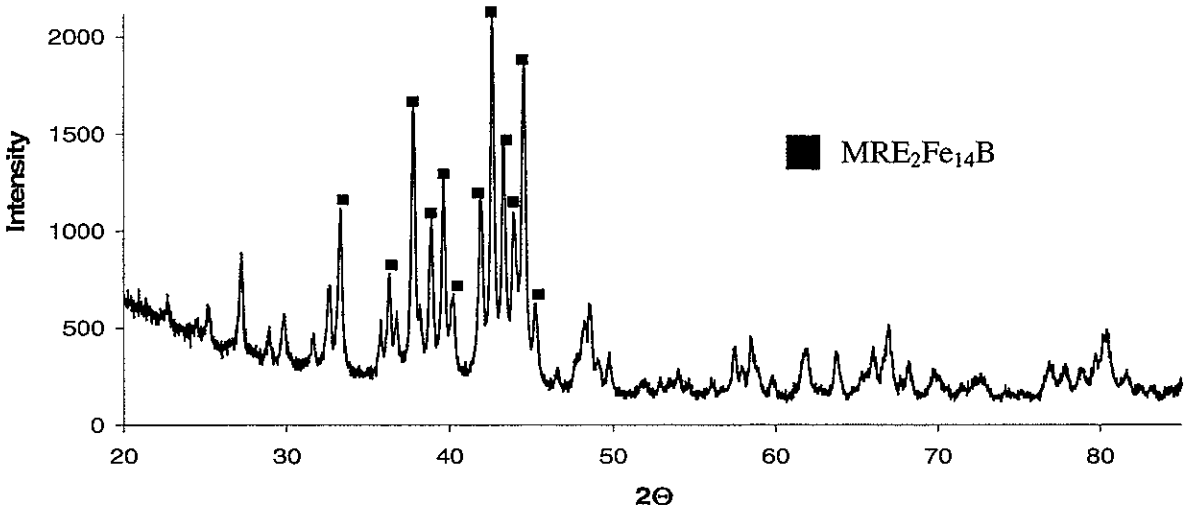

Figure 12: XRD data for the free side of $MRE_2Fe_{14}B$+Zr melt-spun at 10m/s showing a characteristic $MRE_2Fe_{14}B$ pattern.

However, close inspection of the powder particles in the range of 5-10μm revealed a significant increase in the amount of the $MRE_2Fe_{14}B$ phase mixed with the MRE_2Fe_{17} phase, below 5μm the particles were mostly amorphous with a mixture of crystallized MRE_2Fe_{17} and $MRE_2Fe_{14}B$ phases, see Figure 13.

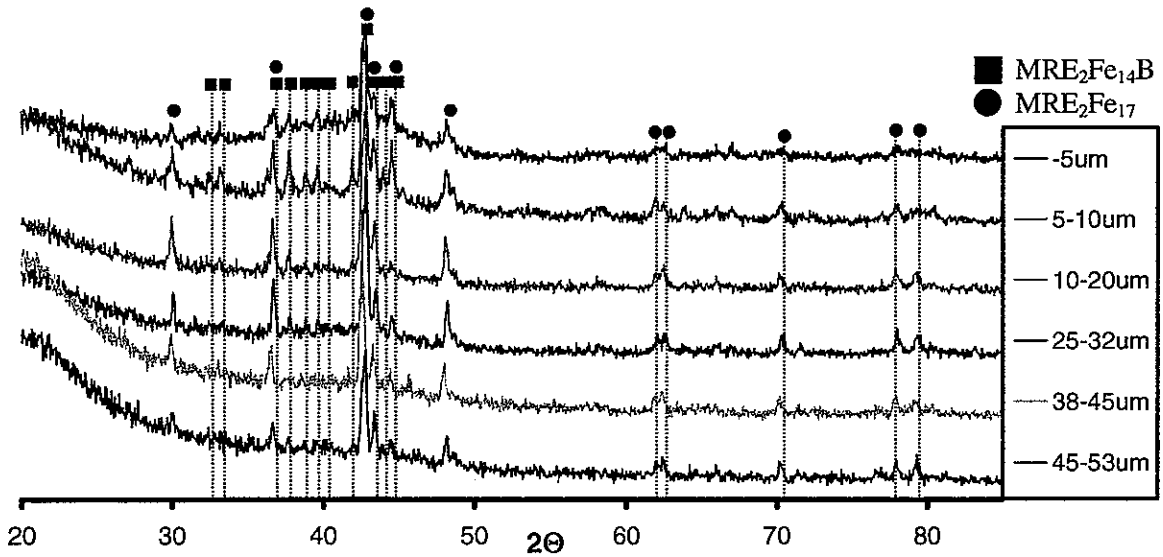

Figure 13: XRD data for HPGA $MRE_2Fe_{14}B$. Characteristic $MRE_2Fe_{14}B$ and MRE_2Fe_{17} peaks are labeled.

The change in phase composition at the smallest particle sizes was also accompanied with a change in microstructure for the atomized particles. Microstructures of the melt-spun ribbon were amorphous and nanocrystalline on the wheel side and the size of the crystallites grew as a function of distance away from the wheel surface. The free side of the ribbon was microcrystalline, much like the melt-spun $YDyFe_{14}B$. HPGA particles in the range of 5-10μm were found to have a microcrystalline microstructure similar in size to the free side of the ribbon, shown in Figure 14.

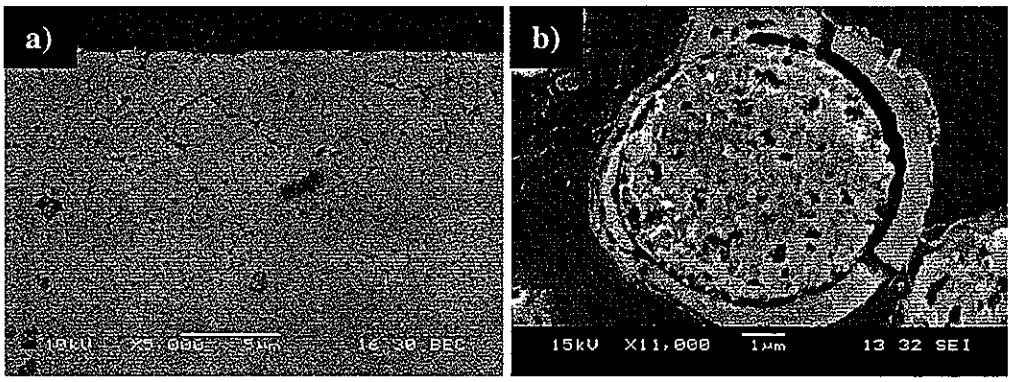

Figure 14: Microstructures for $MRE_2Fe_{14}B$+Zr on the (a) free side of the melt-spun ribbon and for (b) particles in the range of 5-10μm.

Further investigation using electron probe microanalysis of the microcrystalline HPGA particles revealed that the microcrystalline phase is $MRE_2Fe_{14}B$ and, therefore, the contributing factor to the characteristic $MRE_2Fe_{14}B$ peaks seen in the XRD data for the 5-10μm particles. TEM analysis of examples of the shell region on the particle in Figure 14b, not shown [25], revealed that this region was amorphous, equivalent to the wheel side in ribbons of this alloy. The increased amount of $MRE_2Fe_{14}B$ product phase in the gas atomized powders also changed the magnetic properties. The hystresis loop for $YDyFe_{14}B$ particles <10μm is characteristic of a soft material due to the MRE_2Fe_{17} phase. Particles in the range of 5-10μm of the $MRE_2Fe_{14}B$+Zr alloy composition have a hysteresis loop with increased enclose area due to the increase volume of $MRE_2Fe_{14}B$ phase. More area is enclosed in the hystresis loop in the first and third quadrants which are characteristic of mixed hard and soft magnetic phases (see Figure 15). Recent results have shown that the

actual composition of atomized $YDyFe_{14}B$, used for this study, was rare earth deficient. Therefore, the nominal composition was adjusted to be rare earth rich, which resulted in stoichiometric $YDyFe_{14}B$ as the actual composition. The modification caused $MRE_2Fe_{14}B$ to become the primary solidification product. In the <20μm range of particles, $MRE_2Fe_{14}B$ was found to be single phase and microcrystalline which produced good hard magnetic properties.

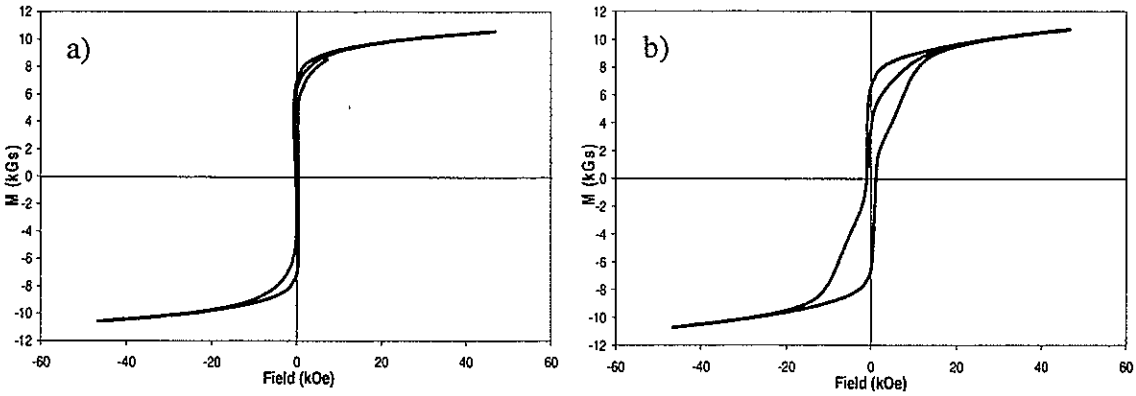

Figure 15: Hystresis loops for (a) <10μm particles of the $YDyFe_{14}B$ composition and (b) 5-10μm particles of the $MRE_2Fe_{14}B$+Zr composition.

CONCLUSIONS

The melt-spinning technique at high wheel speeds can yield $MRE_2Fe_{14}B$ in an overquenched amorphous state that can then be annealed to a microstructure optimal for hard magnetic properties. In this state $MRE_2Fe_{14}B$ experience reduced loss of BH_{max} when tested against commercial $Nd_2Fe_{14}B$. $MRE_2Fe_{14}B$ alloys be crushed and successfully passivated by growing a protective fluoride layer on the surface. PBM of $MRE_2Fe_{14}B$, using PPS as the binder phase, experienced less loss of flux as a function of increasing temperature compared to commercial $Nd_2Fe_{14}B$ subjected to STILT. Further studies to investigate HPGA of $MRE_2Fe_{14}B$ revealed that, through the use of a nucleation catalyst the progression of microstructures and product phases seen on the free side of the melt-spun ribbon could be created in the finest HPGA powders, <10μm, from the spherical powder exterior to the interior.

ACKNOWLEDGMENTS

This work was supported by DOE-EE-FCVT Program, Freedom Car Initiative, Ames Laboratory is acknowledged through contract no. W-7405-Eng-82. The authors are grateful for the performance of STILT testing at Arnold Magnetics Technologies of Marengo, Illinois, on an industrial partnership basis. Also, the authors appreciate the Auger electron spectroscopy and XPS characterization that was performed by Jim Anderegg at Ames Laboratory.

REFERENCES

1. G.C. Hadjipanayis. "Nanophase hard magnets". *Journal of Magnetism and Magnetic Materials.* 200 (1999) 373-391.

2. A. Hütten. "Processing, Structure, and Property Relationships in Nd-Fe-B Magnets". *JOM* March (1992), 11-15.

3. I.E. Anderson, W. Tang, R.W. McCallum. "Particulate processing and high-performance permanent magnets". *International Journal of Powder Metallurgy.* Vol 40:6 (2004) 37-60.

4. ISURF 02935, R.W. McCallum., Y. Xu, M.J. Kramer, I.E. Anderson, K.W. Dennis. "Permanent Magnet Alloy with Improved High Temperature Performance"

5. N.L. Buelow, I.E. Anderson, R.W. McCallum, M.J. Kramer, W. Tang, and K. Dennis, "Comparison of Mixed Rare Earth Iron Boride Gas Atomized Powders to Melt Spun Ribbon for Bonded Isotropic Permanent Magnets," in Advances in Powder Metallurgy & Particulate Materials-2004, compiled by W.B. Jones and R.A. Chernenkoff, MPIF, Princeton, NJ, part 10 (2004) pp. 230-244.

6. R. Mehrabian. "Rapid solidification", *International Metals Review.* Vol. 27, No.4, 185-200 (1982).

7. T.R. Anantharaman, C. Suryanarayana. *Rapidly Solidified Metals.* Trans Tech Publications. Switzerland. 1987.

8. R. M. German, *Powder Injection Molding 1st ed*: Metal Powder Industries Federation, Princeton, New Jersey. 1990.

9. D. Goll., H. Kronmüller. "High performance permanent magnets". *Naturwissenschaften.* 87 (2000) 423-438l.

10. W. Tang, K.W. Dennis, Y.Q. Wu, M.J. Kramer, I.E. Anderson, and R.W. McCallum. "Studies of new YDy-based $R_2Fe_{14}B$ magnets for high temperature performance (R=Y+Dy+Nd)". *IEEE Transactions on Magnetics.* 40 (4), July 2004.

11. W. Tang, K.W. Dennis, Y.Q. Wu, M. J. Kramer, I. E. Anderson and R. W. McCallum "New YDy-based $R_2(Fe,Co)_{14}B$ Melt-spun Magnets (R=Y+Dy+Nd)", Presented in The 5th Pacific Rim International Conference on Advanced Materials and Processing, November 2-5, 2004. Beijing, China.

12. W. Tang, K.W. Dennis, Y.Q. Wu, M. J. Kramer, I. E. Anderson and R. W. McCallum, "Effect of Zr substitution on microstructure and magnetic properties of new YDy-based $R_2Fe_{14}B$ magnets (R=Y+Dy+Nd)", Presented in the 49th Annual Conference on Magnetism and Magnetic Materials, Jacksonville, Florida, November, 7-11, 2004.

13. M.L. Anderson. Surface Passivation and Electrochemical Behavior of Gas Atomized $LaNi_{4.75}Sn_{0.25}$ for Battery Applications. Masters Thesis. Iowa State University. (2000).

14. Magnequench. "MQP 14-12 literature" http://www.magnequench.com/products/index_powders.htm. [Accessed 4 July 2005]

15. D. Raiser, J.P. Deville. *Journal of Electron Spectroscopy and Related Phenomena.* 57, 91 (1991).

16. M.P. Seah. "Distinction between adsorbed monolayers and thicker layers in Auger electron spectroscopy", *Journal of Physics F: Metal Physics.* Vol. 3 August 1973. 1538-1547.

17. Personal communication with Ba-Min Ma (2003)

18. Y.L. Tang, M.J. Kramer, K.W. Dennis, R.W. McCallum, and L.H. Lewis. "On the control of microstructure in rapidly solidified Nd-Fe-B alloys through melt treatment". *Journal of Magnetism and Magnetic Materials.* 267 (2003) 307-315.

19. I.E. Anderson and M.P. Kemppainen. "Undercooling Effects in Gas Atomized Powders". *Undercooled Alloy Phases*, E.W. Collings and C.C. Koch Eds., 1986, TMS-AIME, New Orleans, p 269.

20. D.A. Porter, K.E. Easterling. *Phase Transformations in Metals and Alloys 2nd ed.* Chapman and Hall. London. 1992.

21. R. Mehrabian. "Relationship of heat flow to structure in rapid solidification processing". *Rapid Solidification Processing.* Claitor's Publishing Division, Baton Rouge. (1978) 9-27.

22. O. Shunpei, Tetsuji Saito, Tetsuichi Motegi. "Effects of cooling rate on microstructures and magnetic properties of Nd-Fe-B alloys". *Journal of Alloys and Compounds*. 363 (2004) 263-270.

23. M. J. Kramer H. Mecco, K.W. Dennis, E. Vargonova, R.W. McCallum and R E. Napolitano. "Rapid Solidification and Metallic Glass Formation – Experimental and Theoretical Limits. Presented in The 12th International Conference on Liquid and Amorphous Metals, 11 - 16 July, 2004, Metz, France.

24. H.H. Liebermann and R.L. Bye, Jr. "Rapid solidification processing and its effects on microstructure of metallic alloy strip," *Rapidly Solidified Crystalline Alloys*. Edited by S.K. Das, B.H. Kear, and C.M. Adam. The Metallurgical Society, Inc. (1985) 61-76.

25. Personal communication with Ya-Qaio Wu (2005)

CHAPTER 6: GENERAL CONCLUSIONS

CONCLUSIONS

Many different aspects of novel mixed rare earth iron boron ($MRE_2Fe_{14}B$) were investigated during this study, ranging from processing, to the addition of a protective fluoride coating, to commercial environmental (temperature) testing. The use of melt-spinning to create ribbon flake particulate and high-pressure gas-atomization (HPGA) to create spherical powders have proven to be viable for production of $MRE_2Fe_{14}B$ permanent magnet (PM) powder.

Melt-spinning was completed at two different wheel speeds for two different facets of this study. Wheel speeds of 22m/s and greater were used for the production of $MRE_2Fe_{14}B$ powders in the same way as commercial $Nd_2Fe_{14}B$ for direct comparison. A lower wheel speed of 10m/s was used to simulate cooling rates seen in HPGA. This created an underquenched ribbon whose phase composition and microstructure could be compared to HPGA powders.

At a wheel speed of 22m/s and above the $[Nd_{0.5}(DyY)_{0.25}]_{2.2}Co_{1.5}Fe_{12.5}B$ and $[Nd_{0.45}(YDy)_{0.25}]_{2.2}Co_{1.5}Fe_{12.5}B$ $MRE_2Fe_{14}B$ alloy compositions were overquenched into an amorphous state. A heat treatment of 700°C for 15 minutes was used to achieve an optimal hard magnetic state for the ribbon. The $[Nd_{0.45}(YDy)_{0.25}]_{2.2}Co_{1.5}Fe_{12.5}B$ alloy composition was chosen for industrial tests. The maximum energy product (BH_{max}) of this alloy was tested at increasingly higher temperatures, as was a Nb-modified commercial $Nd_2Fe_{14}B$ powder, and the $MRE_2Fe_{14}B$ experienced less loss of BH_{max} compared to the commercial powder over the range of 25°C-300°C.

In addition to alloy development, a modified fluidized bed process was developed to grow a protective fluoride layer on $MRE_2Fe_{14}B$ flake particles. Since $[Nd_{0.45}(YDy)_{0.25}]_{2.2}Co_{1.5}Fe_{12.5}B$ was selected for commercial testing, it was the material used for calibration of the modified fluidized bed. The modification to the fluidized bed was the addition of a magnetic stirrer to enhance the uniformity of the protective fluoride coating on the flake powders. The fluorinated flake powders, when subjected to air oxidation in a TGA, showed the least amount of mass gain as compared to commercial powder and unfluorinated $MRE_2Fe_{14}B$ powder. Auger and XPS on the fluorinated flake showed that the protective

fluoride coating consisted of a mixture of Y-F and O-F. A minimum fluoride coating thicknesses was determined to be 15nm. This coating thickness could be achieved by using a 0.5% NF_3 concentration in 300 sccm of flowing argon through the fluidized flake particles at 160°C.

Samples of $MRE_2Fe_{14}B$ flake were compression molded with PPS to make polymer bonded permanent magnets (PBM), as was commercial Nd-Fe-Nb-B. When subjected to an industrial environmental test, short term irreversible loss test (STILT), $MRE_2Fe_{14}B$, with the protective fluoride coating, experienced less loss of Helmholtz flux over a temperature range of 25°C to 200°C, compared to the commercial Nd-Fe-Nb-B. However, upon resaturation the commercial powder was able to regain slightly more flux, compared to $MRE_2Fe_{14}B$. This implies that the flux loss experienced by the Nd-Fe-Nb-B is not due to corrosion or structural damage, but due to the intrinsic temperature dependent magnetic properties.

HPGA spherical powder is the desired form for $MRE_2Fe_{14}B$. It was determined through the use of cooling rate models that HPGA powders could experience cooling rates similar to melt-spun ribbon at low wheel speeds, based on average cooling rates. The particles size threshold and wheel speed of interest were determined to be <20μm and 10m/s, respectively. For the alloys near the $MRE_2Fe_{14}B$ alloy composition $YDyFe_{14}B$, the product phase composition and solidification microstructure were more sensitive to composition than the melt-spun version of that alloy over a range of composition. The HPGA powders contained either the MRE_2Fe_{17} phase or the $MRE_2Fe_{14}B$ phase, depending on RE content, while the melt-spun ribbon consisted of $MRE_2Fe_{14}B$. The microstructures were also much different. The HPGA powder was either dendritic for all sizes of particles (with MRE_2Fe_{17} phase predominant) or were single-phase nanocrystalline for all sizes (with $MRE_2Fe_{14}B$ phase) while the melt-spun ribbon had a nanocrystalline microstructure on the wheel side and microcrystalline on the free-side.

Zirconium was added as a nucleation catalyst to decrease the cooling rate needed to form microcrystalline structures and to nucleate the $MRE_2Fe_{14}B$ phase in the HPGA powders that had an increased remanence level (due to a neodymium addition). This resulted in the following $MRE_2Fe_{14}B$ composition $[Nd_{0.45}(YDy)_{0.25}]_{1.8}Zr_{0.4}\,Co_{1.5}\,Fe_{12.5}B$ ($MRE_2Fe_{14}B$+Zr). For the melt-spun ribbon the phase composition was again $MRE_2Fe_{14}B$ and had a

nanocrystalline structure on the wheel side and a microcrystalline structure on the free side. The 0.03wt% zirconium addition was able to refine the microstructure of the HPGA powders and increased the volume of the interdendritic phase, $MRE_2Fe_{14}B$, for all particle sizes. The secondary dendrite arm spacing was also reduced over the previous HPGA powders. Electron microprobe analysis (EPMA) suggested the interdendritic region is where the $MRE_2Fe_{14}B$ phase would reside in the dendritic particles. In the 5-10μm range, of the $MRE_2Fe_{14}B$+Zr alloy composition, the $MRE_2Fe_{14}B$ phase appeared in higher quantity and a microcrystalline structure also appeared. EPMA showed that the microcrystalline particle was composed of the desired $MRE_2Fe_{14}B$ phase and had a similar crystallite size as the free side of the melt-spun ribbon of the same composition.

RECOMMENDATIONS FOR FUTURE WORK

The on-going nature of this study requires that work be continued to further increase the knowledge and understanding of the new $MRE_2Fe_{14}B$ alloy family. The correlation of microstructures obtained at low wheel speeds to those of fine HPGA powders needs to continue so that alloy additions made to $MRE_2Fe_{14}B$ during melt-spinning will be more useful to the HPGA form. The use of current techniques and more extensive use of EPMA and TEM with EDS on both ribbon and powder samples is needed to clearly enhance the understanding of $MRE_2Fe_{14}B$ microstructures. The end result will hopefully be a solidification map that will use the microstructures seen in melt-spun ribbon to predict the microstructure of HPGA powders at different particle sizes.

Alloy additions that specifically affect the microstructure must be classified, and new additions must be designed that will increase the useful particle size obtained from HPGA. When successful alloy designs are accomplished for spherical powders, injection molding of this material with PPS as the binder phase needs to be pursued.

The modified fluidized bed process for growing the protective fluoride layer on the flake powders has proven effective. However, there are still a lot of unknowns and process control issues to address. Currently, control of the NF_3 gas flow is at the lowest level possible with the current setup. Diluting NF_3 with argon as-received in the gas cylinder will allow the flow rate to increase, while retaining low NF_3 concentrations in the gas stream.

The question of the exact composition of the fluoride coating needs to be answered. Scale-up issues also need to be addressed, as the melt-spun flake powders of $MRE_2Fe_{14}B$ moves from a proof of concept to a commercial demonstration phase.

Moving into the commercial demonstration phase also will require increased collaboration with Arnold Magnetics, the industrial collaborator for this study. Further experimentation with the STILT needs to be combined with lifetime testing for $MRE_2Fe_{14}B$, utilizing the long term irreversible loss test available at Arnold Magnetics. An environmental BH_{max} test is also available so that the BH_{max} of $MRE_2Fe_{14}B$ can be measured in both ribbon and PBM form.

ACKNOWLEDGEMENTS

First, I must sincerely express my thanks to my major professor Iver Anderson who was a very inspirational mentor. Iver saw past the numbers to give a student a chance to pursue a higher degree based on his ability to do the work, and for that I am very grateful. I must also express thanks to the magnet group: Bill McCallum, Matt Kramer, Wei Tang, Kevin Dennis, and Ya-Qaio Wu for helping me with experiments and sharing their knowledge of magnetics, solidification, and material characterization. Extra thanks goes out to Wei Tang for XRD and magnetometer data, and to Kevin Dennis for TGA work, and Ya-Qaio for the TEM images. Thanks goes out to Steve Constantinidies at Arnold Magnetic Technologies Corp. for STILT testing of the polymer bonded samples, and to my committee members Matt Kramer and Frank Peters who took the time to read and critique my work.

There is no way I could have gotten through the past couple years with out the help of the good people at Ames Lab: Bob Terpstra was always ready with a down to earth explanation and to help me figure out how to work equipment, Hal Salisbury for his expertise on metallographic processes and excellent stories from late nights giving out parking tickets, the entire MPC crew who did the gas atomization, Fran Laabs for sharing his vast knowledge of SEM, Alfred Kracher for his EPMA work, Jim Anderegg for the Auger and XPS work and for the quick lessons on those techniques, Andy Thom who did some emergency TGA when Kevin's TGA was out of commission, and the ladies in the office Bev, Sue, and Anne who kept me out of trouble when it came to paperwork.

I have to recognize my undergrad helpers. Pete Sokolowski's help was invaluable; he was my right hand man. Lynn Tweed spent a lot of hours polishing and never complained, well about the polishing anyway. Thing 1 (Tom Ocken) and Thing 2 (Joel Rieken) thanks for the air classifying, you're my boys. Chris Baker did a short stint with me doing some polishing (better than I could ever do), and my old officemate Amber Genau who also gets the gold star for being a terrific officemate.

This work was supported by USDOE-EE-FCVT Program, Freedom Car Initiative, through Ames Laboratory contract no. W-7405-Eng-82. The United States government has assigned the DOE Report number IS-T 2562 to this thesis.